



MISSOURI  
**S&T**

# CENTER FOR TRANSPORTATION INFRASTRUCTURE AND SAFETY



## **Development of Bridge Girder Movement Criteria for Accelerated Bridge Construction**

by

**Genda Chen, Ph.D., P.E., F.ASCE, F.SEI**

Professor and Robert W. Abbett Chair in Civil Engineering  
Department of Civil, Architectural, and Environmental Engineering  
Missouri University of Science and Technology  
Rolla, MO 65409-0030

**Yi Bao, Ph.D. Candidate**

Graduate Research Assistant  
Department of Civil, Architectural, and Environmental Engineering  
Missouri University of Science and Technology  
Rolla, MO 65409-0030



**June 2014**



**NUTC  
R316**

**A National University Transportation Center  
at Missouri University of Science and Technology**

## ***Disclaimer***

The contents of this report reflect the views of the author(s), who are responsible for the facts and the accuracy of information presented herein. This document is disseminated under the sponsorship of the Department of Transportation, University Transportation Centers Program and the Center for Transportation Infrastructure and Safety NUTC program at the Missouri University of Science and Technology, in the interest of information exchange. The U.S. Government and Center for Transportation Infrastructure and Safety assumes no liability for the contents or use thereof.

### Technical Report Documentation Page

1. Report No.  NUTC R316	2. Government Accession No.	3. Recipient's Catalog No.	
4. Title and Subtitle Development of Bridge Girder Movement Criteria for Accelerated Bridge Construction		5. Report Date  June 30, 2014	
		6. Performing Organization Code	
7. Author/s  Genda Chen and Yi Bao		8. Performing Organization Report No.  Project #00040815	
9. Performing Organization Name and Address  Center for Transportation Infrastructure and Safety/NUTC program Missouri University of Science and Technology 220 Engineering Research Lab Rolla, MO 65409		10. Work Unit No. (TRAI5)	
		11. Contract or Grant No.  DTRT06-G-0014	
12. Sponsoring Organization Name and Address  U.S. Department of Transportation Research and Innovative Technology Administration 1200 New Jersey Avenue, SE Washington, DC 20590		13. Type of Report and Period Covered  Final	
		14. Sponsoring Agency Code	
15. Supplementary Notes			
16. Abstract End diaphragms connect multiple girders to form a bridge superstructure system for effective resistance to earthquake loads. Concrete girder bridges that include end diaphragms consistently proved to perform well during previous earthquake events. However, whether concrete bridges without end diaphragms are definitively inadequate in seismic performance is yet to be answered. The 2010 Chile Earthquake indicated that properly designed bridge girders and their lateral movement stoppers (shear keys) may perform equally well with those with end diaphragms. In this report, a feasibility study on the design of girder bridges without end diaphragms is presented. This study is particularly significant in the context of accelerate bridge construction since concrete diaphragms are often cast in place and eliminating them can save field erection time and cost. The key to make the no-diaphragm concept work is to understand how multiple girders can work together during a transverse earthquake excitation without breaking the girders and bridge deck. Specifically, a three-dimensional finite element model of a representative concrete girder bridge with and without end diaphragms is established and analyzed to understand the effects of various design parameters (e.g. diaphragm height, diaphragm thickness, the coefficient of friction between girders and their supporting elements, the number and size of shear keys) on transverse girder movement capacity. Numerical results indicate that properly designed end diaphragms can increase the transverse capacity of a bridge by making individual girders work together but can be substituted by shear keys placed between the strengthened girders. In doing so, both transverse capacity and stiffness of the bridge superstructure can be significantly increased. Shear keys are more reliable than the friction mechanism. In particular, movable shear keys are more effective in distributing loads among multiple girders.			
17. Key Words  Bridge, design, accelerated bridge construction, and test		18. Distribution Statement  No restrictions. This document is available to the public through the National Technical Information Service, Springfield, Virginia 22161.	
19. Security Classification (of this report)  unclassified	20. Security Classification (of this page)  unclassified	21. No. Of Pages  101	22. Price

## EXECUTIVE SUMMARY

End diaphragms connect multiple girders to form a bridge superstructure system for effective resistance to earthquake loads. Concrete girder bridges that include end diaphragms consistently proved to perform well during previous earthquake events. However, whether concrete bridges without end diaphragms are definitively inadequate in seismic performance is unknown. The 2010 Chile Earthquake seemed to indicate that properly designed bridge girders and their lateral movement stoppers (shear keys) may perform equally well with those with end diaphragms. This study is particularly significant in the context of accelerate bridge construction since concrete diaphragms are often cast in place and eliminating them can save field erection time and cost.

In this study, the feasibility design of girder bridges without end diaphragms is presented. The main objective of this study is to understand how multiple girders can work together during a transverse earthquake excitation without breaking the girders and bridge deck so that the no-diaphragm concept can be realized in bridge design. To achieve the objective, a three-dimensional finite element model of a representative concrete girder bridge with and without end diaphragms is established. Nonlinear analysis with surface contact elements introduced is conducted in ABAQUS to understand the effects of various design parameters (e.g. diaphragm height, diaphragm thickness, the coefficient of friction between girders and their supporting elements, the number and size of shear keys) on transverse girder movement capacity. Numerical results indicate that properly designed end diaphragms can increase the transverse capacity of a bridge by making individual girders work together but may be substituted by shear keys placed between the strengthened girders. The shear keys can significantly increase both the capacity and stiffness of the bridge superstructure in transverse direction and have little effect in vertical direction. Shear keys are more reliable than the friction mechanism between girders and supporting elements such as cap beams since friction can vary during an earthquake. In particular, movable shear keys are more effective in distributing loads among multiple girders. A compound spring model is presented as an analytical model of movable shear keys and validated by numerical simulations. Properly designed movable shear keys may significantly improve the seismic performance of multi-girder bridges without end diaphragms.

# TABLE OF CONTENTS

<b>SECTION 1 INTRODUCTION.....</b>	<b>1</b>
1.1 Field Observations on Bridge Performance .....	1
1.2 Pushover Analysis .....	2
1.2.1 Failure modes .....	3
1.2.2 Three-dimensional nonlinear finite element model .....	3
1.3 Outline of the Report.....	3
<b>SECTION 2 DESCRIPTIONS OF THE BRIDGE AND THE MODELING .....</b>	<b>5</b>
2.1 Bridge Description .....	5
2.2 Finite Element Modeling.....	5
2.2.1 Assumptions .....	5
2.2.2 Elements .....	6
2.2.3 Material models .....	7
2.2.4 Prestressing .....	9
2.2.5 Analysis algorithm.....	9
2.3 Outline of Simulation Matrixes.....	12
2.3.1 Bridges with end diaphragms .....	12
2.3.2 Bridges without end diaphragm.....	12
<b>SECTION 3 ANALYSIS OF BRIDGES WITH END DIAPHRAGMS.....</b>	<b>14</b>
3.1 Parametric Study of Diaphragm Height.....	14
3.1.1 Installed diagram of full girder height .....	15
3.1.2 Installed diagram of 75% girder height .....	19
3.1.3 Installed diagram of 50% girder height .....	22
3.1.4 Installed diagram of 25% girder height .....	25
3.1.5 Discussion on diaphragm height.....	28
3.2 Parametric Study of Diaphragm Thickness.....	29
3.2.1 Installed 50 cm diaphragm.....	30
3.2.2 Installed 40 cm diaphragm.....	32
3.2.3 Installed 30 cm diaphragm.....	34
3.2.4 Installed 20 cm diaphragm.....	34
3.2.5 Installed 10 cm diaphragm.....	35
3.2.6 Discussion on diaphragm thickness.....	37
3.3 Sensitivity Study for Friction Coefficient .....	39
3.3.1 Friction coefficient 0.3.....	39
3.3.2 Friction coefficient 0.2.....	42

3.3.3 Friction coefficient 0.1.....	45
3.3.4 Frictionless.....	47
3.3.5 Discussion on friction coefficient.....	50
3.4 Summary .....	51
<b>SECTION 4 ANALYSIS OF BRIDGES WITHOUT END DIAPHRAGM .....</b>	<b>53</b>
4.1 Analysis of Bridge without Interior Shear Keys .....	53
4.2 Parametric Study of Friction Coefficient .....	56
4.2.1 Friction coefficient 0.3.....	56
4.2.2 Friction coefficient 0.2.....	58
4.2.3 Friction coefficient 0.1.....	58
4.2.4 Frictionless.....	60
4.2.5 Discussion on friction coefficient.....	62
4.3 Analysis of Bridge with Interior Shear Keys .....	64
4.3.1 Installed one interior shear key.....	64
4.3.2 Installed two interior shear keys.....	67
4.3.3 Installed three interior shear keys.....	69
4.3.4 Installed four interior shear keys.....	72
4.3.5 Discussion on interior shear key.....	74
4.4 Summary .....	76
<b>SECTION 5 DESIGN AND EVALUATION OF DUCTILE SHEAR KEYS .....</b>	<b>77</b>
5.1 Introduction of Shear Keys .....	77
5.2 A Novel Design of Movable Shear Key.....	77
5.3 Implementation .....	78
5.4 Analytical Models .....	78
5.4.1 Series springs.....	79
5.4.2 Stiffness variations in compound model.....	80
5.4.3 Boundary variations in compound model.....	81
5.5 Evaluation of Movable Shear Keys.....	82
5.5.1 Without construction error.....	82
5.5.2 Boundary variations.....	85
5.6 Summery .....	86
<b>SECTION 6 CONCLUSIONS .....</b>	<b>87</b>
<b>REFERENCES.....</b>	<b>88</b>

## LIST OF FIGURES

Fig. 1.1 Observed performance of highway bridges during the 2010 Chile Earthquake. ....	1
Fig. 1.2 Capacity spectrum method. ....	2
Fig. 2.1 Three-span prestressed concrete bridge. ....	5
Fig. 2.2 Simplified finite element model of the Stoddard County Bridge. ....	6
Fig. 2.3 Simulations of the reinforcement in bridge superstructure. ....	7
Fig. 2.4 Concrete response to uniaxial loading. ....	7
Fig. 2.5 Bilinear model. ....	9
Fig. 2.6 Proportional loading with unstable response. ....	10
Fig. 2.7 Simplified flowchart of nonlinear static analysis. ....	11
Fig. 3.1 Bridges installed with different heights of end diaphragms. ....	14
Fig. 3.2 A simplified FE model of bridge installed diaphragm of full girder height. ....	15
Fig. 3.3 Maximum principal stress distribution under self-weight and prestressing. ....	16
Fig. 3.4 Vertical deflection under self-weight and prestressing. ( $\times 500$ ). ....	16
Fig. 3.5 Maximum principal stress under self-weight, prestressing and transverse load. ( $\times 10$ ). ....	16
Fig. 3.6 Damage development in the superstructure. ....	17
Fig. 3.7 Pushover curve (Load-Displacement relation). ....	18
Fig. 3.8 Von Mises stress in mild rebar. ( $\times 10$ ). ....	18
Fig. 3.9 Von Mises stress in prestressed tendons. ( $\times 10$ ). ....	18
Fig. 3.10 Vertical deflection under self-weight, prestressing, and transverse force. ( $\times 500$ ). ....	19
Fig. 3.11 A simplified FE model of bridge installed diaphragm of 75% girder height. ....	19
Fig. 3.12 Maximum principal stress distribution under self-weight and prestressing. ( $\times 500$ ). ....	19
Fig. 3.13 Vertical deflection under self-weight and prestressing. ( $\times 500$ ). ....	20
Fig. 3.14 Maximum principal stress under self-weight, prestressing and transverse load. ....	20
Fig. 3.15 San Nicholas bridge with partial diaphragms. ....	21
Fig. 3.16 Pushover curve (Load-Displacement relation). ....	21
Fig. 3.17 Vertical deflection under self-weight, prestressing, and transverse force. ( $\times 500$ ). ....	21
Fig. 3.18 Transverse drift under self-weight, prestressing, and transverse force. ( $\times 10$ ). ....	22
Fig. 3.19 A simplified FE model of bridge installed diaphragm of 50% girder height. ....	22
Fig. 3.20 Maximum principal stress under self-weight and prestressing. ( $\times 500$ ). ....	23
Fig. 3.21 Vertical deflection under self-weight and prestressing. ( $\times 500$ ). ....	23
Fig. 3.22 Maximum principal stress under self-weight and prestressing. ....	24
Fig. 3.23 Pushover curve (Load-Displacement relation). ....	24

Fig. 3.24 Damage development in the superstructure.....	24
Fig. 3.25 Lateral displacement under self-weight, prestressing, and transverse force. ( $\times 10$ ).....	25
Fig. 3.26 A simplified FE model of bridge installed diaphragm of 25% girder height. ....	25
Fig. 3.27 Maximum principal stress distribution under self-weight and prestressing. ( $\times 500$ ).....	26
Fig. 3.28 Vertical deflection under self-weight and prestressing. ( $\times 500$ ).....	26
Fig. 3.29 Maximum principal stress under self-weight and prestressing.....	26
Fig. 3.30 Pushover curve (Load-Displacement relation). ....	27
Fig. 3.31 Damage development in the superstructure.....	27
Fig. 3.32 Vertical deflection under self-weight, prestressing, and transverse force. ( $\times 500$ ). ....	28
Fig. 3.33 Influence of diaphragm height on vertical behaviors. ....	28
Fig. 3.34 Comparison of pushover curves of bridges with different diaphragm heights. ....	29
Fig. 3.35 Influence of diaphragm height on transverse behaviors. ....	29
Fig. 3.36 Bridges with different heights of end diaphragms.....	29
Fig. 3.37 A simplified FE model of bridge installed diaphragm of 50 cm thickness. ....	30
Fig. 3.38 Maximum principal stress distribution under self-weight and prestressing force. ( $\times 500$ ). ....	30
Fig. 3.39 Vertical deflection under self-weight and prestressing force. ( $\times 500$ ).....	30
Fig. 3.40 Maximum principal stress under self-weight, prestressing, and transverse force. ....	31
Fig. 3.41 Vertical deflection under self-weight, prestressing, and transverse force. ( $\times 500$ ). ....	31
Fig. 3.42 Pushover curve (Load-Displacement relation). ....	32
Fig. 3.43 Maximum principal stress under self-weight and prestressing. ( $\times 500$ ).....	32
Fig. 3.44 Vertical deflection under self-weight and prestressing. ( $\times 500$ ).....	32
Fig. 3.45 Maximum principal stress under self-weight, prestressing, and transverse force. ( $\times 10$ ).....	33
Fig. 3.46 Vertical deflection under self-weight, prestress, and transverse force. ( $\times 500$ ). ....	33
Fig. 3.47 Pushover curve (Load-Displacement relation). ....	34
Fig. 3.48 Maximum principal stress distribution under self-weight and prestressing. ( $\times 500$ ).....	34
Fig. 3.49 Vertical deflection under self-weight and prestressing. ( $\times 500$ ).....	34
Fig. 3.50 Maximum principal stress under self-weight, prestressing, and transverse force. ....	35
Fig. 3.51 Vertical deflection under self-weight, prestressing, and transverse force. ( $\times 500$ ). ....	35
Fig. 3.52 Pushover curve (Load-Displacement relation). ....	35
Fig. 3.53 Maximum principal stress distribution under self-weight and prestressing. ( $\times 10$ ). ....	36
Fig. 3.54 Vertical deflection under self-weight and prestressing. ( $\times 500$ ).....	36
Fig. 3.55 Maximum principal stress under self-weight, prestress, and transverse force. ( $\times 10$ ).....	36
Fig. 3.56 Vertical deflection under self-weight, prestress, and transverse force. ( $\times 10$ ). ....	37
Fig. 3.57 Transverse drift under self-weight, prestressing, and transverse force. ( $\times 10$ ).....	37
Fig. 3.58 Influence of diaphragm thickness on vertical behaviors.....	38



Fig. 3.59 Comparison of pushover curves of bridges with different diaphragm thicknesses. ....	38
Fig. 3.60 Influence of diaphragm thickness on transverse behaviors. ....	39
Fig. 3.61 Maximum principal stress under self-weight and prestressing. ....	39
Fig. 3.62 Vertical deflection under self-weight and prestressing. ( $\times 500$ ). ....	40
Fig. 3.63 Maximum principal stress under self-weight and prestressing. ....	40
Fig. 3.64 Pushover curve (Load-Displacement relation). ....	41
Fig. 3.65 Damage development in the superstructure. ....	41
Fig. 3.66 Transverse drift under self-weight, prestressing, and transverse force. ( $\times 10$ ). ....	42
Fig. 3.67 Maximum principal stress under self-weight and prestressing. ( $\times 500$ ). ....	42
Fig. 3.68 Vertical deflection under self-weight and prestressing. ( $\times 500$ ). ....	43
Fig. 3.69 Maximum principal stress distribution under self-weight and prestressing. ....	43
Fig. 3.70 Damage development in the superstructure. ....	44
Fig. 3.71 Pushover curve (Load-Displacement relation). ....	44
Fig. 3.72 Transverse drift under self-weight, prestressing, and transverse force. ( $\times 10$ ). ....	45
Fig. 3.73 Maximum principal stress distribution under self-weight and prestressing. ( $\times 500$ ). ....	45
Fig. 3.74 Vertical deflection under self-weight and prestressing. ( $\times 500$ ). ....	46
Fig. 3.75 Maximum principal stress under self-weight and prestressing. ....	46
Fig. 3.76 Damage development in the superstructure. ....	47
Fig. 3.77 Pushover curve (Load-Displacement relation). ....	47
Fig. 3.78 Transverse drift under self-weight, prestressing, and transverse force. ( $\times 10$ ). ....	47
Fig. 3.79 Maximum principal stress under self-weight and prestressing. ....	48
Fig. 3.80 Vertical deflection under self-weight and prestressing. ( $\times 500$ ). ....	48
Fig. 3.81 Maximum principal stress under self-weight, prestressing and transverse load. ....	48
Fig. 3.82 Maximum principal stress under self-weight, prestressing and transverse load. ....	49
Fig. 3.83 Pushover curve (Load-Displacement relation). ....	49
Fig. 3.84 Influence of friction coefficient under self-weight and prestressing. ....	50
Fig. 3.85 Comparison of pushover curves of bridges with different friction coefficients. ....	51
Fig. 3.86 Influence of friction coefficient under self-weight, prestressing and transverse load. ....	51
Fig. 4.1 Comparison of the cross sections. ....	53
Fig. 4.2 A simplified FE model of bridge without diaphragm. ....	53
Fig. 4.3 Maximum principal stress distribution under self-weight and prestressing. ....	54
Fig. 4.4 Vertical displacement distribution under self-weight and prestressing. ( $\times 500$ ). ....	54
Fig. 4.5 Maximum principal stress distribution. ....	54
Fig. 4.6 Damage development in the bridge superstructure. ....	55
Fig. 4.7 Damage in Chada Bridge with no diaphragm. ....	55

Fig. 4.8 Transverse drift. ( $\times 10$ ).....	55
Fig. 4.9 Pushover curve (Load-Displacement relation).....	56
Fig. 4.10 Maximum principal stress distribution under self-weight and prestressing.....	56
Fig. 4.11 Vertical deflection under self-weight and prestressing. ( $\times 500$ ).....	56
Fig. 4.12 Maximum principal stress.....	57
Fig. 4.13 Damage development in the superstructure.....	57
Fig. 4.14 Pushover curve (Load-Displacement relation).....	57
Fig. 4.15 Transverse drift. ( $\times 10$ ).....	58
Fig. 4.16 Maximum principal stress distribution under self-weight and prestressing.....	58
Fig. 4.17 Vertical displacement distribution under self-weight and prestressing. ( $\times 500$ ).....	58
Fig. 4.18 Maximum principal stress.....	59
Fig. 4.19 Damage development in the superstructure.....	59
Fig. 4.20 Pushover curve (Load-Displacement relation).....	60
Fig. 4.21 Transverse displacement. ( $\times 10$ ).....	60
Fig. 4.22 Maximum principal stress under self-weight and prestressing.....	60
Fig. 4.23 Vertical deflection under self-weight and prestressing. ( $\times 500$ ).....	61
Fig. 4.24 Maximum principal stress.....	61
Fig. 4.25 Damage development in the superstructure.....	61
Fig. 4.26 Pushover curve (Load-Displacement relation).....	62
Fig. 4.27 Transverse drift. ( $\times 10$ ).....	62
Fig. 4.28 Influence of friction coefficient on vertical behaviors.....	63
Fig. 4.29 Comparison of pushover curves of bridges with different friction coefficients.....	63
Fig. 4.30 Influence of friction coefficient on transverse behaviors.....	63
Fig. 4.31 Illustration of the bridges with various interior shear key configurations.....	64
Fig. 4.32 A simplified FE model of bridge installed one interior shear key.....	64
Fig. 4.33 Maximum principal stress distribution under self-weight and prestressing.....	65
Fig. 4.34 Vertical displacement distribution under self-weight and prestressing. ( $\times 500$ ).....	65
Fig. 4.35 Maximum principal stress distribution.....	66
Fig. 4.36 Damage development in the superstructure.....	66
Fig. 4.37 Pushover curve (Load-Displacement relation).....	66
Fig. 4.38 Transverse displacement in the superstructure. ( $\times 10$ ).....	67
Fig. 4.39 A simplified FE model of bridge installed two interior shear key.....	67
Fig. 4.40 Maximum principal stress under self-weight and prestressing.....	67
Fig. 4.41 Vertical displacement distribution under self-weight and prestressing. ( $\times 500$ ).....	68
Fig. 4.42 Maximum principal stress in the superstructure.....	68

Fig. 4.43 Damage development in the superstructure.....	68
Fig. 4.44 Pushover curve (Load-Displacement relation). ....	69
Fig. 4.45 Transverse drift. ( $\times 10$ ).....	69
Fig. 4.46 A simplified FE model of bridge installed three interior shear key.....	69
Fig. 4.47 Maximum principal stress under self-weight and prestressing.....	70
Fig. 4.48 Vertical deflection under self-weight and prestressing. ( $\times 500$ ).....	70
Fig. 4.49 Maximum principal stress. ( $\times 10$ ).....	70
Fig. 4.50 Damage development in the superstructure.....	71
Fig. 4.51 Pushover curve (Load-Displacement relation). ....	71
Fig. 4.52 Transverse drift. ( $\times 10$ ).....	71
Fig. 4.53 A simplified FE model of bridge installed four interior shear key.....	72
Fig. 4.54 Maximum principal stress under self-weight and prestressing.....	72
Fig. 4.55 Vertical deflection under self-weight and prestressing. ( $\times 500$ ).....	72
Fig. 4.56 Maximum principal stress.....	73
Fig. 4.57 Damage development in the superstructure.....	73
Fig. 4.58 Pushover curve (Load-Displacement relation). ....	73
Fig. 4.59 Transverse drift. ( $\times 10$ ).....	74
Fig. 4.60 Influence of interior shear key number on vertical behaviors. ....	74
Fig. 4.61 Comparison of pushover curves of bridges with different numbers of interior shear keys. ....	75
Fig. 4.62 Influence of interior shear key number on transverse behaviors. ....	75
Fig. 4.63 Comparison of pushover curves of different bridges.....	75
Fig. 5.1 Illustration of the slidable shear key.....	77
Fig. 5.2 Comparison of fixed shear key and slidable shear key.....	78
Fig. 5.3 Implementation of the proposed slidable shear key in bridge application.....	78
Fig. 5.4 The model of compound springs. ....	79
Fig. 5.5 Spring model for each pair of girder and shear key.....	79
Fig. 5.6 The model of compound springs with gaps.....	81
Fig. 5.7 Maximum principal stress. ( $\times 10$ ).....	83
Fig. 5.8 Transverse drift. ( $\times 10$ ).....	83
Fig. 5.9 Maximum principal stress. ( $\times 10$ ).....	83
Fig. 5.10 Transverse drift. ( $\times 10$ ).....	84
Fig. 5.11 Maximum principal stress. ( $\times 10$ ).....	84
Fig. 5.12 Transverse drift. ( $\times 10$ ).....	84
Fig. 5.13 Comparisons of pushover curves of bridges with different shear key configurations.....	85
Fig. 5.14 Comparisons of pushover curves of bridges with gaps. ....	85

## LIST OF TABLES

Table 2.1 Simulations of bridges with end diaphragms. ....	12
Table 2.2 Simulations of bridges without end diaphragm. ....	13

## SECTION 1 INTRODUCTION

### 1.1 Field Observations on Bridge Performance

Accelerated bridge construction (ABC) and bridge rehabilitation have become a worldwide trend in urban areas.<sup>1-3</sup> In the U.S, significant efforts have been devoted to understanding the seismic behavior of ABC connections among precast components. The ABC trend expects to continue in the years to come with increasing pace for implementation. Two main strategies for a successful ABC design and construction are to simplify bridge components and maximize opportunities for their prefabrication and erection.

During the reconnaissance trip to Chile in 2010,<sup>4,5</sup> the Federal Highway Administration (FHWA) team investigated the performance of reinforced concrete (RC) girder bridges that were constructed similar or dissimilar to the U.S. practices. Fig. 1.1 shows a comparison of four types of bridge bent details. Bridges with neither end diaphragms nor concrete teeth on cap beams suffered the most damage as exemplified in Fig. 1.1(a). Partial-depth end diaphragms caused transverse shear block or lateral fracture failures of RC girders as shown in Fig. 1.1(b). Concrete teeth on cap beams helped the bridge survive the earthquake with no damage except for local spalling at the concrete teeth due to earthquake-induced pounding as illustrated in Fig. 1.1(c). The bridges with full-depth end diaphragms always performed well as indicated in Fig. 1.1(d). Although the U.S. commonly practiced full-depth end diaphragms proved effective, the bridges with no end diaphragms but with concrete teeth appeared a potential alternative. On the other hand, the elimination of end diaphragms can simplify bridge components and thus benefit the ABC. It can also save materials and reduce labor costs.



**Fig. 1.1 Observed performance of highway bridges during the 2010 Chile Earthquake.**

In this study, the feasibility design of girder bridges without end diaphragms is presented. The main objective of this study is to understand how multiple girders can work together during a transverse earthquake excitation without breaking the girders and bridge deck so that the no-diaphragm concept can be realized in bridge design. To achieve the objective, a three-dimensional finite element model of a representative concrete girder bridge with and without end diaphragms is established. Nonlinear analysis

with surface contact elements introduced is conducted in ABAQUS to understand the effects of various design parameters (e.g. diaphragm height, diaphragm thickness, the coefficient of friction between girders and their supporting elements, the number and size of shear keys) on transverse girder movement capacity.

## 1.2 Pushover Analysis

In a study of the structural behavior of bridges under earthquake loading, an adequate characterization and interpretation of the seismic demand requests the consideration of the nonlinear behavior of structural elements. Given that the current seismic design and assessment codes emphasize the need for more accurate deformation analyses, instead of the common force-based ones, there is a clear advantage in using nonlinear analysis to obtain a more precise characterization of deformation measures such as ductility demand.

Pushover analysis, also known as nonlinear static analysis, can provide an insight into the structural performance during severe earthquakes.<sup>9-11</sup> It provides the capacity and ductility of the structure, which cannot be obtained by elastic analysis. The load-displacement curve obtained by pushover analysis is known as the capacity curve that characterizes the structural capacity. By comparing the capacity curve with the demand curve which depends upon the seismic ground motion, whether a structure is adequate in resisting the earthquake effect will be evaluated. In addition, by pushover analysis the potential failure mode can be identified, which leads to an optimal structural design.

In recent years, the capacity spectrum method has rapidly gained increasing acceptance. It was originally developed by Freeman.<sup>12</sup> The capacity spectrum method compares the capacity of a structure with the seismic demand on the structure through a graphical procedure. The graphical presentation makes possible a visual evaluation of how the structure will perform when subjected to earthquake ground motion, as shown in Fig. 1.2.<sup>13</sup> The capacity of the structure is represented by a force-displacement curve, obtained by pushover analysis. The shear force-displacement relations are converted to the spectral acceleration and spectral displacement of an equivalent single-degree-of-freedom (SDOF) system, respectively. These spectral values define the capacity spectrum. The demands of the earthquake ground motion are defined by highly damped elastic spectra. The acceleration-displacement response spectrum (ADRS) format is used, in which spectral accelerations are plotted against spectral displacements with the vibration periods represented by radial lines. The intersection of the capacity spectrum and the demand spectrum provides an estimate of the inelastic acceleration (strength) and displacement demand.<sup>13,14</sup>

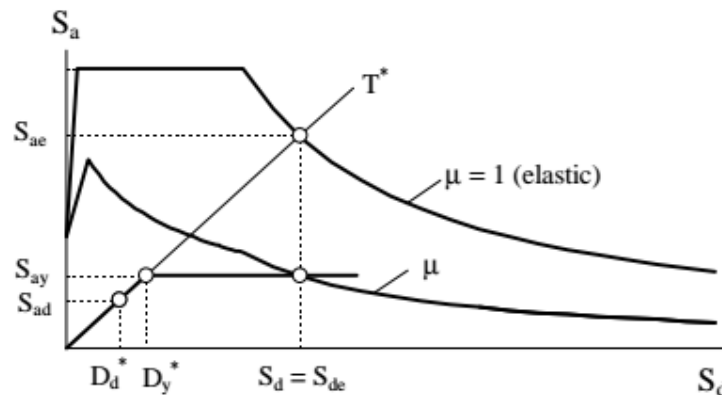


**Fig. 1.2 Capacity spectrum method.**

To carry out a pushover analysis, the force distribution and target displacement are based on assumptions. Hence, if the structural response is significantly influenced by higher modes, it will be in principle inaccurate to count only the fundamental mode. That is, it may not detect structural damage resulting from the change in structural dynamic characteristics. One practical method to partly overcome this limitation is to apply the model pushover analysis (MPA).<sup>15</sup>

In this study, pushover analysis was carried out to analyze the failure modes of bridge structures with various end diaphragm and boundary conditions. The transverse flexural stiffness of a simply-supported beam is often very large in the deck plane. In most cases, the fundamental mode shape will thus dominate in the seismic analysis. In addition, the gravity center is near the deck plane. Therefore, a transverse point load can be applied on the deck. The bridge system will eventually fail as the applied load increases, and the failure mode can thus be demonstrated. With gravity loads, the superstructure was also subjected to friction in addition to the transverse point load. In this study, only transverse ground motion was considered and no vertical ground motion and rocking were taken into account.

### **1.2.1 Failure modes**

To design a structural system for a given function, engineers must understand how the system works and fails. Possible failure modes of the structure must be understood with corresponding failure criteria. For a structure or a structural member under loads, the structural response depends not only on the materials but also on the environmental and loading conditions.

Depending on how it is loaded, a structural member may fail by excessive deflection, losing its design function; by plastic deformation (generally yielding), resulting in a permanent, undesirable change in shape; or by ductile or brittle fracture (break); or by progressive growth of one or more cracks in a member subjected to repeated loads, often culminates in a brittle fracture type of failure. Elastic or plastic instability is another failure mode. In this failure manner, the structural member may undergo large displacements from its design configuration when the applied load reaches a critical value, the buckling load (or instability load). This type of failure may result in excessive displacement or loss of ability (because of yielding or fracture) to carry the design load. In addition to the failure modes already mentioned, a structural member may fail because of corrosion.

The failure modes of structural members mainly include: 1. failure by excessive deflection: a. elastic deflection; b. deflection caused by creep. 2. Failure by general yielding. 3. Failure by fracture: a. sudden fracture of brittle materials; b. Fracture of cracked or flawed members; c. Progressive fracture (fatigue). 4. Failure by instability.

These failure modes and their associated failure criteria are most meaningful for simple structural members (e.g., tension members, columns, beams, circular cross section torsion members). For more complicated problems, the significance of such simple failure modes is open to question. Many of these failure modes for simple structural members are well known to engineers. However, under unusual conditions of load or environment, other types of failure may occur. The physical action in a structural member leading to failure is usually a complicated phenomenon, and in the following discussion the phenomena are necessarily oversimplified, but they nevertheless retain the essential features of the failures.

### **1.2.2 Three-dimensional nonlinear finite element model**

Three-dimensional (3D) nonlinear finite element (FE) modeling technique has been widely applied in various applications besides civil engineering, which provide informative simulation results.<sup>6-8</sup> In this research, 3D nonlinear FE models were established for the analysis of the 3D detailed stresses in bridge structures. Nonlinear material properties and boundary conditions were taken into consideration.

3D nonlinear FE modeling technique could be implemented by various finite element codes. ABAQUS codes were adopted in this research to take advantage of the high computation efficiency for 3D detailed stress problems and high accuracy for nonlinear problems.<sup>16</sup>

## **1.3 Outline of the Report**

In this research, the failure modes and capacities of bridges with different end diaphragm and boundary conditions were investigated by pushover analyses using 3D nonlinear FE method.

Different bridge structures were evaluated based on the structural performances, and how the multiple girder work together was demonstrated. In addition, sacrificial shear keys were implemented to improve the ductility of the bridges, and various designs were proposed.

The report was organized in seven sections.

Section 1 is the introduction covering the main objectives and background technologies of this research.

Section 2 introduces the bridge and the implementation of the FE modeling technique.

Section 3 elaborates the analysis of the original bridge, and then the function of the end diaphragms are characterized by varying the diaphragm height and thickness for bridges with two types of shear key conditions.

Section 4 elaborates the analyses of bridges without end diaphragm, and the function of the exterior and interior shear keys are investigated.

Section 5 presents a novel design of ductile shear key and a model of compound springs. The proposed design is evaluated and the model is validated by numerical simulations.

Section 6 briefly summarizes the findings in this study.



## SECTION 2 DESCRIPTIONS OF THE BRIDGE AND THE MODELING

### 2.1 Bridge Description

Extensive modeling in this research was conducted by using an existing Missouri Bridge as a subject for the simulations looking into the effects of introducing shear keys and concrete diaphragms at the supports. The goal was to base the simulation on an existing structure to quantify observable change. An existing bridge named Stoddard County Bridge was used as the subject of this study, as shown in Fig. 2.1. The bridge which was built in 1995, and is a three-span prestressed concrete bridge consisting of five girders that are simply supported on the pier cap or abutment. The length of each span is 28 m with zero longitudinal slopes. Cast-in-place concrete piles were used for the foundation. Each pier is seated on six deep cylindrical piles.



**Fig. 2.1 Three-span prestressed concrete bridge.**

The design was based on AASHTO-1992 and interims through 1994. The concrete for the prestressed girders was Class A1 with  $f'_c = 41$  MPa and  $f'_{ci} = 31$  MPa. The prestressing tendons were uncoated seven-wire low-relaxation strands with a 12.7 mm diameter conforming to AASHTO-M203 Grade 270. In each girder, 36 strands were used with an initial prestressing force of 5 kN. Mild reinforcement was also used, including #4 and #6 rebar in girders, and #6 and #8 rebar in the deck. The minimum clearance of mild reinforcement was 4 cm. The Stoddard County Bridge was installed with full reinforced concrete diaphragms, and the diaphragm thickness was 30 cm.

### 2.2 Finite Element Modeling

The failure mode and capacity under transverse load of each bridge superstructure were investigated and compared in this study based on the structural behaviors that were analyzed by FE method. The modeling is hereby introduced.

#### 2.2.1 Assumptions

To simplify the FE model, three assumptions were taken into consideration.

(1) The bridge substructures such as piers or abutments are strong and thus will not be damaged in the loading process. The bridge superstructure is focused on. The substructures can be simplified as the caps that provide boundaries for the superstructure.

(2) The kinematic friction coefficient (FC) between concrete surfaces is assumed to be 0.2, which is not accurate in many cases, so a sensitivity study is carried out.

(3) The bridge is very stiff in the deck plane and therefore only the first vibration mode was considered in that plane.

Based on the above assumptions, 3D nonlinear FE modeling technique was implemented by ABAQUS codes. A FE model is shown in Fig. 2.2.

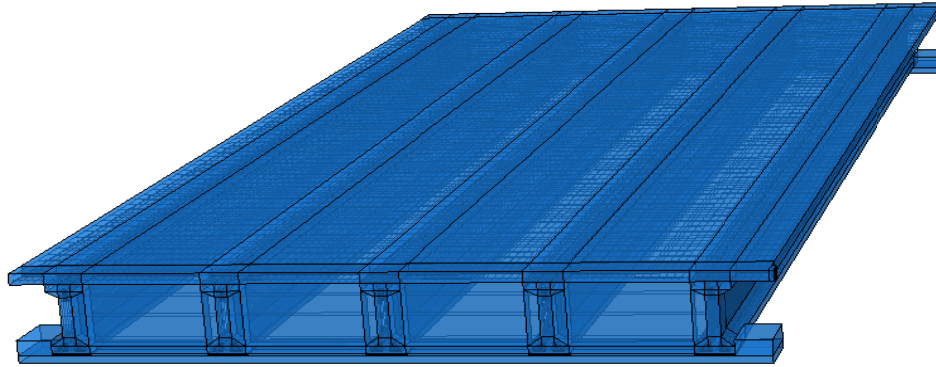
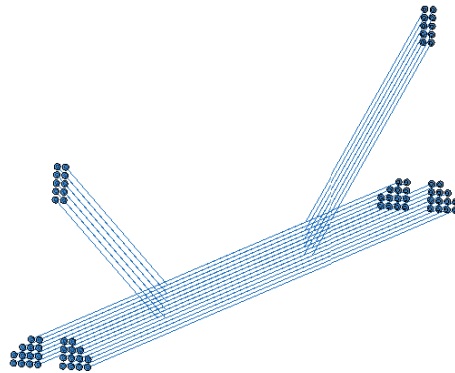


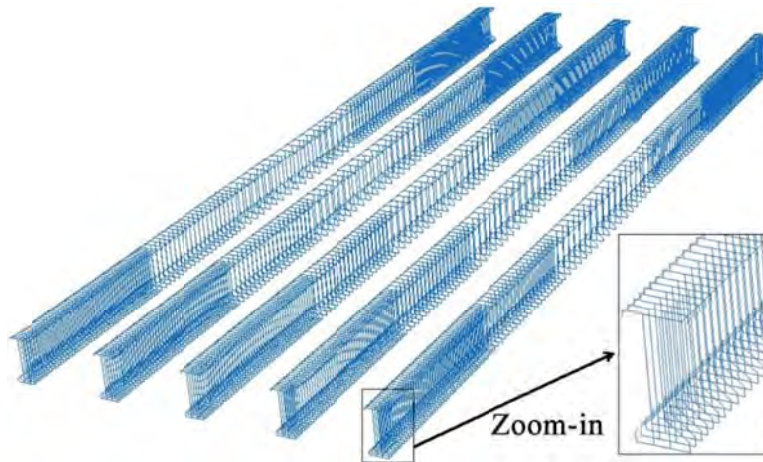
**Fig. 2.2 Simplified finite element model of the Stoddard County Bridge.**

### 2.2.2 Elements

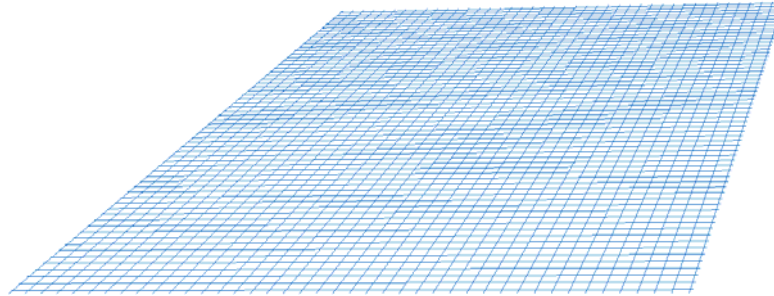
The deck panel, girders, diaphragms, pier caps, shear keys, the rebar in shear keys, loading block, and the anchorage for prestressed tendons were simulated by 3D solid elements; the prestressed tendons and mild rebar in the deck and girders were simulated by 3D truss elements, as shown in Fig. 2.3. No moments or forces perpendicular to the centerline are supported for truss elements.



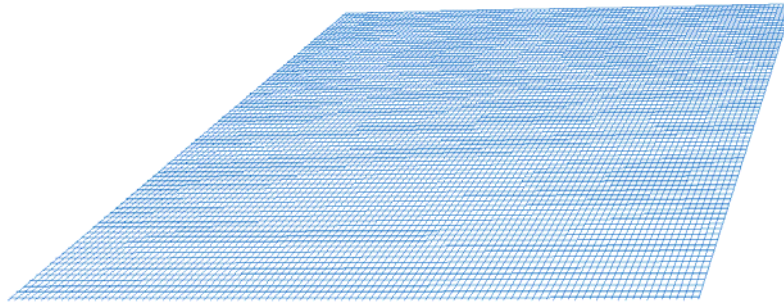
**(a) Prestressed tendons and anchorage in a girder.**



**(b) Mild rebar in the girders.**



(c) Top layer of mild rebar in the deck.



(d) Bottom layer of mild rebar in the deck.

Fig. 2.3 Simulations of the reinforcement in bridge superstructure.

### 2.2.3 Material models

The main bridge superstructure consisted of concrete, mild rebar, high strength steel tendons, and steel anchorage system; rubber bearings were used. Nonlinear stress-strain relations were defined for concrete and mild rebar in bridge superstructure.

Concrete damaged plasticity (CDP) model was used to characterize the concrete material as shown in Fig. 2.4. CDP model provides a capability for modeling concrete using concepts of isotropic damaged elasticity in combination with isotropic tensile and compressive plasticity to represent the inelastic behavior of concrete.<sup>17</sup> CDP model can be used for plain concrete and reinforced concrete. It was designed for applications in which concrete is subjected to monotonic, cyclic, and/or dynamic loading under low confining pressures. CDP model is a continuum, plasticity-based, damage model for concrete. It assumes that the main two failure mechanisms of concrete are tensile cracking and compressive crushing. The evolution of the yield (or failure) surface is controlled by tensile and compressive equivalent plastic strains,  $\tilde{\varepsilon}_t^{pl}$  and  $\tilde{\varepsilon}_c^{pl}$ , linked to failure mechanisms under tension and compression loading, respectively.<sup>18,19</sup> CDP model assumes that the uniaxial tensile and compressive responses of concrete are characterized by damaged plasticity.

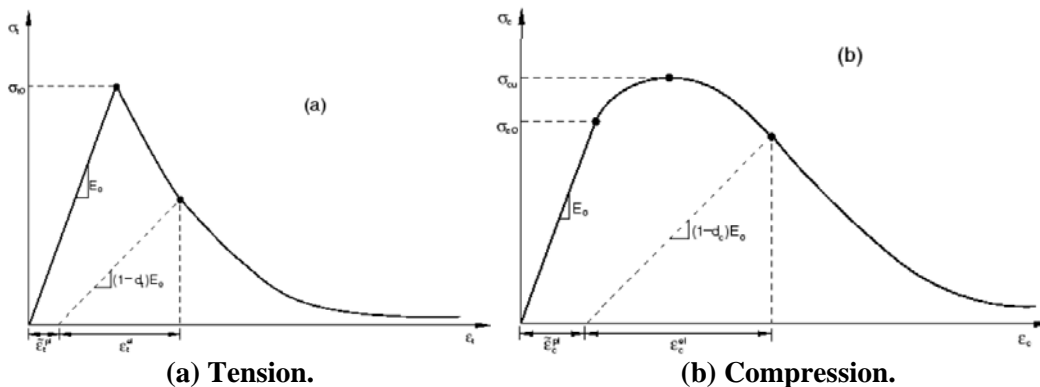


Fig. 2.4 Concrete response to uniaxial loading.

Under uniaxial tension, the stress-strain response follows a linear elastic relationship until reaching the failure stress value,  $\sigma_{t0}$ . The failure stress corresponds to the onset of micro-cracking in the concrete material. Beyond the failure stress the formation of micro-cracks is represented macroscopically with a softening stress-strain response, which induces strain localization in the concrete structure. Under uniaxial compression, the response is linear until the initial yield value,  $\sigma_{c0}$ . In the plastic regime the response is typically characterized by stress hardening followed by strain softening beyond the ultimate stress,  $\sigma_{cu}$ .

When the concrete specimen is unloaded from any point on the strain softening branch of the stress-strain curves, the unloading response is weakened: the elastic stiffness of the material appears to be damaged (or degraded). The degradation of the elastic stiffness is characterized by two damage variables,  $d_t$  and  $d_c$ , which are assumed to be functions of the plastic strains, temperature, and field variables.

$$d_t = d_t(\tilde{\varepsilon}_t^{pl}, \theta, f_i); 0 \leq d_t \leq 1,$$

$$d_c = d_c(\tilde{\varepsilon}_c^{pl}, \theta, f_i); 0 \leq d_c \leq 1.$$

The damage variables can take values from zero, representing the undamaged material, to one, which represents total loss of strength.

If  $E_0$  is the initial (undamaged) elastic stiffness of the material, the stress-strain relations under uniaxial tension and compression loading are, respectively:

$$\sigma_t = (1 - d_t)E_0(\varepsilon_t - \tilde{\varepsilon}_t^{pl}),$$

$$\sigma_c = (1 - d_c)E_0(\varepsilon_c - \tilde{\varepsilon}_c^{pl}).$$

Effective cohesion stresses determine the size of the yield (or failure) surface. The “effective” tensile and compressive cohesion stresses as:

$$\bar{\sigma}_t = \frac{\sigma_t}{1 - d_t} = E_0(\varepsilon_t - \tilde{\varepsilon}_t^{pl}),$$

$$\bar{\sigma}_c = \frac{\sigma_c}{1 - d_c} = E_0(\varepsilon_c - \tilde{\varepsilon}_c^{pl}).$$

The density is 2500 kg/m<sup>3</sup>; Young’s modulus is 30 GPa; Poisson ratio is 0.21.<sup>20</sup>

Bars are considered as one-dimensional rods that can be defined singly or embedded in oriented surfaces. Bars are typically used with metal plasticity models to describe the behavior of the rebar material and are superposed on a mesh of standard element types used to model the concrete. With this modeling approach, the concrete behavior is considered independently of the rebar. Effects associated with the rebar/concrete interface, such as bond slip and dowel action, are modeled approximately by introducing some “tension stiffening” into the concrete modeling to simulate load transfer across cracks through the rebar.

Mild bar was defined as ideal elasto-plastic material, as shown in Fig. 2.5. The density is 7800 kg/m<sup>3</sup>, the Young’s modulus is 210 GPa, and the Poisson ratio is 0.3. Prestressed tendons are made of high strength steel that demonstrated linear elastic behavior, and thus was defined as linear elastic material.

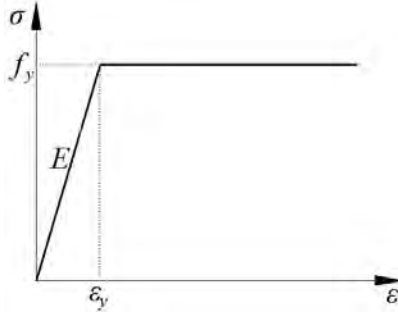


**Fig. 2.5 Bilinear model.**

In finite element analysis, small contact surface between a pair of contacting surfaces will lead to stress concentration for elastic materials but usually will not cause computation problem; however, for inelastic materials, most often the iterative computations cannot converge to a good solution due to the stress concentration.<sup>21</sup> To address this issue, the transverse point load was applied onto an elastic steel block that is tied onto the bridge deck, and then the point load can be distributed by the contact area so the stress concentration problem will be avoided.

### 2.2.4 Prestressing

For the prestressed tendons, when prestressing force was applied to the prestressed tendons, the concrete near the two ends of the tendons would be subjected to high stress change due to the strain transfer from the tendons to the concrete, and the stress concentration happened which prevented the computation from converging. An anchorage system was used to address this issue following the same concept. In addition, the modeling of the anchorage system matched with the real world applications.

The prestressing in prestressed tendons was simulated by temperature decrease based on the relation between strain change and temperature change. As described in equation (2.1), the prestressing force in the tendons is related to the strain change that is equal to the temperature change multiplied by the coefficient of thermal expansion (CTE). Given the Young's modulus and cross section of the tendons, the temperature change that needs to be applied can be calculated by the prestressing force.

$$F_{ps} = EA\varepsilon = EA\alpha\Delta T \quad (2.1)$$

where,  $F_{ps}$  denotes prestressing force,  $E$ ,  $A$ , and  $\alpha$  represent the Young's modulus, the cross section, and the CTE of the tendons, respectively;  $\Delta T$  denotes the temperature change.

If an analysis is undertaken of a practical structure with only the prestress acting, it is often found that cracking of the concrete is predicted. This is because the cable is designed to partially balance the stress due to external load. It is convenient therefore to analyze the initial state of the structure with the effects of both the prestressed and self-weight. If these effects are analyzed separately spurious non-linear effects are introduced because of cracking. Because the behavior in the post cracking stage is significantly non-linear, it is not possible to treat the two effects separately and superpose the results.

### 2.2.5 Analysis algorithm

Pushover analysis involves progressive collapse behavior, where the load-displacement response shows a negative stiffness and the structure must release strain energy to remain in equilibrium. Several approaches are possible for modeling such behavior. One is to treat the buckling response dynamically, thus actually modeling the response with inertia effects included as the structure snaps. This approach is easily accomplished by restarting the terminated static procedure and switching to a dynamic procedure when the static solution becomes unstable. In some simple cases displacement control can provide a solution, even when the conjugate load (the reaction force) is decreasing as the displacement increases. Another approach would be to use dashpots to stabilize the structure during a static analysis.

Alternatively, static equilibrium states during the unstable phase of the response can be found by the “modified Riks method”.<sup>22-24</sup> This method is used for cases where the loading is proportional; that is, where the load magnitudes are governed by a single scalar parameter. The method can provide solutions even in cases of complex, unstable response such as that shown in Fig. 2.6.

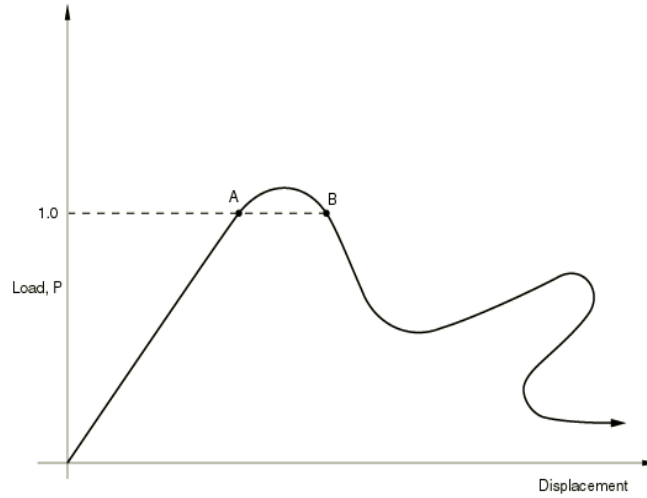


**Fig. 2.6 Proportional loading with unstable response.**

The established FE models were solved by modified Risk (arc-length) method that was usually used to predict unstable, geometrically nonlinear collapse of a structure including nonlinear materials and boundary conditions. The Riks method uses the load magnitude as an additional unknown; it solves simultaneously for loads and displacements. Therefore, “arc length” along the static equilibrium path in load-displacement space another quantity is used to measure the progress of the solution. This approach provides solutions regardless of whether the response is stable or unstable.

If the Riks step is a continuation of a previous history, any loads that exist at the beginning of the step and are not redefined are treated as “dead” loads with constant magnitude. A load whose magnitude is defined in the Riks step is referred to as a “reference” load. All prescribed loads are ramped from the initial (dead load) value to the reference values specified.

The loading during a Riks step is always proportional. The current load magnitude,  $P_{total}$ , is defined by equation (2.2).

$$P_{total} = P_0 + \lambda(P_{ref} - P_0) \quad (2.2)$$

where  $P_0$  is the “dead load,”  $P_{ref}$  is the reference load vector, and  $\lambda$  is the “load proportionality factor.” The load proportionality factor is found as part of the solution.

The Riks procedure uses only a 1% extrapolation of the strain increment. An initial increment in arc length along the static equilibrium path,  $\Delta l_{in}$ , is specified when the step is defined. The initial load proportionality factor,  $\Delta \lambda_{in}$ , is computed as

$$\Delta \lambda_{in} = \frac{\Delta l_{in}}{l_{period}} \quad (2.3)$$

where,  $l_{period}$  is a user-specified total arc length scale factor (typically set equal to 1). The value of  $\Delta \lambda_{in}$  is used during the first iteration of a Riks step. For subsequent iterations and increments the value of  $\lambda$  is computed automatically, so you have no control over the load magnitude. The value of  $\lambda$  is part of the solution. The minimum and maximum arc length increments,  $\Delta l_{min}$  and  $\Delta l_{max}$ , can be used to control the automatic incrementation. A simplified flowchart of the nonlinear static analysis procedure is illustrated in Fig. 2.7.

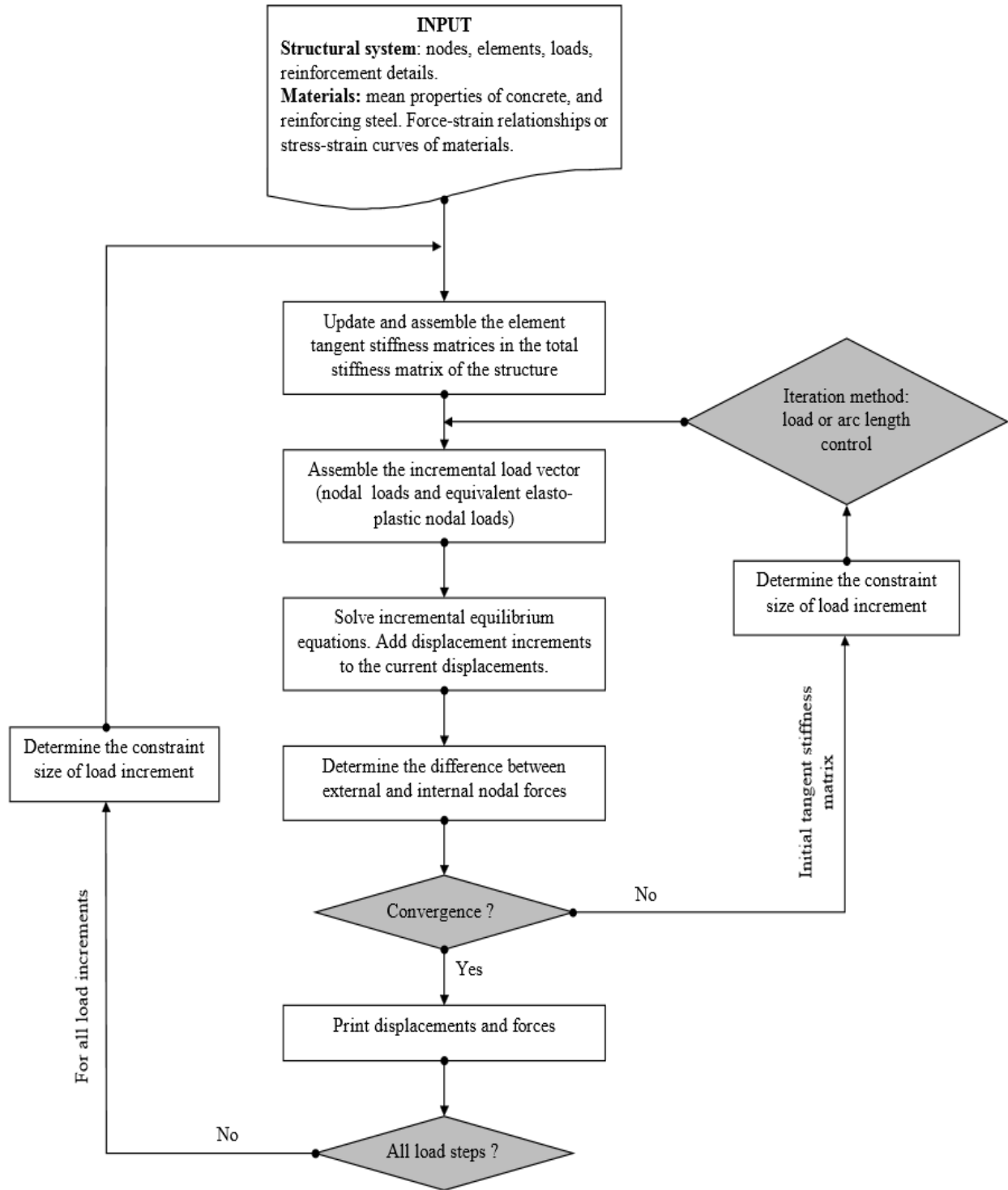


**Fig. 2.7 Simplified flowchart of nonlinear static analysis.**

## 2.3 Outline of Simulation Matrixes

### 2.3.1 Bridges with end diaphragms

Table 2.1 shows the organization of simulations for bridges with end diaphragms. The functions and effectiveness of diaphragm height, thickness, and the friction coefficient (FC) of the support were evaluated.

**Table 2.1 Simulations of bridges with end diaphragms.**

Thickness (cm) Height	10	20	30	40	50
1/4	---	---	FC=0.2	---	---
2/4	---	---	FC=0 FC=0.1 FC=0.2 FC=0.3	---	---
3/4	---	---	FC=0.2	---	---
1 (full diaphragm)	FC=0.2	FC=0.2	FC=0.2	FC=0.2	FC=0.2

In the investigation of the influence of diaphragm height, the diaphragm thickness and FC were set to be 30 cm and 0.2, respectively, and the height ratio was varied from 100% to 25% with a 25% step.

Bridges installed with full diaphragms were used in the evaluation of the diaphragm thickness; FC was fixed as 0.2; the thickness was varied from 50 cm to 10 cm with a 10 cm step.

Bridges with half diaphragms were used in the investigation of the influence of FC; the diaphragm thickness was 30 cm; FC was varied from 0.3 to 0 with a 0.1 step.

In each case, the failure mode, transverse stiffness and capacity of were investigated. The impact of each parameter was quantified by the comparison of structural behaviors when the parameter was changed.

### 2.3.2 Bridges without end diaphragm

Table 2.2 shows the organization of simulations for bridges without end diaphragm. The impact and effectiveness of the number of interior shear key, the friction coefficient (FC) of the support and the construction error were evaluated. The construction error was simulated by presetting gaps between the girders and shear keys. Based on the results of simulations and comparisons, the concept of slidable shear key was presented, and a design was proposed. The proposed design was evaluated by finite element analysis.



**Table 2.2 Simulations of bridges without end diaphragm.**

FC \ Number of interior SK	0	1	2	3	4
0 (frictionless)	Fixed SK	---	---	---	---
0.1	Fixed SK	---	---	---	---
0.2	Fixed SK	Fixed SK	Fixed SK	Fixed SK Fixed SK with gap Slidable SK Slidable SK with gap	Fixed SK
0.3	Fixed SK	---	---	---	---

In each case, the failure mode, transverse stiffness and capacity of were investigated. The impact of each parameter was quantified by the comparison of structural behaviors when the parameter was changed.

## SECTION 3 ANALYSIS OF BRIDGES WITH END DIAPHRAGMS

In this section, the failure modes and transverse capacities of bridge superstructures with end diaphragms were investigated by carrying out pushover analyses.

Exterior shear keys are designed to constrain the transverse movement of the girders subjected to seismic ground motions.<sup>25,26</sup> When the girders transversely move and contact the exterior shear keys, transverse contact forces will be provided to resist the inertia force due to the earthquake. On the other hand, the transverse force will be applied on the exterior girder.

Both end and intermediate diaphragms benefit the bridge by enhancing the overall stiffness of the bridge can be increased. When a bridge is subjected to vertical loads, for instance, the vehicle loads, the bridge can take advantage of the enhancement, in that the vehicle loads can be distributed more uniformly to the multiple girders.<sup>27,28</sup> There are two enhancement mechanisms for bridges subjected to transverse force. First, diaphragms are designed to be stiff and have high strength in plane, so they can help resist transverse force applied on the superstructure. Bridge girders are designed to mainly resist vertical load; hence, they usually have small stiffness and strength in the transverse direction, which can be compensated by the end diaphragms. On the other hand, the connections between multiple girders are enhanced and hence the transverse force can be resisted by multiple girders together instead of being resisted by the exterior girder. Therefore, the seismic performance of a bridge is closely related to the configuration of the end diaphragm, which was observed in failures noted in the 2010 reconnaissance trip to Chile.<sup>4,5</sup>

The failure mode and transverse capacity associated with the height and thickness of the end diaphragms were investigated and elaborated below.

### 3.1 Parametric Study of Diaphragm Height

Four cases corresponding to four levels of end diaphragm height were investigated, including 100%, 75%, 50%, and 25%, as shown in Fig. 3.1. The thickness of the diaphragms was 30 cm.

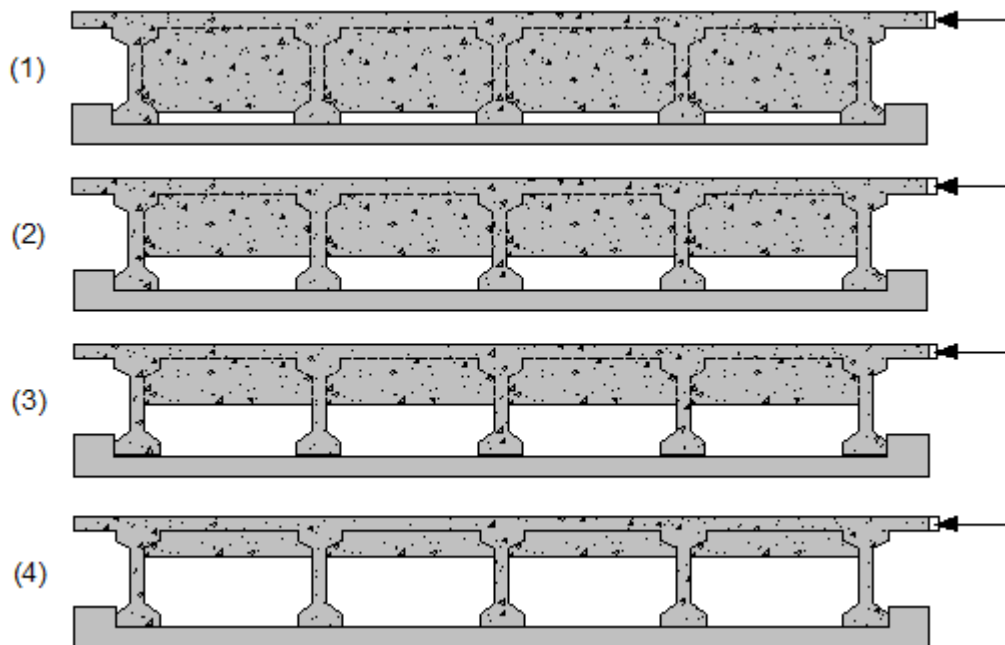
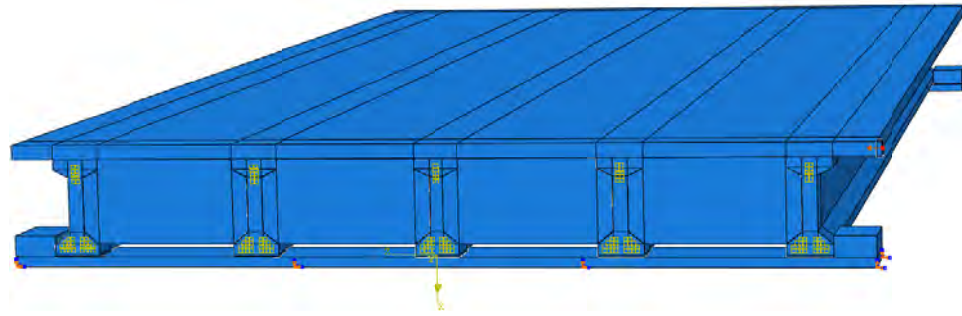


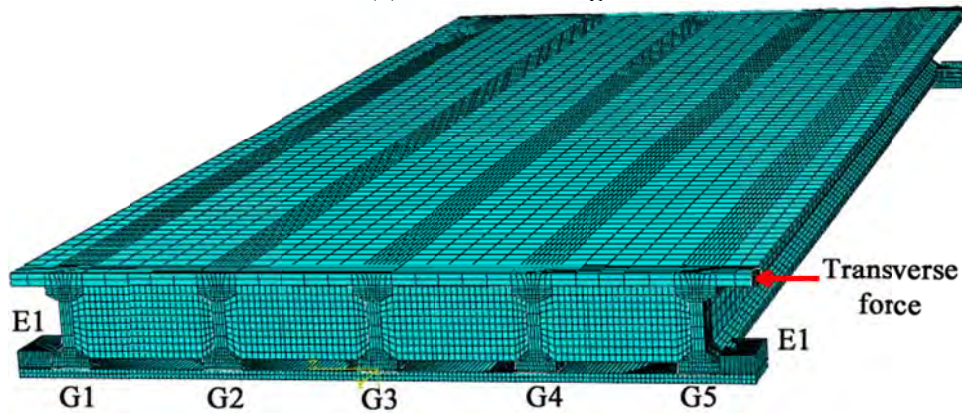
Fig. 3.1 Bridges installed with different heights of end diaphragms.

### 3.1.1 Installed diagram of full girder height

The FE model of bridge installed with full height end diaphragm is shown in Fig. 3.2. The five girders are represented by G1, G2, G3, G4, and G5, respectively; the two exterior shear keys are represented by E1 and E2, respectively. Different mesh densities were applied at different zones. Fine mesh is applied to the areas where surface-to-surface contact is defined to improve the computation accuracy; while coarse mesh is applied to improve the computation efficiency for zones where stress distributions are uniform.



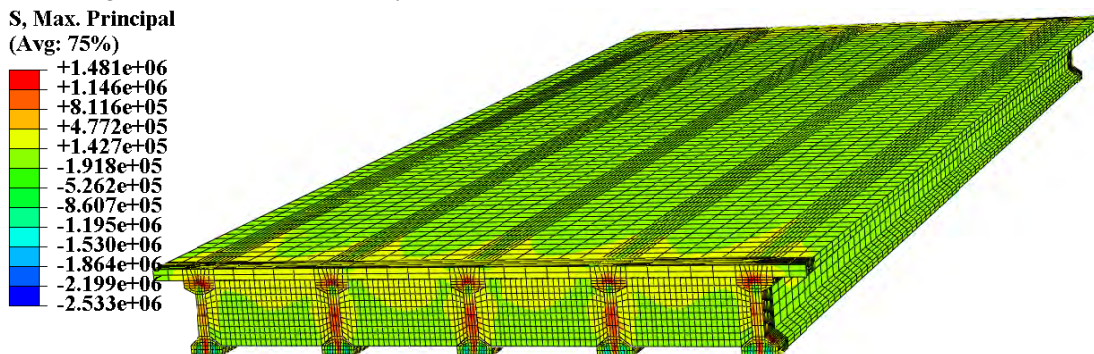
(a) Before meshing.



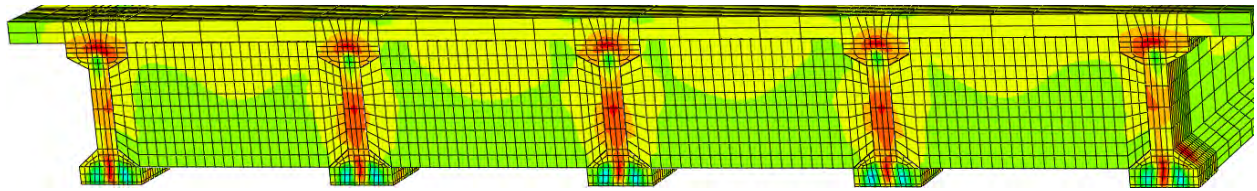
(b) After meshing.

**Fig. 3.2 A simplified FE model of bridge installed diaphragm of full girder height.**

Maximum principal stress distribution under self-weight and prestressing is shown in Fig. 3.3. Overall the stress is small, since the stress due to self-weight can be partially balanced by the prestressing. At each end of a girder, there is an anchorage zone where localized stresses are caused by the prestressed tendons. The localized stresses are larger than the overall stresses. Vertical deflection under self-weight and prestressing is shown in Fig. 3.4. The deflection distribution is overall symmetrical about the middle span in the longitudinal direction, and symmetrical about the G3 in the transverse direction.



(a) Top view of the superstructure.



(b) Zoom in the end diaphragm zone

Fig. 3.3 Maximum principal stress distribution under self-weight and prestressing.

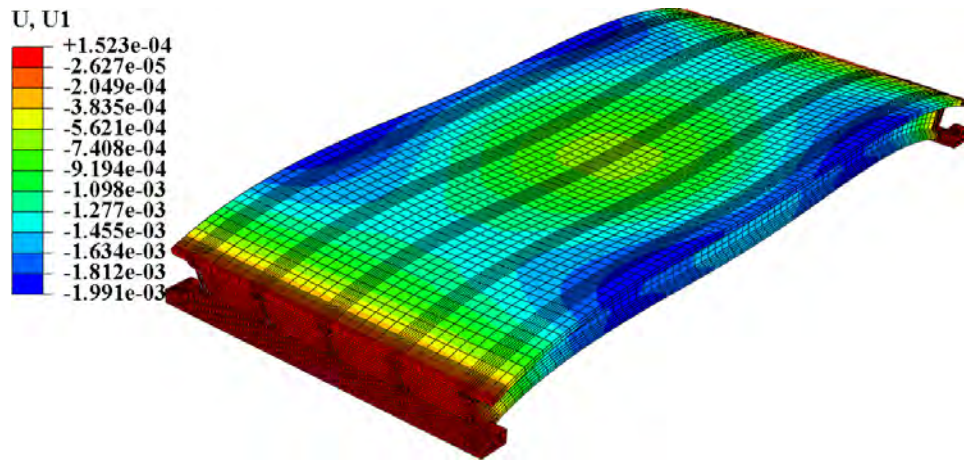
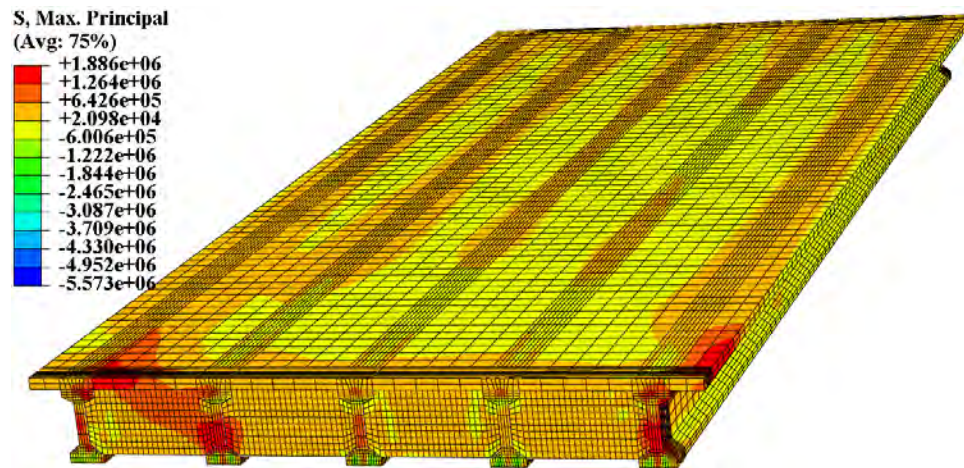
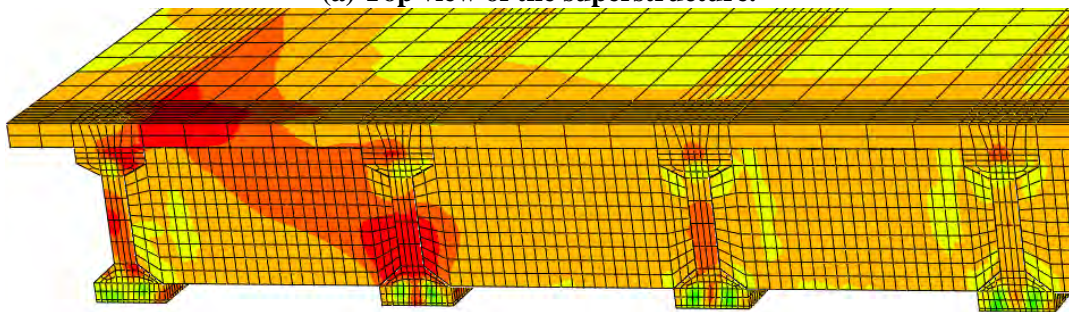


Fig. 3.4 Vertical deflection under self-weight and prestressing. ( $\times 500$ ).



(a) Top view of the superstructure.



(b) Zoom in the end diaphragm zone

Fig. 3.5 Maximum principal stress under self-weight, prestressing and transverse load. ( $\times 10$ ).

Maximum principal stress distribution under self-weight, prestressing, and transverse force is shown in Fig. 3.5. Exterior girder 'G1' and its adjacent zones are under high stress. Under transverse loading, the superstructure drifts and surface-to-surface contact is gradually established between G1 and the exterior shear key 'E1'. Then a contact force will be applied on G1 in the transverse direction and therefore the zones around G1 is under high stress. The corner of the deck where the transverse force is applied via a small cushion block is under high stress. This is a localized behavior that is related to the simulation method of the load. In a real world earthquake, inertia force is applied to the whole structure in terms of mass distribution instead of being concentrated at a corner, so localized behaviors associated with the loading method do not need to be taken into consideration.

With the increase of transverse load, cracks will be initiated at the top of the deck and the web of exterior girder simultaneously. The damage development process is shown in Fig. 3.6. The damage propagates in the deck and the end diaphragm, and will potentially go through the interior girders; the cracks in girders propagate along the longitudinal direction.

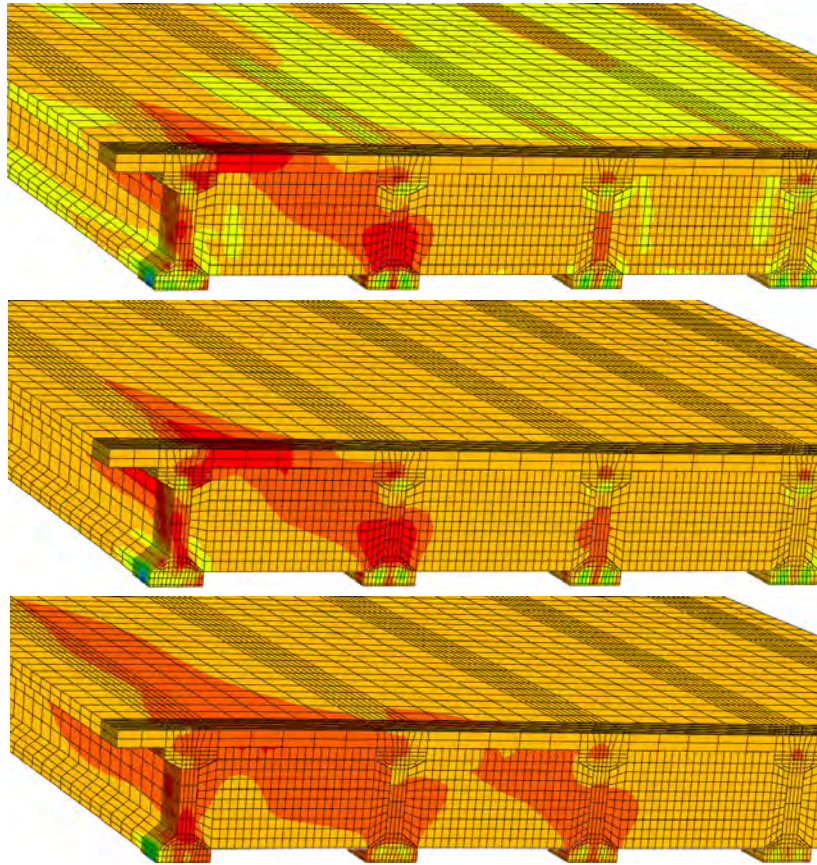


**Fig. 3.6 Damage development in the superstructure.**

Besides the concrete cracks, the bars reinforcing the concrete will gradually yield with the increase of load. Eventually the superstructure fails. The pushover curve is shown in Fig. 3.7. Onset of crack corresponds to 2 mm transverse drift. Then the structure will undergo a 'softening' stage representing the propagation of cracks in the concrete; however, the structure can resist higher load during that stage, because the concrete is reinforced by rebar that can provide tensile strength and restrain the cracking. With the propagation and widening of the cracks, eventually the rebar will yield and thus the structure will lose strength and fail.

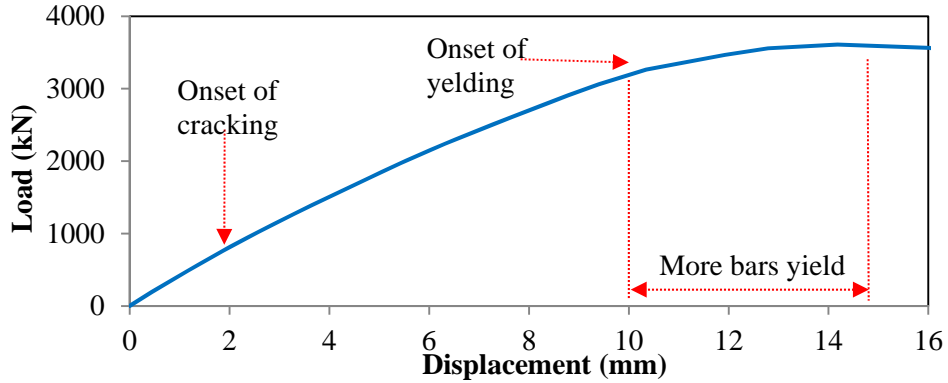


**Fig. 3.7 Pushover curve (Load-Displacement relation).**

Von Mises stress distributions in mild rebar and prestressed tendons are shown in Figs. 3.8 and 3.9, respectively. As introduced in Section 2, the yielding stress of mild rebar is 414 MPa (60 kips), the tensile strength of the prestressed tendons is 1860 MPa. Von Mises criterion is applied to control the yielding conditions. The yielding of mild rebar can be observed in Figs. 3.8 and 3.9; however, the prestressed tendons are working within the elastic range.

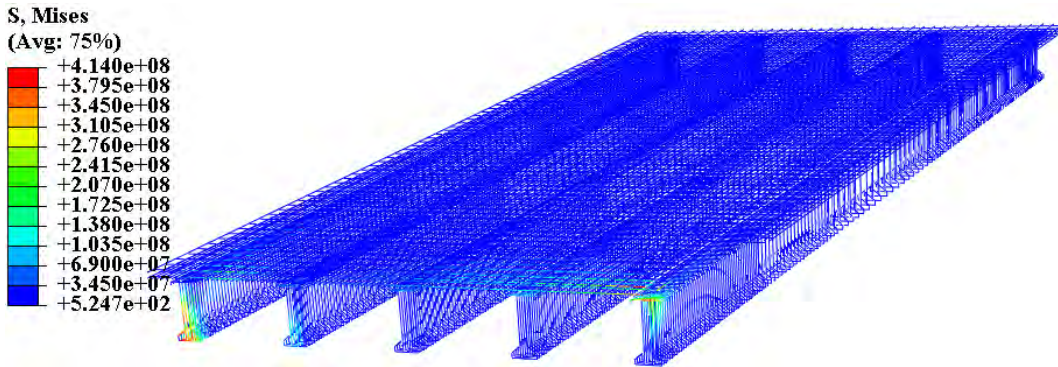


**Fig. 3.8 Von Mises stress in mild rebar. (×10).**



**Fig. 3.9 Von Mises stress in prestressed tendons. (×10).**

Vertical deflection under self-weight, prestressing, and transverse force is shown in Fig. 3.10. The deflection distribution is overall symmetrical about the middle span in the longitudinal direction; however, in the transverse direction, the deflection is not symmetrical about the G3. The superstructure drifts due to the transverse force; the end diaphragms are compressed and distorted, and the girders are bent due to the shear force caused by the contact between G1 and E1.

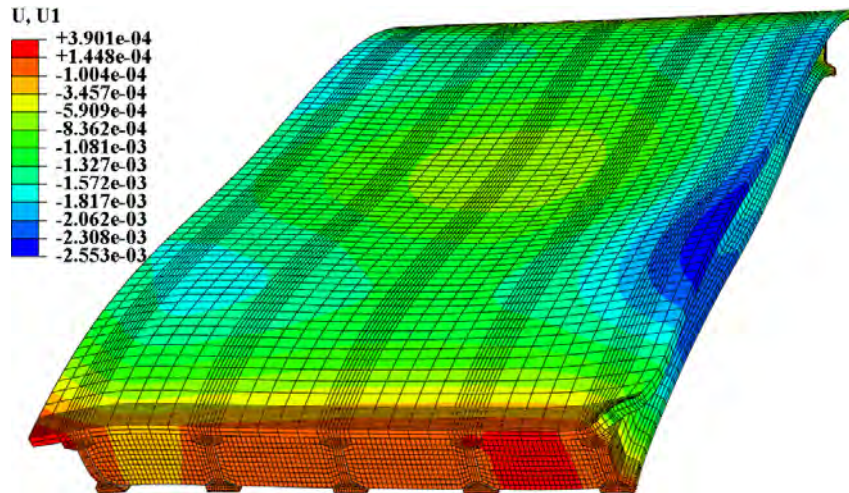


**Fig. 3.10 Vertical deflection under self-weight, prestressing, and transverse force. ( $\times 500$ ).**

### 3.1.2 Installed diagram of 75% girder height

The meshed FE model of bridge with 75% end diaphragm is shown in Fig. 3.11.

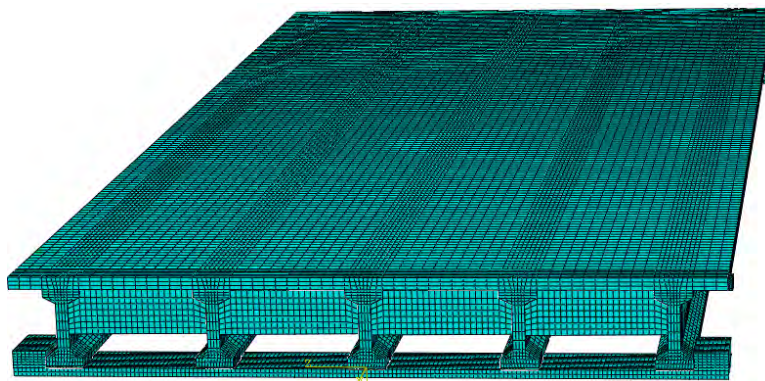


**Fig. 3.11 A simplified FE model of bridge installed diaphragm of 75% girder height.**

Maximum principal stress distribution under self-weight and prestressing is shown in Fig. 3.12. Vertical deflection under self-weight and prestressing is shown in Fig. 3.13. The deflection distribution is overall symmetrical about the middle span in the longitudinal direction, and symmetrical about the G3 in the transverse direction.

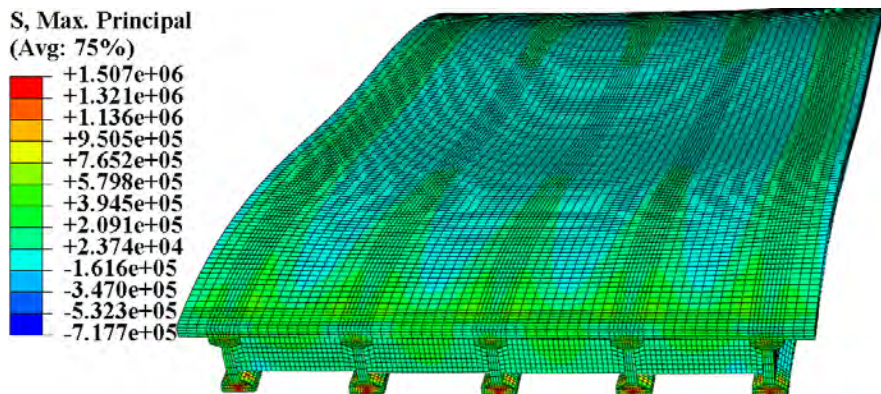


**Fig. 3.12 Maximum principal stress distribution under self-weight and prestressing. ( $\times 500$ ).**

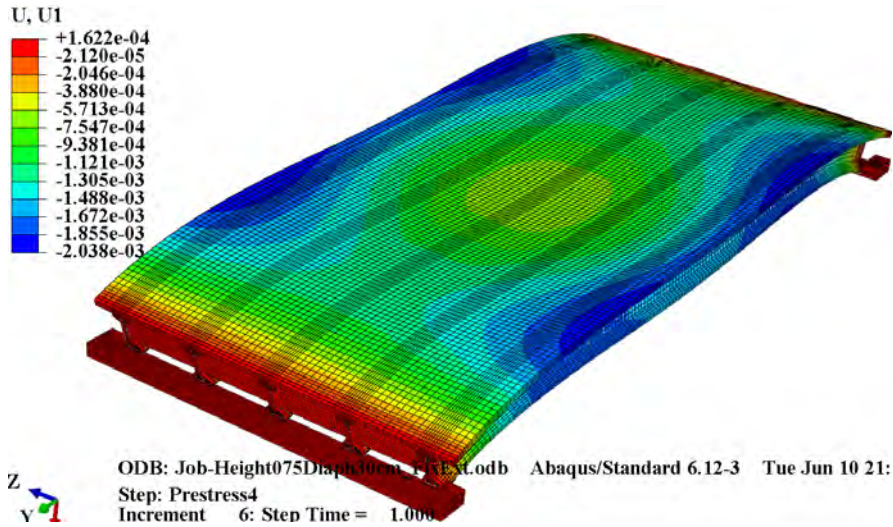


**Fig. 3.13 Vertical deflection under self-weight and prestressing. ( $\times 500$ ).**

Maximum principal stress distribution under self-weight, prestressing, and transverse force is shown in Fig. 3.14. The damage location is demonstrated to be in the exterior girder at the joint with the partial end diaphragm.

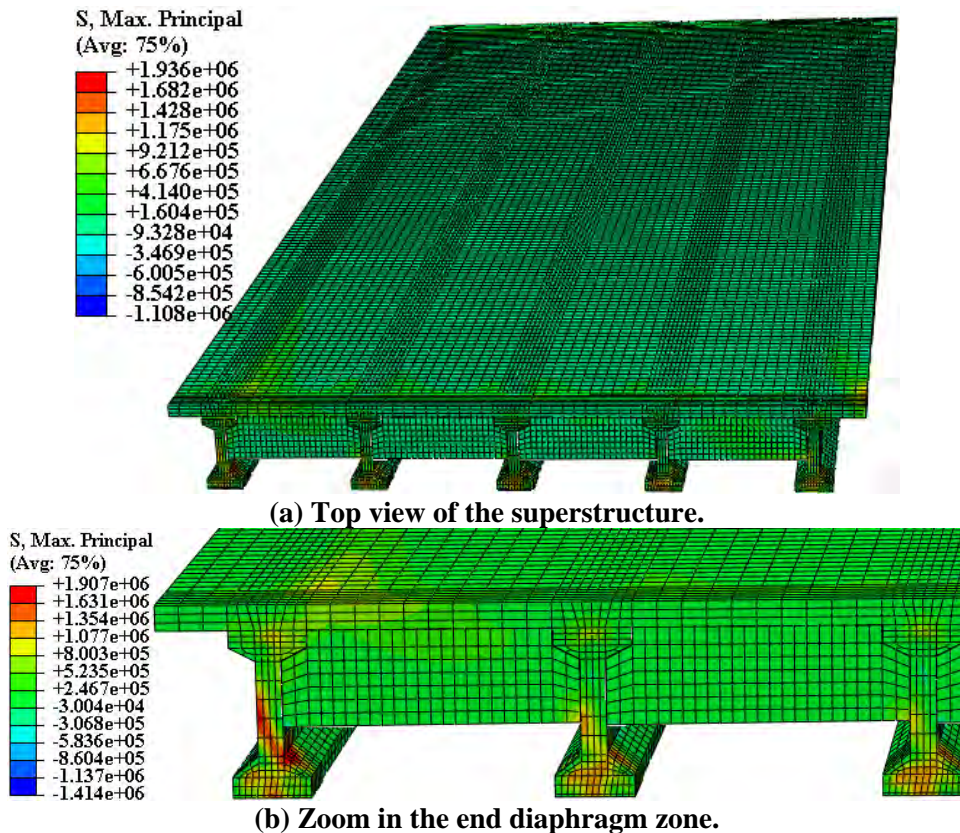


**Fig. 3.14 Maximum principal stress under self-weight, prestressing and transverse load.**

Fig. 3.15 shows the damage in San Nicholas Bridge after the 2010 Chile earthquake. San Nicholas Bridge is a reinforced concrete bridge with partial end diaphragm instrumented with seismic bars. The exterior girder was damaged at the joint with the partial end diaphragm during the earthquake, which is in good agreement with the simulation results.





**Fig. 3.15 San Nicholas bridge with partial diaphragms.**

The pushover curve is shown in Fig. 3.16. With the increase of loading, maximum principal stress/strain in concrete will increase until a crack is formed. Then the structure will undergo a ‘softening’ stage representing the propagation of cracks in the concrete. With the propagation and widening of the cracks, eventually the rebar will yield and thus the structure will lose strength and fail.

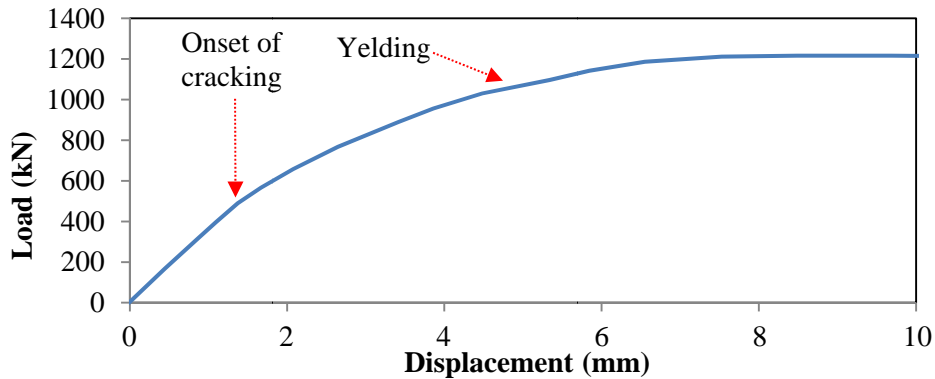


**Fig. 3.16 Pushover curve (Load-Displacement relation).**

Vertical deflection under self-weight, prestressing, and transverse force is shown in Fig. 3.17.

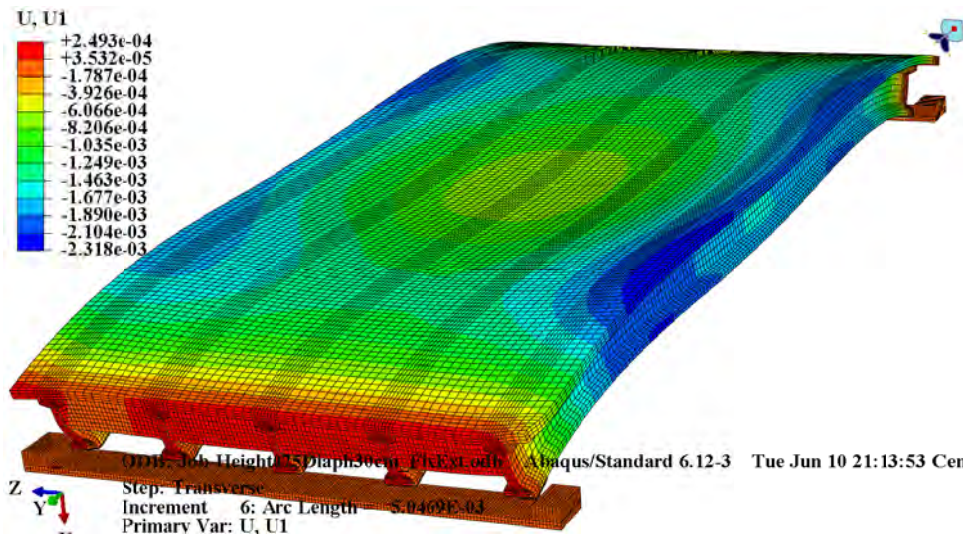
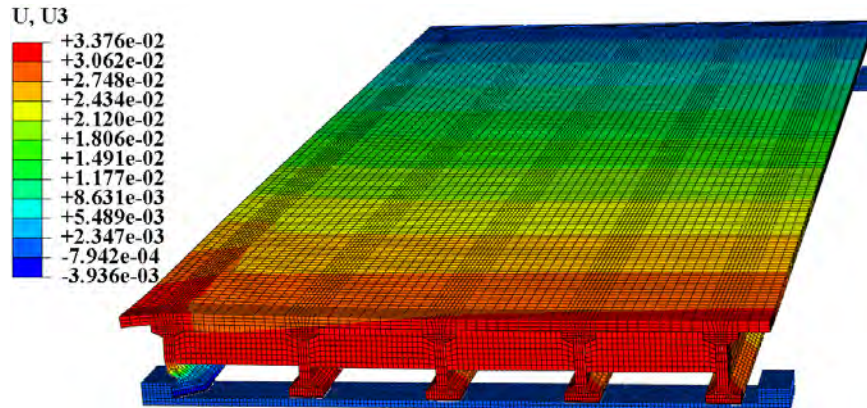


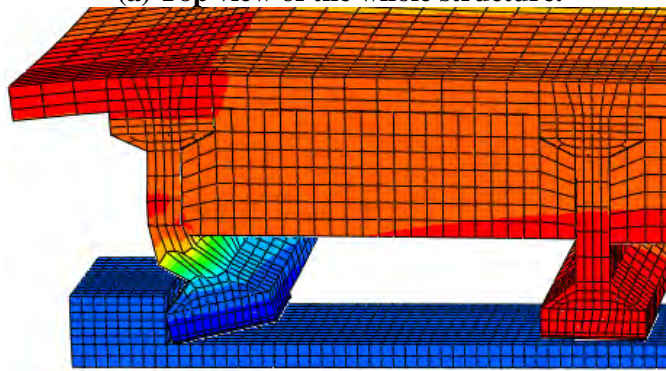
**Fig. 3.17 Vertical deflection under self-weight, prestressing, and transverse force. (×500).**

Transverse displacement distribution of the bridge under self-weight, prestressing, and transverse force is shown in Fig. 3.18. Overall the whole superstructure shifted in the transverse direction due to the transverse load, except for the end of G1 which was restrained by the exterior shear key. The end

diaphragm was stiff in its plane; hence, the zones that were reinforced by the diaphragms were stiff and thus demonstrated relatively small displacement.



(a) Top view of the whole structure.



(b) Zoom in the deformed exterior girder.

Fig. 3.18 Transverse drift under self-weight, prestressing, and transverse force. ( $\times 10$ ).

### 3.1.3 Installed diagram of 50% girder height

The meshed FE model of bridge with 50% end diaphragm is shown in Fig. 3.19.

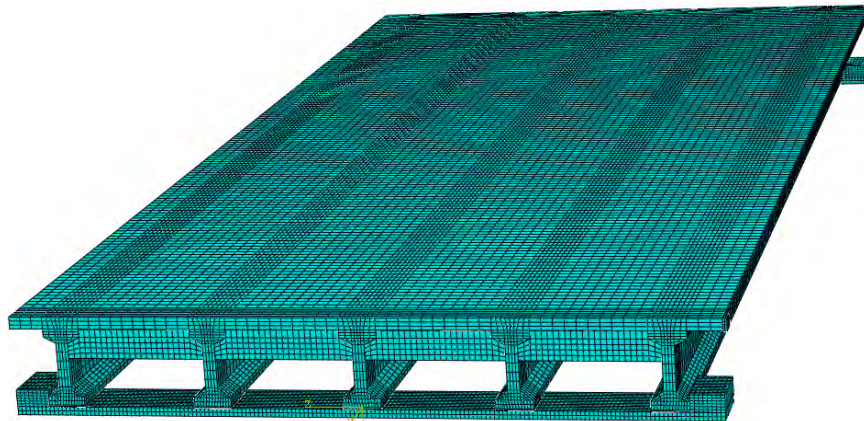


Fig. 3.19 A simplified FE model of bridge installed diaphragm of 50% girder height.

Maximum principal stress distribution under self-weight and prestressing is shown in Fig. 3.20. Vertical deflection under self-weight and prestressing is shown in Fig. 3.21. Compared with the bridge with full end diaphragms, the bridge with partial end diaphragms demonstrated similar stress and displacement results under self-weight and prestressing.

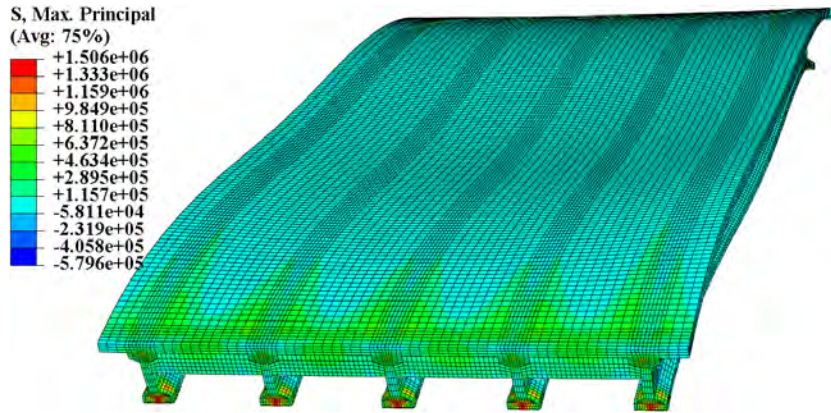


Fig. 3.20 Maximum principal stress under self-weight and prestressing. ( $\times 500$ ).

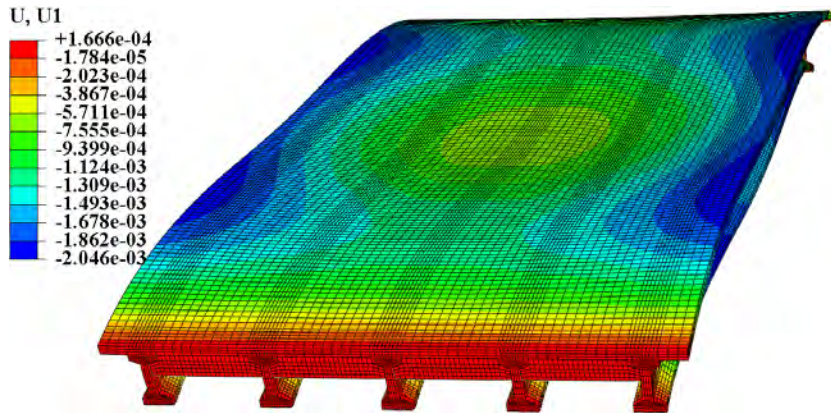
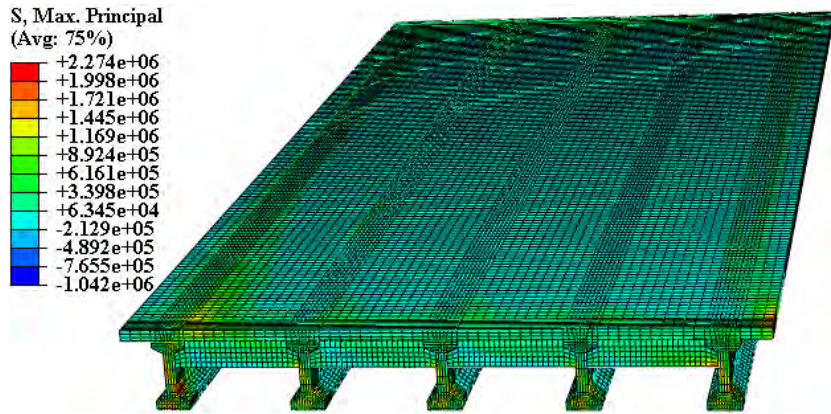
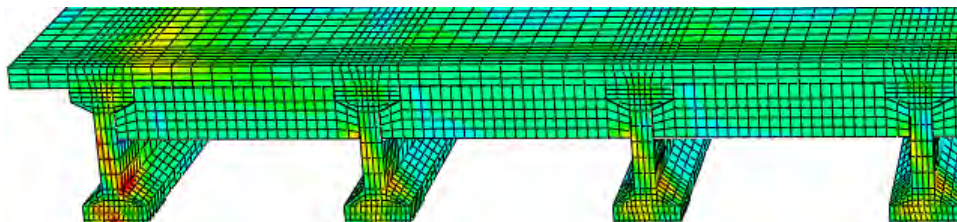


Fig. 3.21 Vertical deflection under self-weight and prestressing. ( $\times 500$ ).

Maximum principal stress distribution under self-weight, prestressing, and transverse force is shown in Fig. 3.22. The pushover curve is shown in Fig. 3.23.

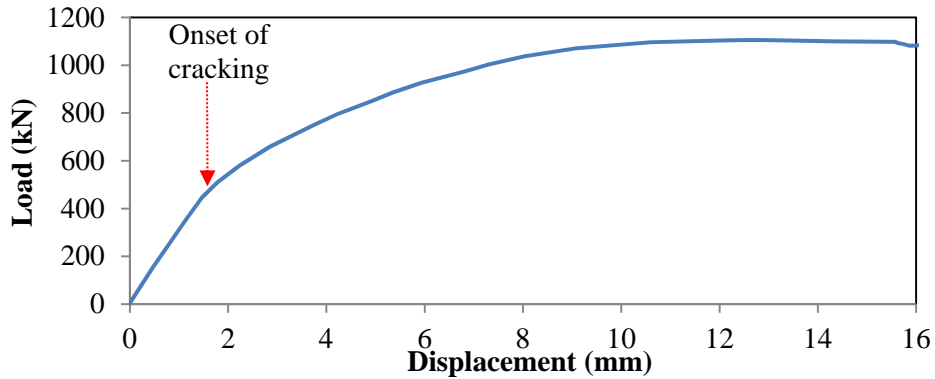


(a) Top view of the superstructure.



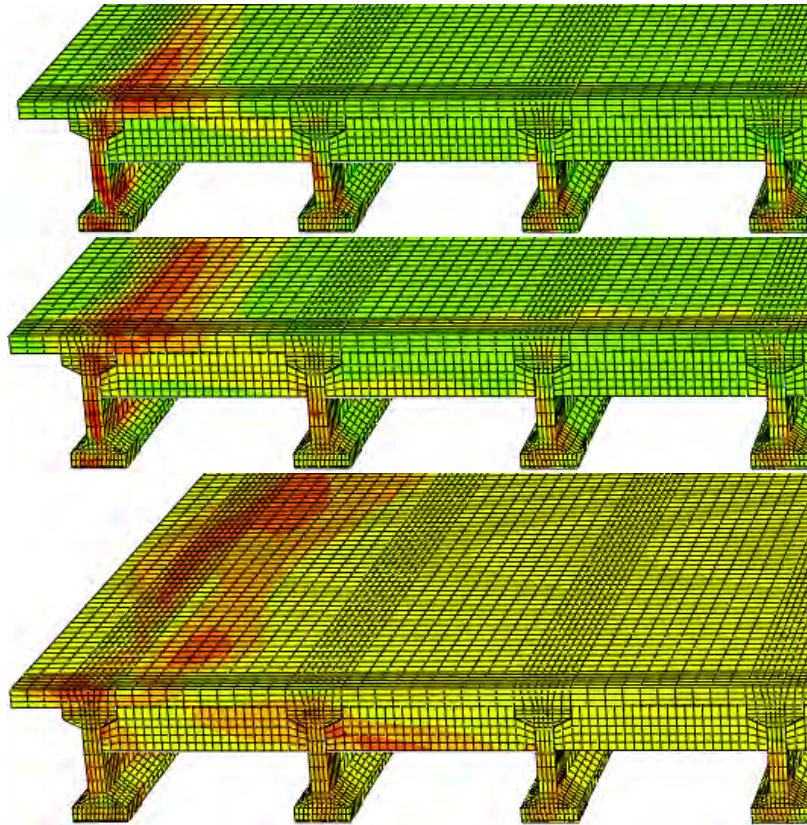
(b) Zoom in the end diaphragm zone.

**Fig. 3.22 Maximum principal stress under self-weight and prestressing.**



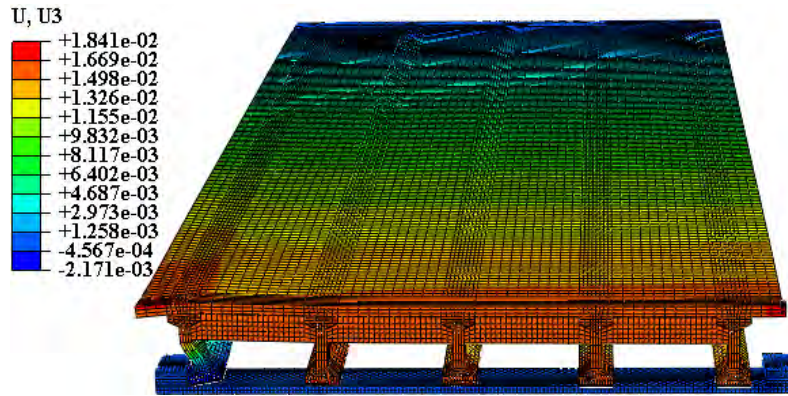
**Fig. 3.23 Pushover curve (Load-Displacement relation).**

Fig. 3.22 shows that cracking initiates at the top of the deck and the web of exterior girder simultaneously. The damage development is shown in Fig. 3.24. The damage propagates in the deck and the end diaphragm, and will potentially go through the interior girders; the cracks in girders propagate along the longitudinal direction. The damage behavior demonstrated is in good agreement with the damage observed in the San Nicholas bridge shown in Fig. 3.12.

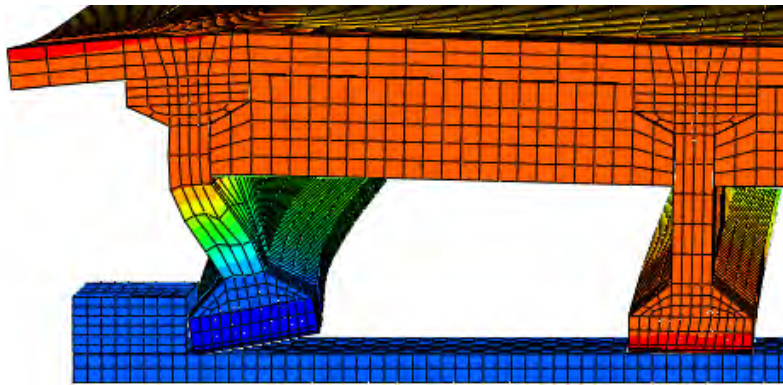


**Fig. 3.24 Damage development in the superstructure.**

Transverse displacement of the bridge under self-weight, prestressing, and transverse force is shown in Fig. 3.25. Similar to Fig. 3.18, overall the whole superstructure shifted in the transverse direction due to the transverse load, except for the end of G1 which was restrained by the exterior shear key. The end diaphragm was stiff in its plane; hence, the zones that were reinforced by the diaphragms were stiff and thus demonstrated relatively small displacement.



(a) Top view of the whole structure.



(b) Zoom in the deformed exterior girder.

Fig. 3.25 Lateral displacement under self-weight, prestressing, and transverse force. ( $\times 10$ ).

### 3.1.4 Installed diagram of 25% girder height

The meshed FE model of bridge with 25% end diaphragm is shown in Fig. 3.26.

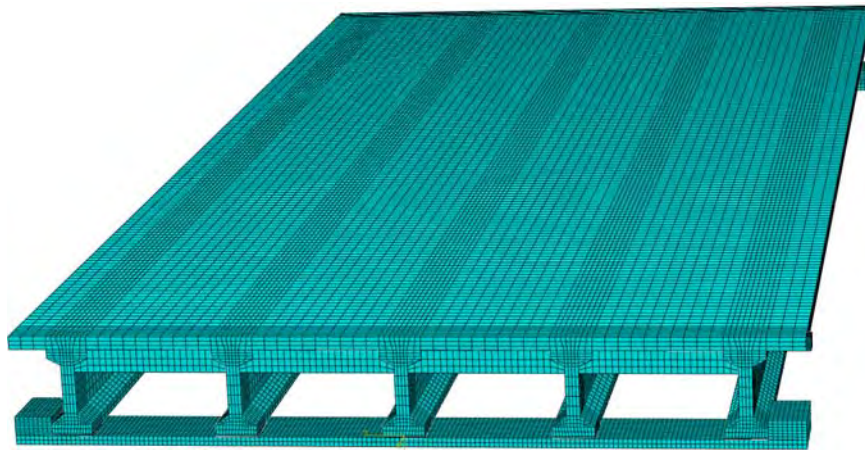


Fig. 3.26 A simplified FE model of bridge installed diaphragm of 25% girder height.

Maximum principal stress distribution under self-weight and prestressing is shown in Fig. 3.27. Vertical deflection under self-weight and prestressing is shown in Fig. 3.28. Compared with the bridge with full end diaphragms, under self-weight and prestress, the bridge with partial end diaphragms demonstrated similar stress and displacement results in terms of the distribution and magnitude.

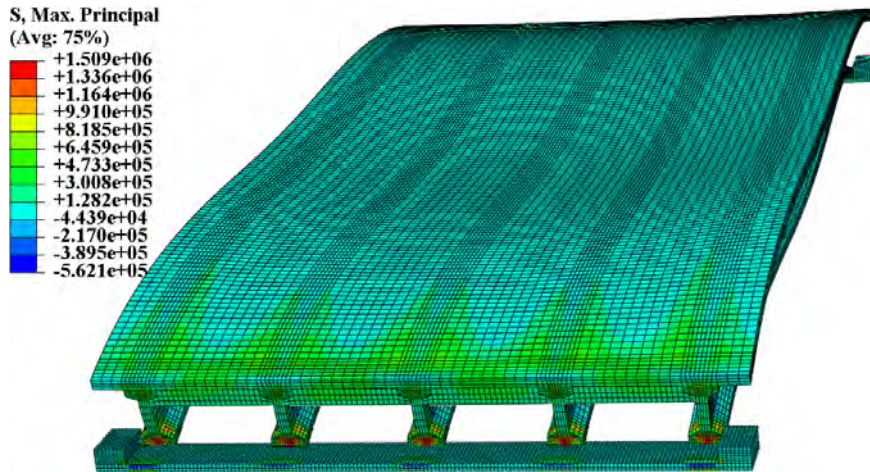


Fig. 3.27 Maximum principal stress distribution under self-weight and prestressing. ( $\times 500$ ).

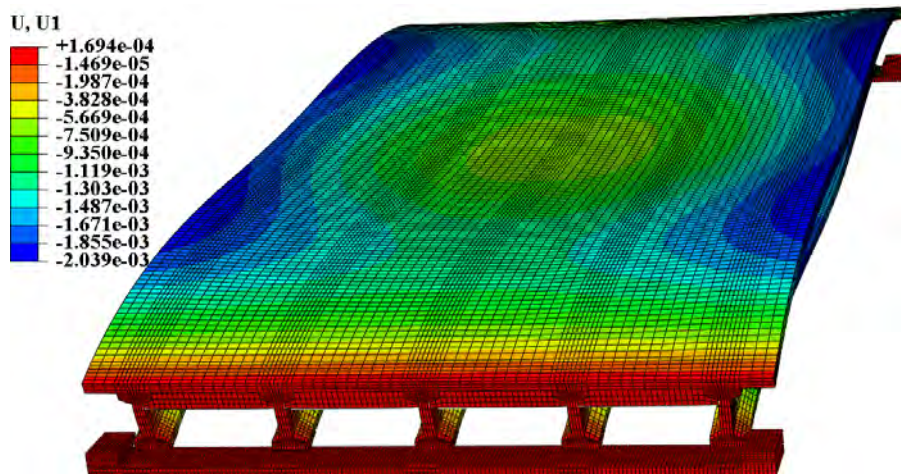


Fig. 3.28 Vertical deflection under self-weight and prestressing. ( $\times 500$ ).

Maximum principal stress distribution under self-weight, prestressing, and transverse force is shown in Fig. 3.1.29.

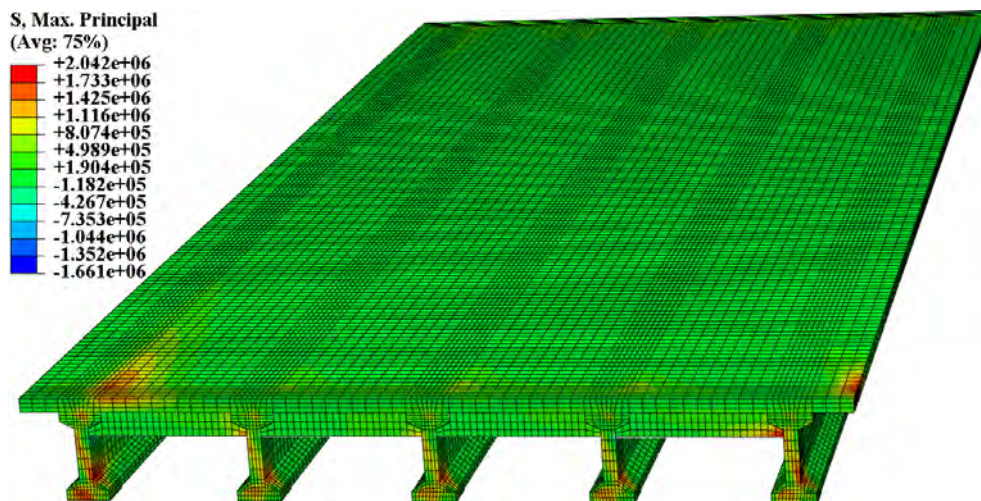
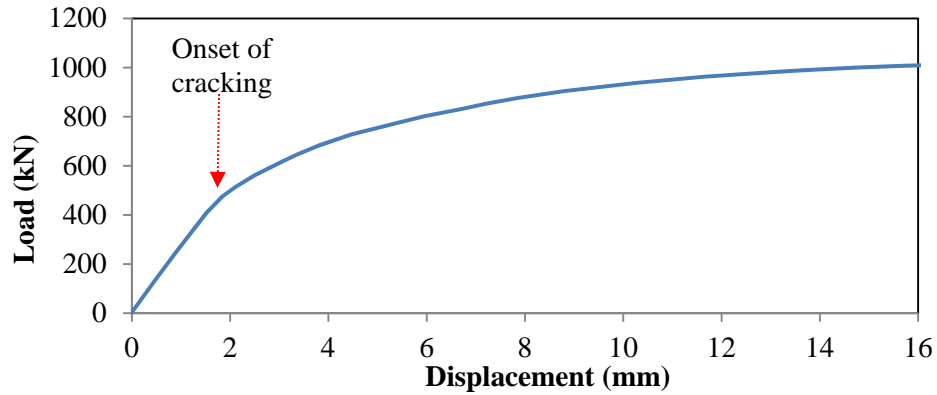


Fig. 3.29 Maximum principal stress under self-weight and prestressing.



**Fig. 3.30 Pushover curve (Load-Displacement relation).**

The pushover curve is shown in Fig. 3.30. After the contact between E1 and G1 is established, reaction force will be applied to G1. With the increase of loading, maximum principal stress/strain in concrete will increase until crack is formed. Then the structure will undergo a ‘softening’ stage representing the propagation of cracks in the concrete; however, the structure can resist higher load during that stage, because the concrete is reinforced by rebar that can provide tensile strength and restrain the cracking. With the propagation and widening of the cracks, eventually the rebar will yield and thus the structure will lose strength and fail.

Fig. 3.29 shows that cracking initiates at the top of the deck and the web of exterior girder simultaneously. The damage development is shown in Fig. 3.31. The damage propagates in the deck and the end diaphragm, and will potentially go through the interior girders; the cracks in girders propagate along the longitudinal direction. The damage behavior demonstrated is in good agreement with the damage observed in the San Nicholas bridge shown in Fig. 3.12.

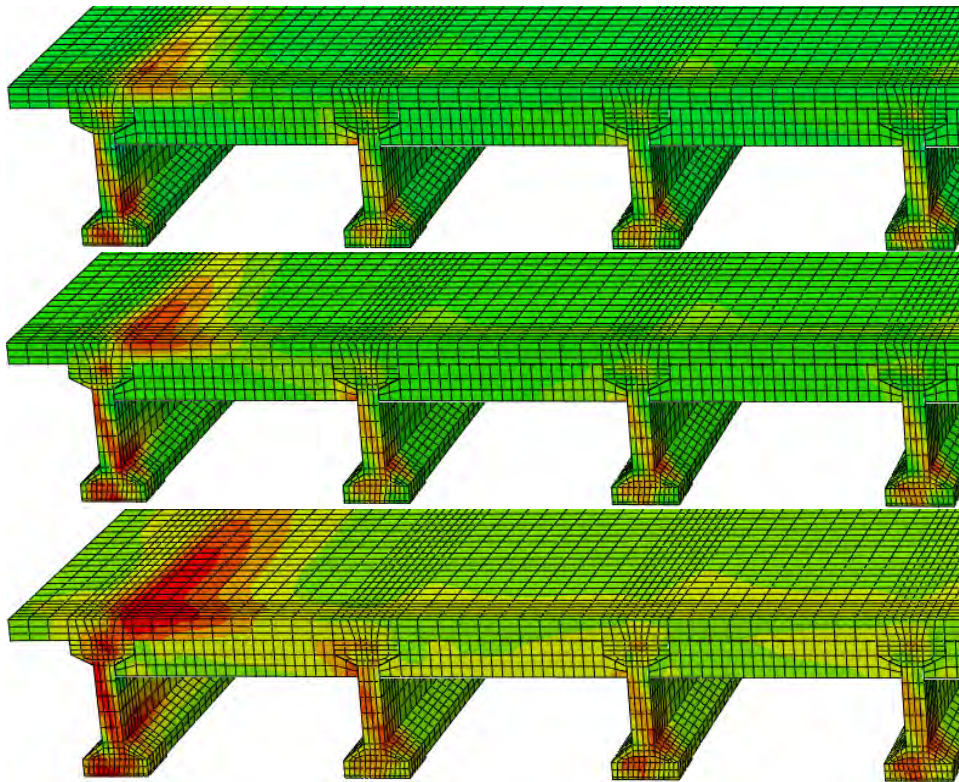


**Fig. 3.31 Damage development in the superstructure.**

Vertical deflection under self-weight, prestressing, and transverse force is shown in Fig. 3.32.

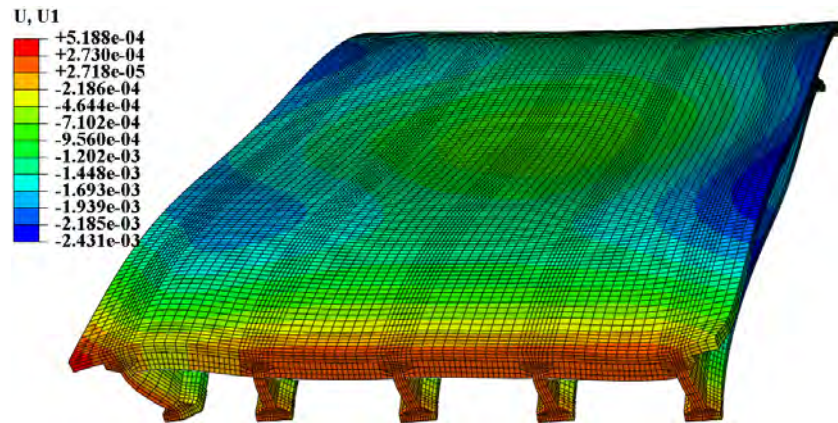


Fig. 3.32 Vertical deflection under self-weight, prestressing, and transverse force. ( $\times 500$ ).

### 3.1.5 Discussion on diaphragm height

The influence of end diaphragm height on vertical deflection and maximum principal stress of bridge superstructures under self-weight and prestressing is shown in Fig. 3.33 that indicates the diaphragm height does not significantly influence the bridge’s vertical behaviors. In Fig. 3.33, ‘0%’ represents the bridge without diaphragm.

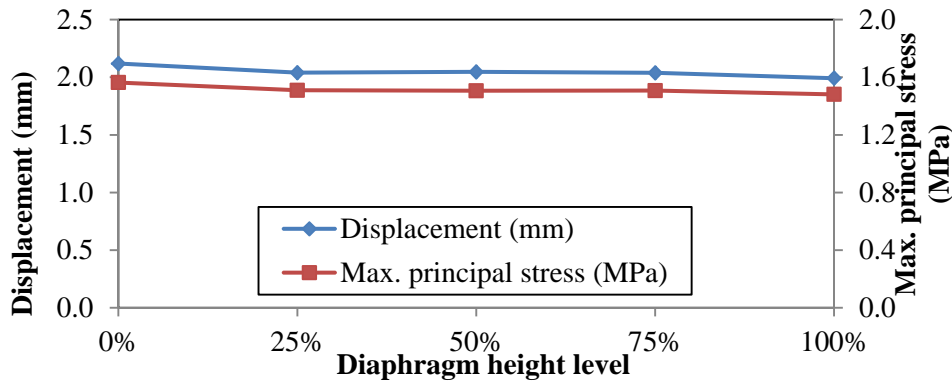


Fig. 3.33 Influence of diaphragm height on vertical behaviors.

The diaphragm height significantly influences bridge’s transverse performance, including the failure mode, the transverse stiffness and capacity. The failure modes have been introduced in the preceding sections. For a bridge with full diaphragm, cracks initiate in the exterior concrete girder and the joint of deck and end diaphragm; however, for bridges with partial diaphragms, cracks most often initiate in an exterior girder. Fig. 3.34 shows the influence on transverse stiffness and capacity. With the increase of diaphragm height, the stiffness and capacity increase, as shown in Fig. 3.34. Therefore, under the same conditions, bridges with partial diaphragm usually suffer more than the bridges with full diaphragms, as demonstrated in Fig. 1.1.



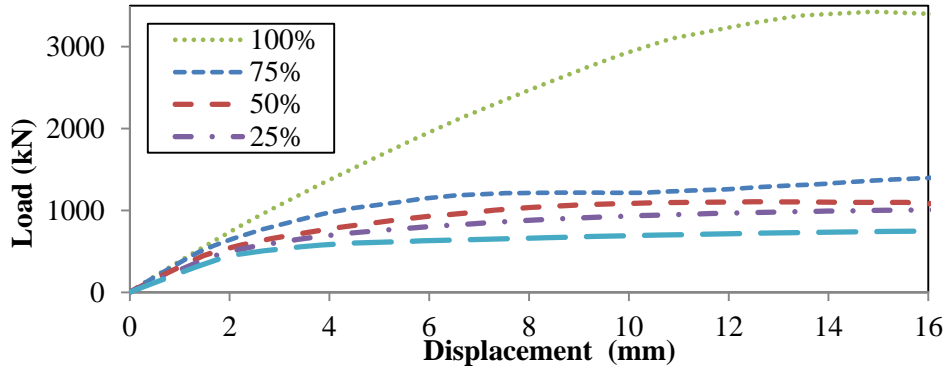


Fig. 3.34 Comparison of pushover curves of bridges with different diaphragm heights.

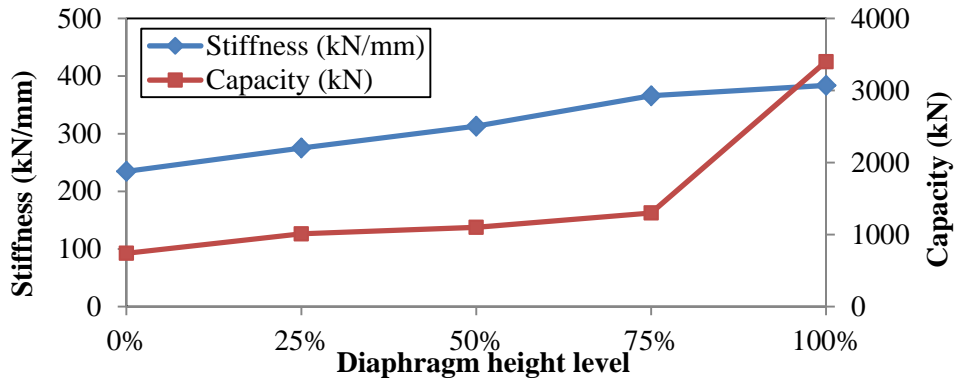


Fig. 3.35 Influence of diaphragm height on transverse behaviors.

### 3.2 Parametric Study of Diaphragm Thickness

Five cases corresponding to five levels of end diaphragm thickness were investigated, including 50 cm, 40 cm, 30 cm, 20 cm, and 10 cm. The diaphragms have full height as shown in Fig. 3.36.

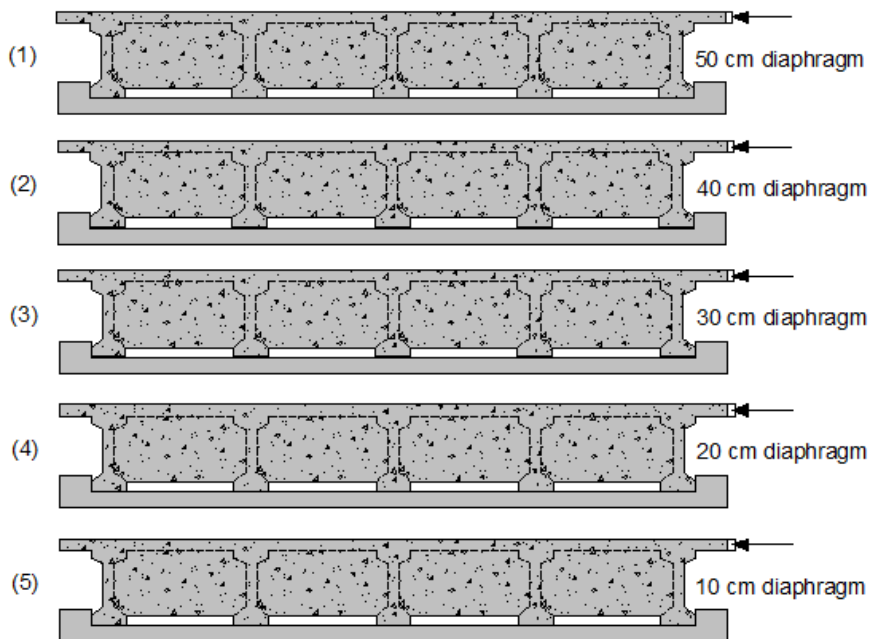
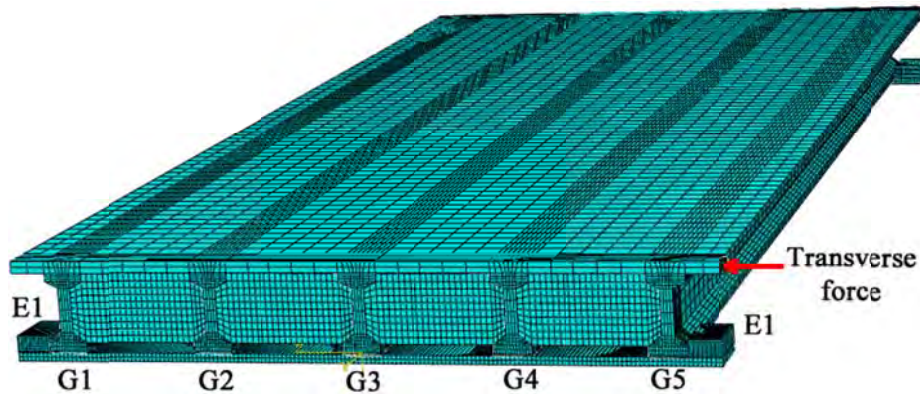


Fig. 3.36 Bridges with different heights of end diaphragms.

### 3.2.1 Installed 50 cm diaphragm

The FE model of bridge that has full end diaphragm with 50 cm thickness is shown in Fig. 3.37.



**Fig. 3.37** A simplified FE model of bridge installed diaphragm of 50 cm thickness.

Maximum principal stress distribution under self-weight and prestressing force is shown in Fig. 3.38. Vertical deflection under self-weight and prestressing force is shown in Fig. 3.39.

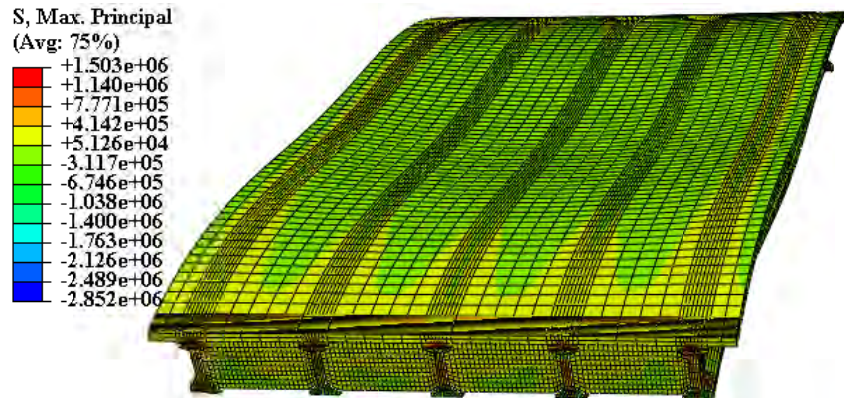


**Fig. 3.38** Maximum principal stress distribution under self-weight and prestressing force. ( $\times 500$ ).

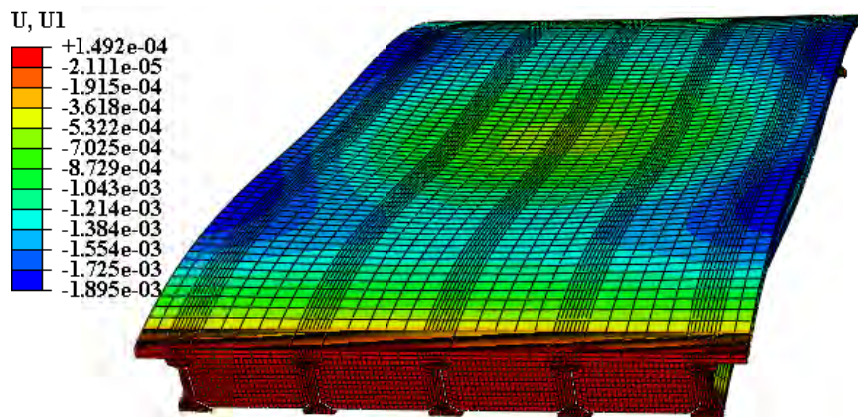


**Fig. 3.39** Vertical deflection under self-weight and prestressing force. ( $\times 500$ ).

Maximum principal stress distribution under self-weight, prestressed tendons and transverse force is shown in Fig. 3.40. Vertical deflection under self-weight, prestressing, and transverse force is shown in Fig. 3.41.

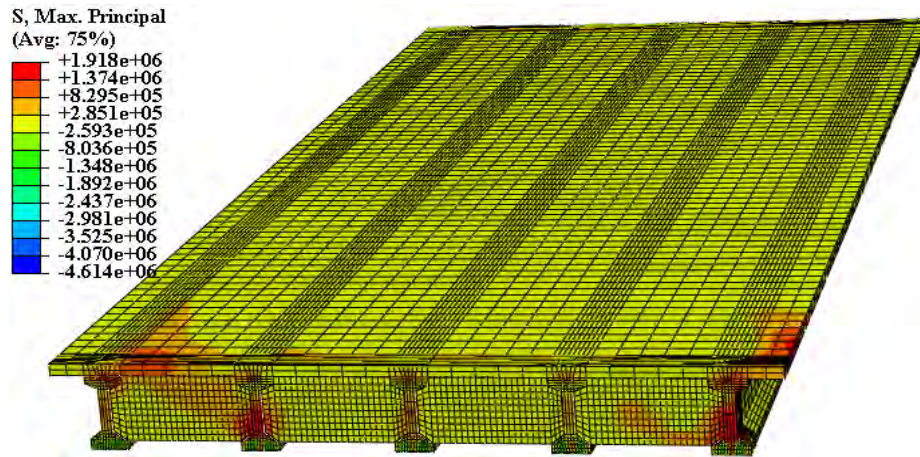


**Fig. 3.40** Maximum principal stress under self-weight, prestressing, and transverse force.

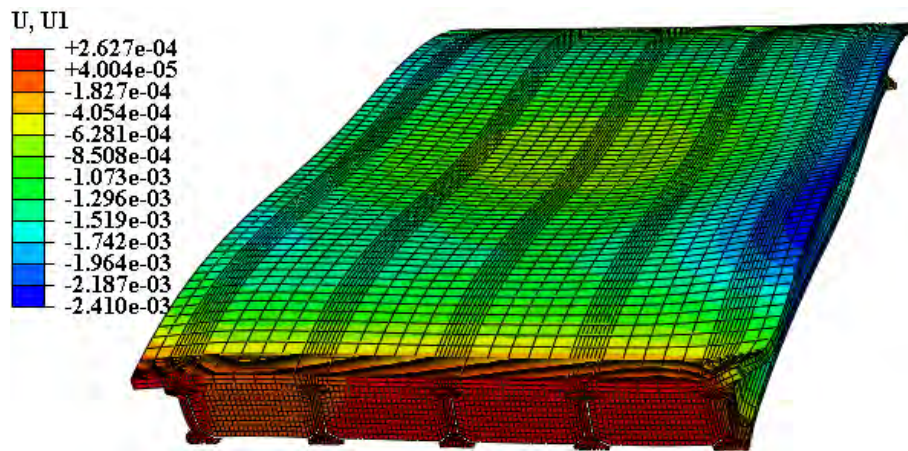


**Fig. 3.41** Vertical deflection under self-weight, prestressing, and transverse force. ( $\times 500$ ).

The load-displacement curve is shown in Fig. 3.42. At the beginning of the loading, the materials were elastic, and thus the displacement increased linearly with the load. When the stress/strain in concrete reached the elastic limit, crack would appear at the high stress zones shown in Fig. 3.40, and then the load-displacement curve would be nonlinear. A three-dimensional critical failure section was gradually formed. The decrease of slope represented the reduction of the superstructure's transverse stiffness, which was caused by the propagation of damage. During this damaging process, the rebar held the concrete and restrained the development of cracks, so stress in rebar would gradually increase until yielding. Because the structure had multiple reinforcements, it would not fail at the onset of yield. Eventually, all rebar that went across the critical section yielded; the stiffness became negative and the superstructure could not resist larger load.

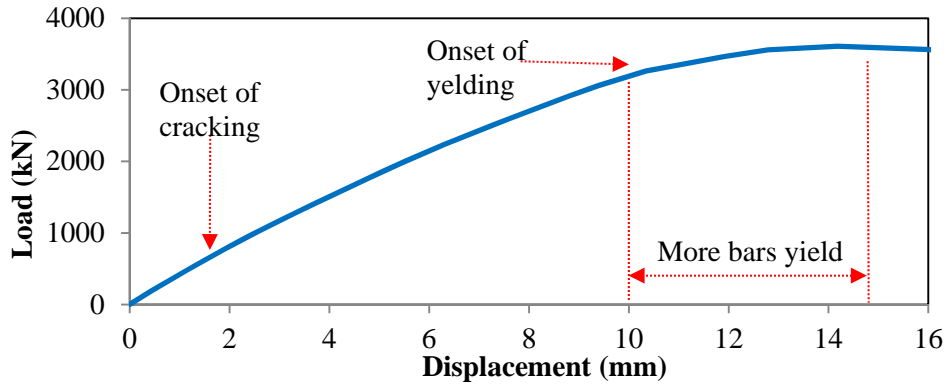


Fig. 3.42 Pushover curve (Load-Displacement relation).

### 3.2.2 Installed 40 cm diaphragm

The FE model corresponding to 40 cm end diaphragms is similar to the model shown in Fig. 3.37. Maximum principal stress distribution under self-weight and prestressing force is shown in Fig. 3.43, and vertical deflection under self-weight and prestressing force is shown in Fig. 3.44. The results are similar to the bridge with 50 cm end diaphragm discussed in the last section.

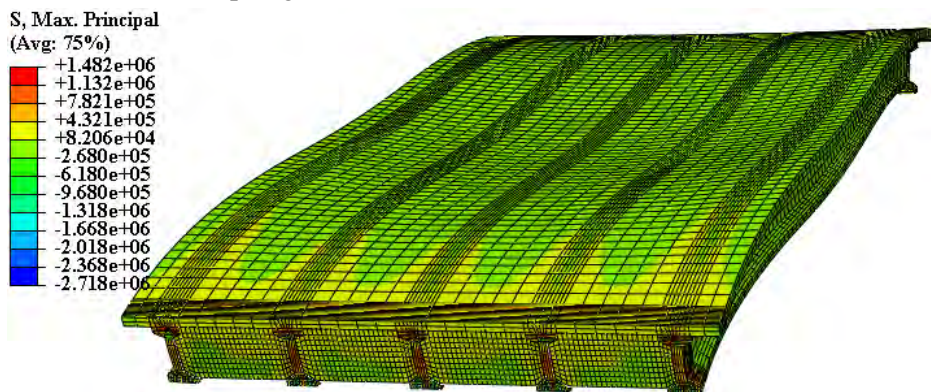


Fig. 3.43 Maximum principal stress under self-weight and prestressing. ( $\times 500$ ).

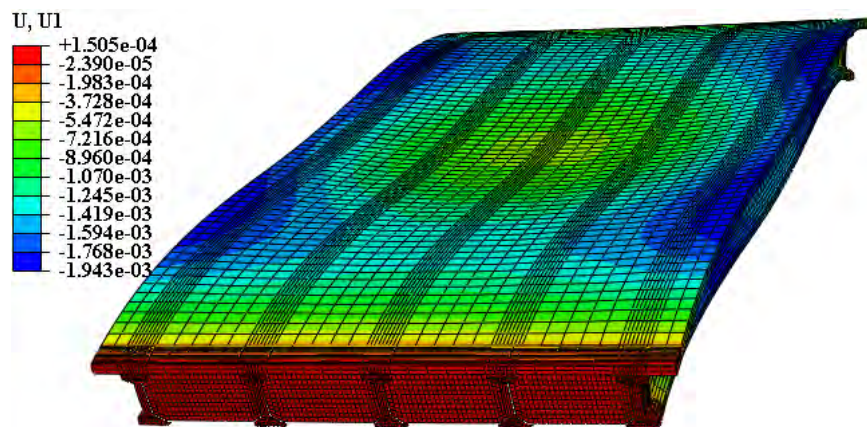
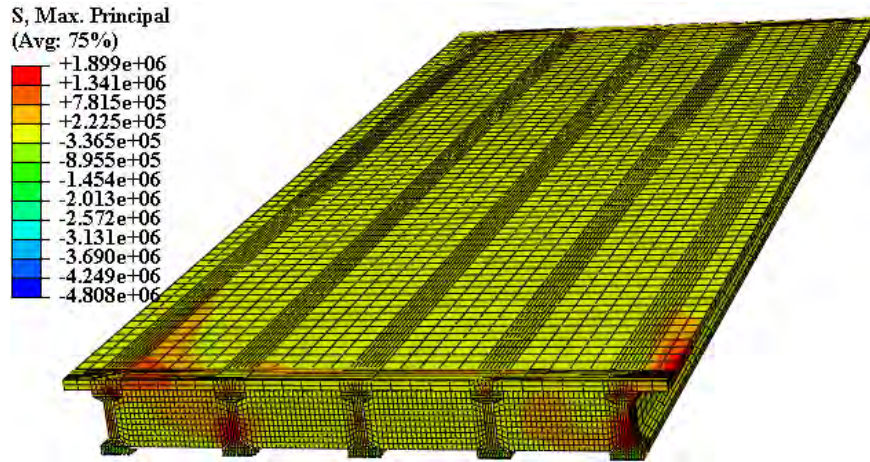


Fig. 3.44 Vertical deflection under self-weight and prestressing. ( $\times 500$ ).

Maximum principal stress distribution under self-weight, prestressed tendons and transverse force is shown in Fig. 3.45. Similar to Fig. 3.40, two high stress level zones can be observed. One zone was in the exterior girder 'G5' where the transverse force was applied and this was a localized behavior that would

not happen in the real earthquake. The other high stress level zone was at the joint of exterior girder 'G1' and an end diaphragm, which was the same as the bridge with 50 cm end diaphragms.



**Fig. 3.45 Maximum principal stress under self-weight, prestressing, and transverse force. ( $\times 10$ ).**

Vertical deflection under self-weight, prestressing, and transverse force is shown in Fig. 3.46. The deflection distribution was overall symmetrical about the middle span in the longitudinal direction; however, in the transverse direction, the superstructure was distorted by the transverse load and thus it was not symmetrical about G3. The superstructure shifted due to the transverse force; the end diaphragms were compressed and distorted, and the girders were bent due to the shear force caused by the contact with the exterior shear key E1.

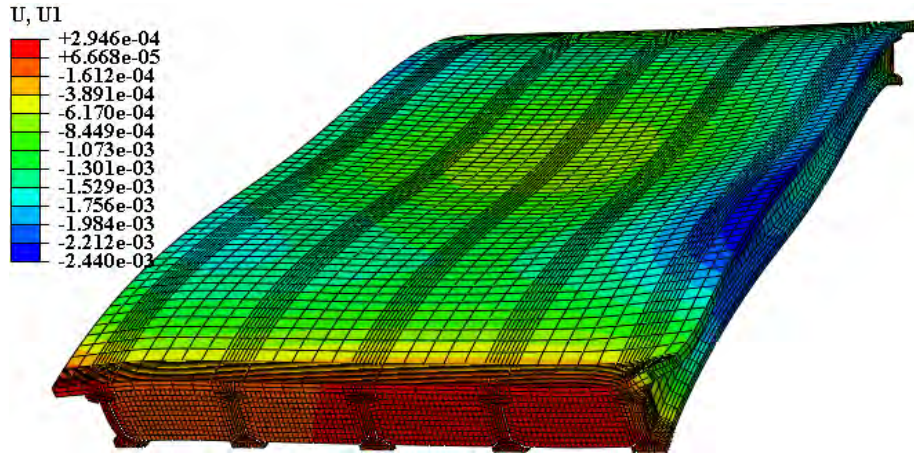


**Fig. 3.46 Vertical deflection under self-weight, prestress, and transverse force. ( $\times 500$ ).**

The load-displacement curve was shown in Fig. 3.47 that was similar to that of the bridge with 50 cm diaphragms, and it showed similar behaviors.

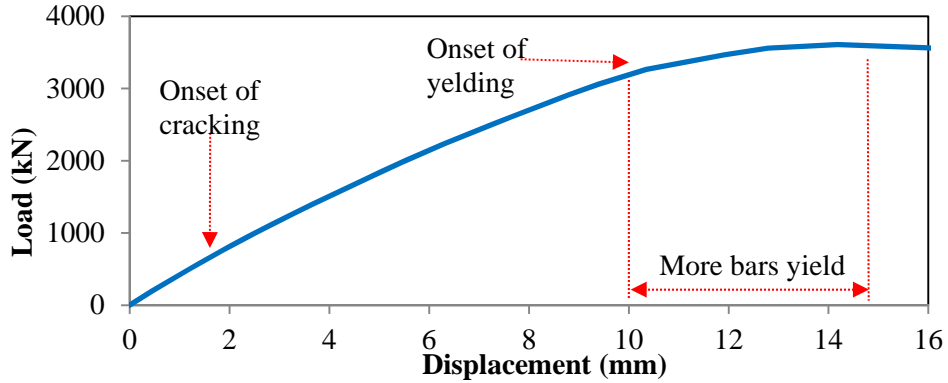


**Fig. 3.47 Pushover curve (Load-Displacement relation).**

### 3.2.3 Installed 30 cm diaphragm

The analysis for bridge with 30 cm end diaphragms has been introduced in Section 3.1 and thus will not be repeated.

### 3.2.4 Installed 20 cm diaphragm

The FE model corresponding to 40 cm end diaphragms is similar to the model shown in Fig. 3.37. Maximum principal stress distribution under self-weight and prestressing force is shown in Fig. 3.48, and vertical deflection under self-weight and prestressing force is shown in Fig. 3.49.

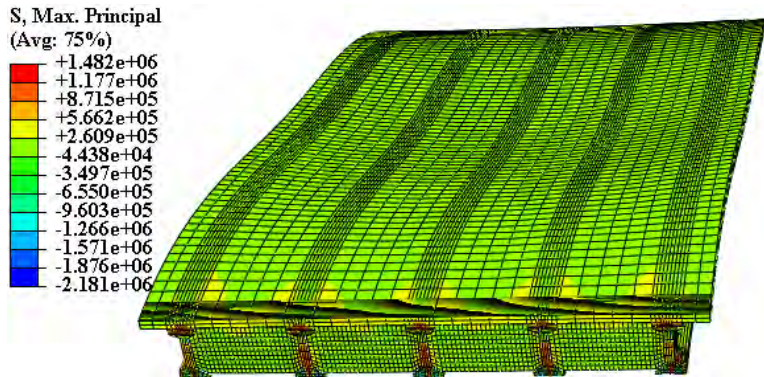


**Fig. 3.48 Maximum principal stress distribution under self-weight and prestressing. ( $\times 500$ ).**

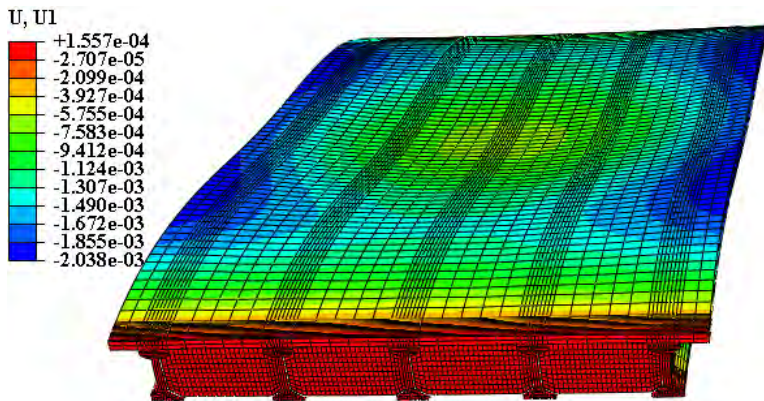


**Fig. 3.49 Vertical deflection under self-weight and prestressing. ( $\times 500$ ).**

Maximum principal stress distribution under self-weight, prestressed tendons and transverse force is shown in Fig. 3.50. Two high stress level zones can be observed. One zone was the vicinity of exterior

girder 'G5'. The other high stress level zone was at the joint of exterior girder 'G1' and an end diaphragm, which was the same as the bridge with 50 cm end diaphragms.

The deflection distribution was overall symmetrical about the middle span in the longitudinal direction; however, in the transverse direction, the superstructure was distorted by the transverse load and thus it was not symmetrical about G3. The superstructure shifted due to the transverse force; the end diaphragms were compressed and distorted, and the girders were bent due to the shear force caused by the contact with the exterior shear key E1.

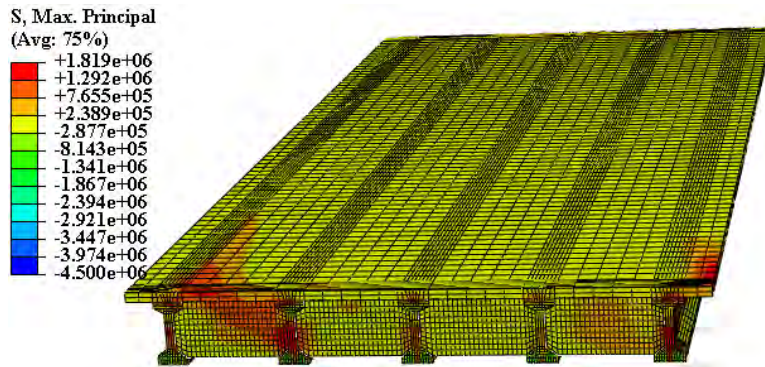


Fig. 3.50 Maximum principal stress under self-weight, prestressing, and transverse force.

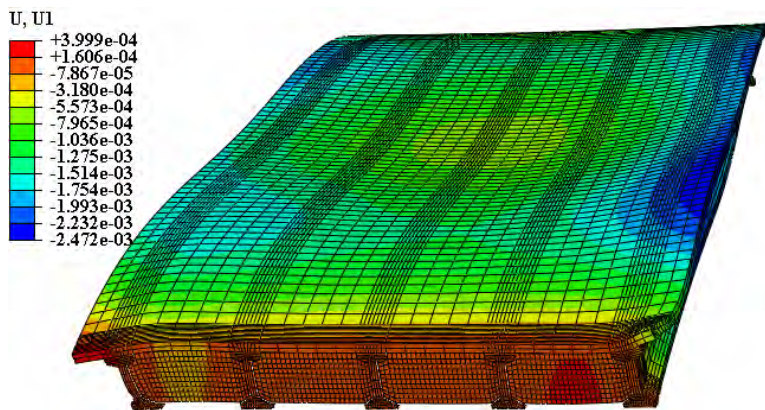


Fig. 3.51 Vertical deflection under self-weight, prestressing, and transverse force. ( $\times 500$ ).

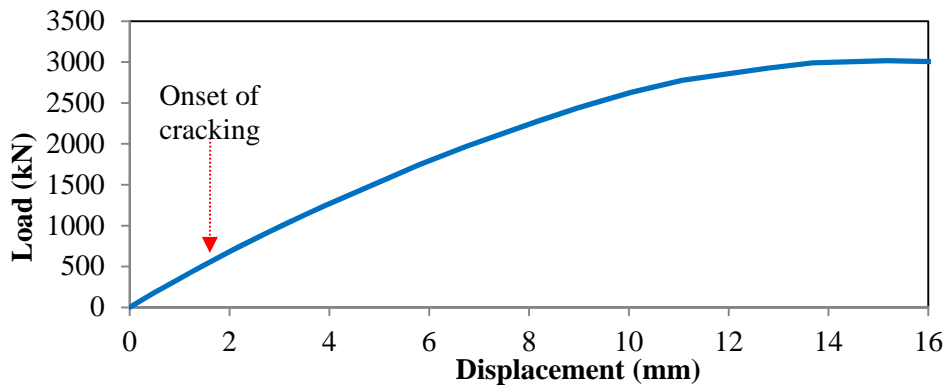


Fig. 3.52 Pushover curve (Load-Displacement relation).

### 3.2.5 Installed 10 cm diaphragm

Maximum principal stress distribution under self-weight and prestressing is shown in Fig. 3.53, and vertical deflection under self-weight and prestressing is shown in Fig. 3.54.

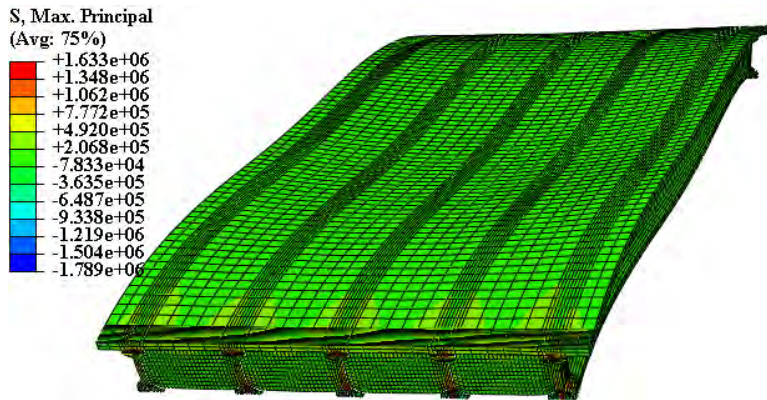


Fig. 3.53 Maximum principal stress distribution under self-weight and prestressing. ( $\times 10$ ).

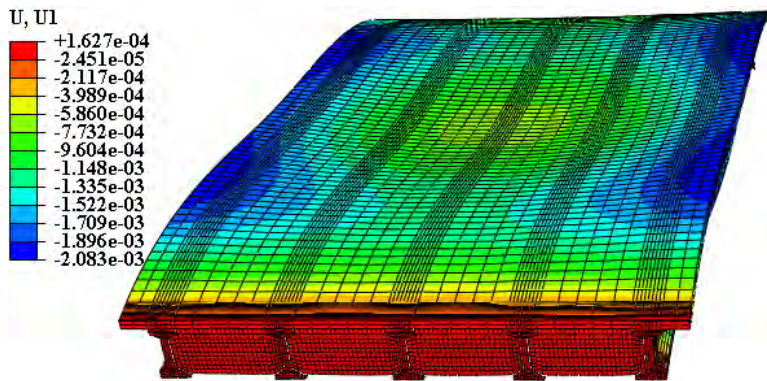
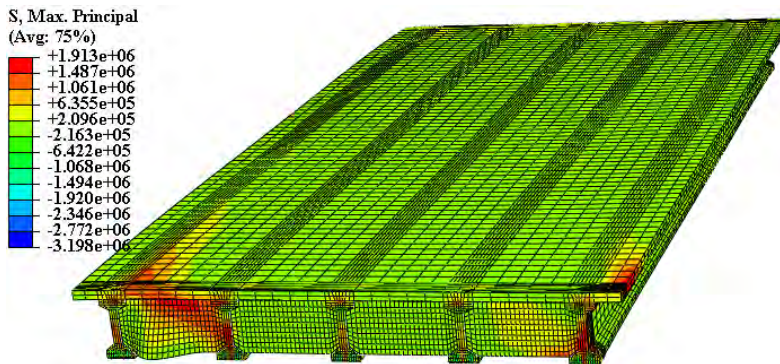
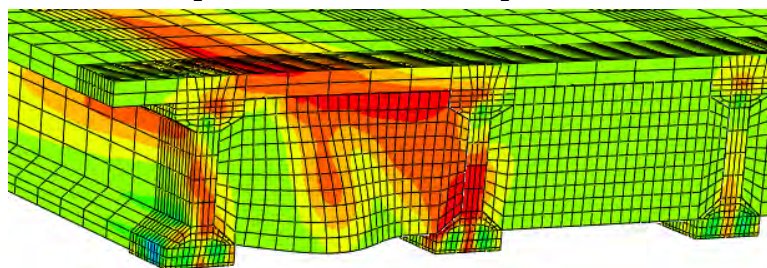


Fig. 3.54 Vertical deflection under self-weight and prestressing. ( $\times 500$ ).

Maximum principal stress distribution under self-weight, prestressing, and transverse force is shown in Fig. 3.55.



(a) Top view of the concrete superstructure.



(b) Zoom in the high stressed zone.

Fig. 3.55 Maximum principal stress under self-weight, prestress, and transverse force. ( $\times 10$ ).



Compared with the cases that the diaphragm thicknesses were 50 cm, 40 cm, 30 cm, and 20 cm, respectively, there was a critical difference. The structure with 10 cm diaphragm failed due to buckling of the diaphragm adjacent to the exterior girder ‘G1’. Subjected to combined compression and bending, the thin diaphragm lost stability and failed to support the girder. Hence, the damage was accelerated.

Vertical deflection and longitudinal displacement under self-weight, prestressing, and transverse force are shown in Figs. 3.56 and 3.57, respectively. One end diaphragm buckled and large displacement was demonstrated in Figs. 3.56 and 3.57. The buckling of the diaphragm is manifested in the two figures.

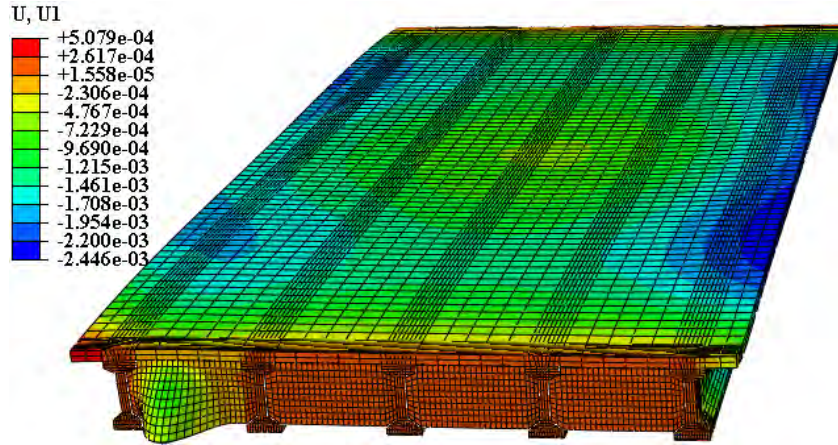


Fig. 3.56 Vertical deflection under self-weight, prestress, and transverse force. ( $\times 10$ ).

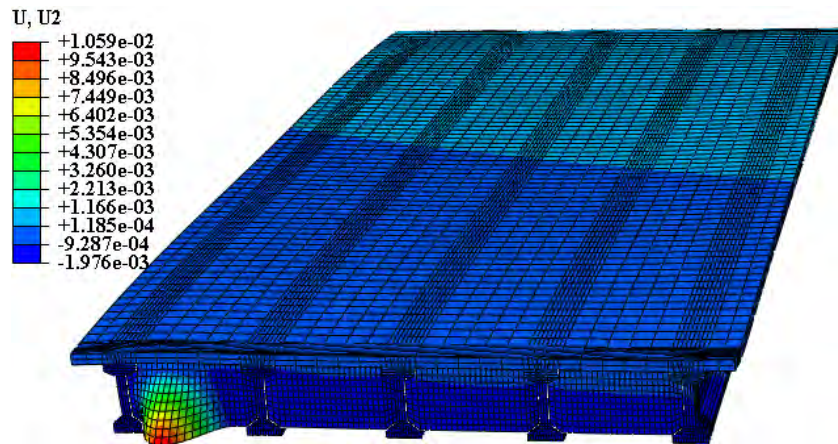
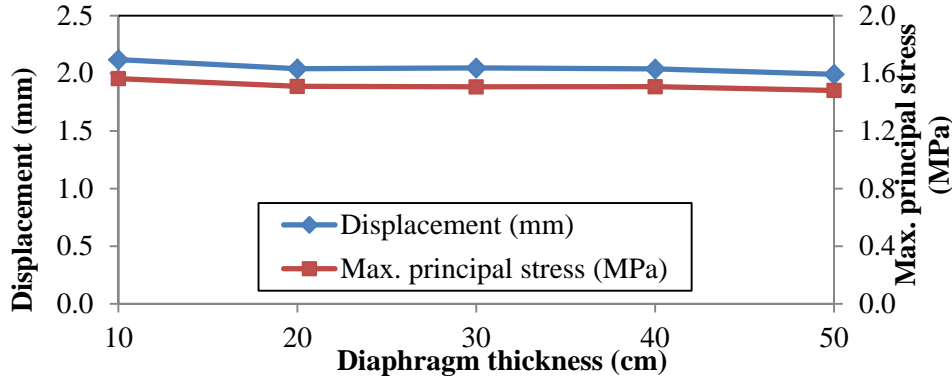


Fig. 3.57 Transverse drift under self-weight, prestressing, and transverse force. ( $\times 10$ ).

### 3.2.6 Discussion on diaphragm thickness

Bridges with different thicknesses of end diaphragms were investigated and thus the influence of diaphragm thickness is evaluated. The diaphragm thickness does not significantly influence the bridge’s behaviors under self-weight and prestressing, which are known as vertical behaviors, as demonstrated in Fig. 3.58. No significant change for the vertical deflection and maximum principal stress observed with the change of diaphragm thickness. When the diaphragm thickness varies from 10 cm to 50 cm, the changes of the vertical displacement and maximum principal stress are only up to 6%.

However, the comparison of the pushover curves corresponding to different diaphragm thicknesses in Fig. 3.59 demonstrates that the diaphragm thickness can significantly influence bridge’s transverse performance, including the failure mode, the transverse stiffness and capacity. ‘Transverse stiffness’ represents the slope of the linear portion of a pushover curve.



**Fig. 3.58 Influence of diaphragm thickness on vertical behaviors.**

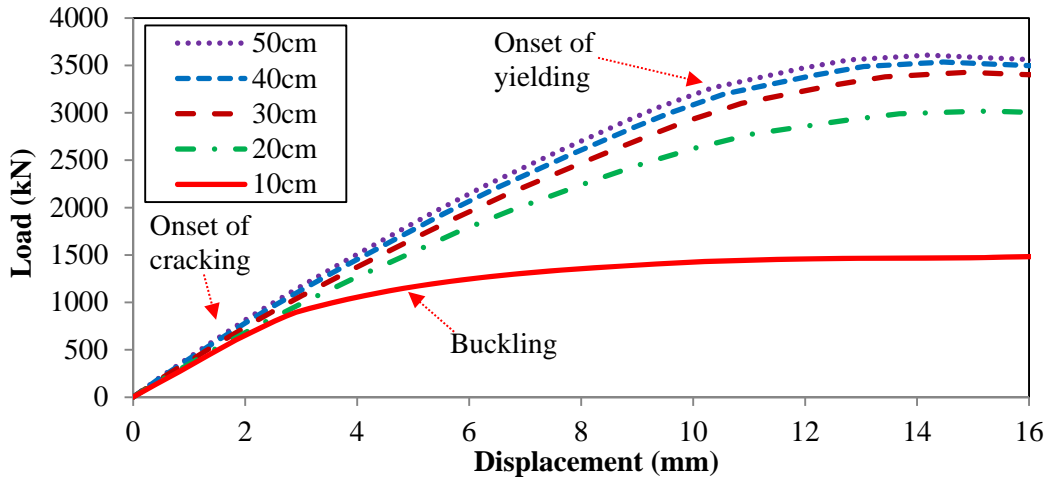


**Fig. 3.59 Comparison of pushover curves of bridges with different diaphragm thicknesses.**

The failure modes have been introduced in the preceding sections. At the very beginning of the loading, the materials were ideal elastic, so the displacement increased linearly with the load in the five curves. When damage initiated, the curve would be nonlinear. Eventually the structure would fail due to the fracture of concrete and yield of rebar. However, with the change of diaphragm thickness, the structures could be divided into two groups. The first group includes bridges with 20-50 cm diaphragms which did not buckle. The bridge with 10 cm diaphragm was separated from the first group because it buckled and thus the capacity was much lower than the structure in the first group.

The influence of diaphragm thickness on the transverse stiffness and capacity is manifested in Fig. 3.60. When the diaphragm thickness is varied from 10-50 cm, the stiffness linearly increases; however, the change of capacity is nonlinear. The curve can be divided into two parts by one data point that corresponds to 30 cm diaphragm. When the thickness is smaller than 30 cm, the capacity increases fast, and up to 133% capacity can be obtained by increasing the diaphragm thickness from 10-30 cm. However, after the 30 cm thickness point, the capacity will keep constant.

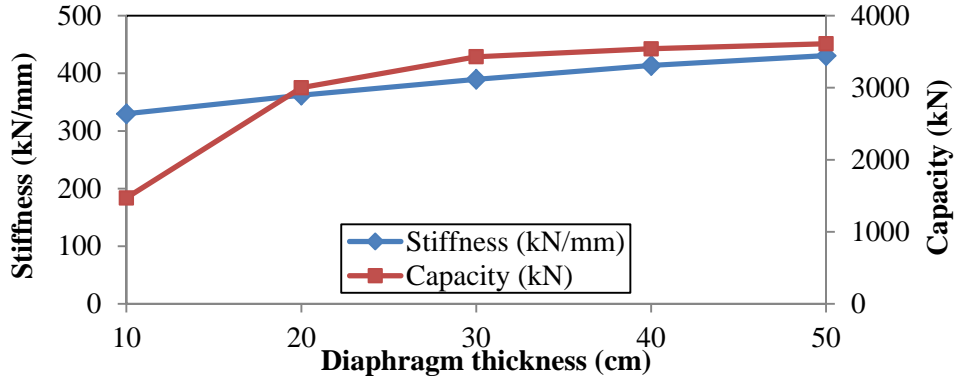


Fig. 3.60 Influence of diaphragm thickness on transverse behaviors.

### 3.3 Sensitivity Study for Friction Coefficient

In the analyses of the influences of diaphragm thickness and height, it was observed that each one of the girders helped resist transverse load due to the friction force from the surface-to-surface contact between cap and girder. Sensitivity study for the friction coefficient was carried out in this section. The FE models used in this section are similar to the one with half end diaphragms which has been demonstrated in Fig. 3.3; the only difference is the friction coefficient is changed.

#### 3.3.1 Friction coefficient 0.3

The friction coefficient of surface-to-surface contact between cap and girder was changed to be 0.3. Maximum principal stress and vertical deflection distributions of the bridge under self-weight and prestressing are shown in Figs. 3.61 and 3.62. Compared with the bridge with full end diaphragms, under self-weight and prestress, the bridge with partial end diaphragms demonstrated similar stress and displacement results in terms of the distribution and magnitude.

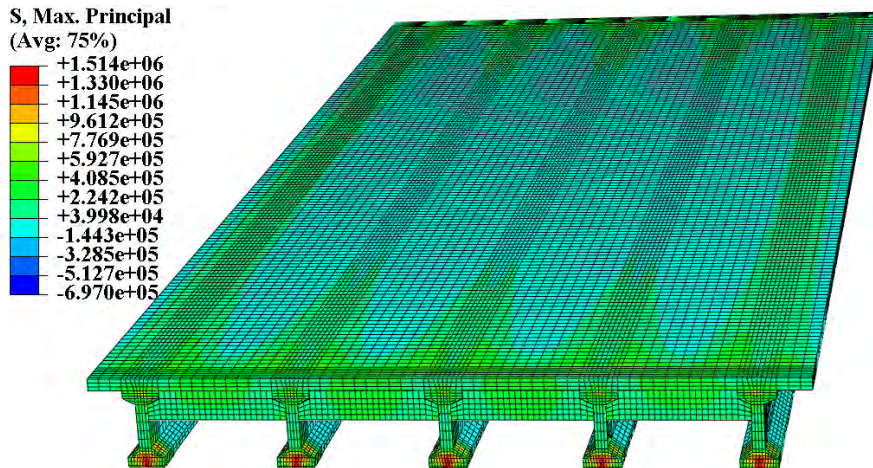
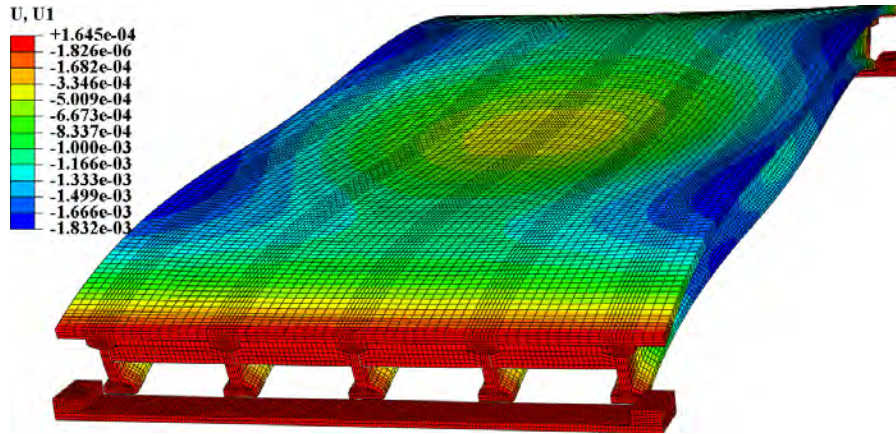
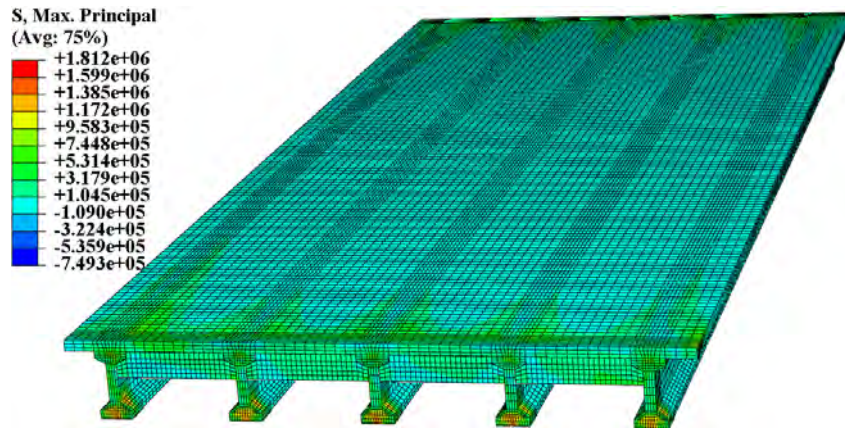


Fig. 3.61 Maximum principal stress under self-weight and prestressing.

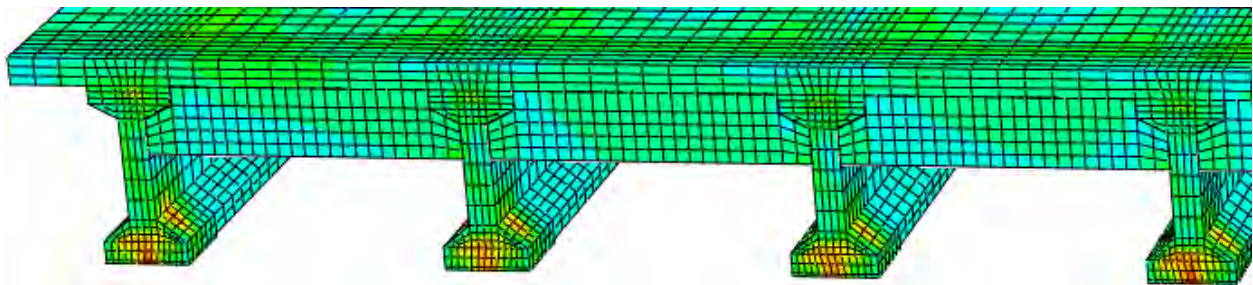


**Fig. 3.62 Vertical deflection under self-weight and prestressing. ( $\times 500$ ).**

Maximum principal stress distribution under self-weight, prestress, and transverse force is shown in Fig. 3.63. Cracking initiates at the top of the deck and the web of exterior girder simultaneously.



**(a) Top view of the superstructure.**



**(b) Zoom in the end diaphragm zone.**

**Fig. 3.63 Maximum principal stress under self-weight and prestressing.**

The pushover curve is shown in Fig. 3.64. After the contact between E1 and G1 is established, reaction force will be applied to G1.

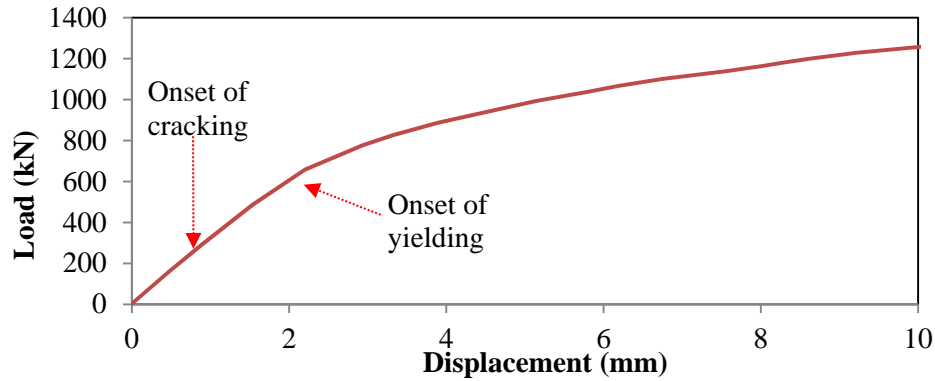


**Fig. 3.64 Pushover curve (Load-Displacement relation).**

The damage development is shown in Fig. 3.65. The damage propagates in the deck and the end diaphragm, and will potentially go through the interior girders; the cracks in girders propagate along the longitudinal direction. The damage behavior demonstrated is in good agreement with the damage observed in the San Nicholas bridge, as shown in Fig. 1.1.

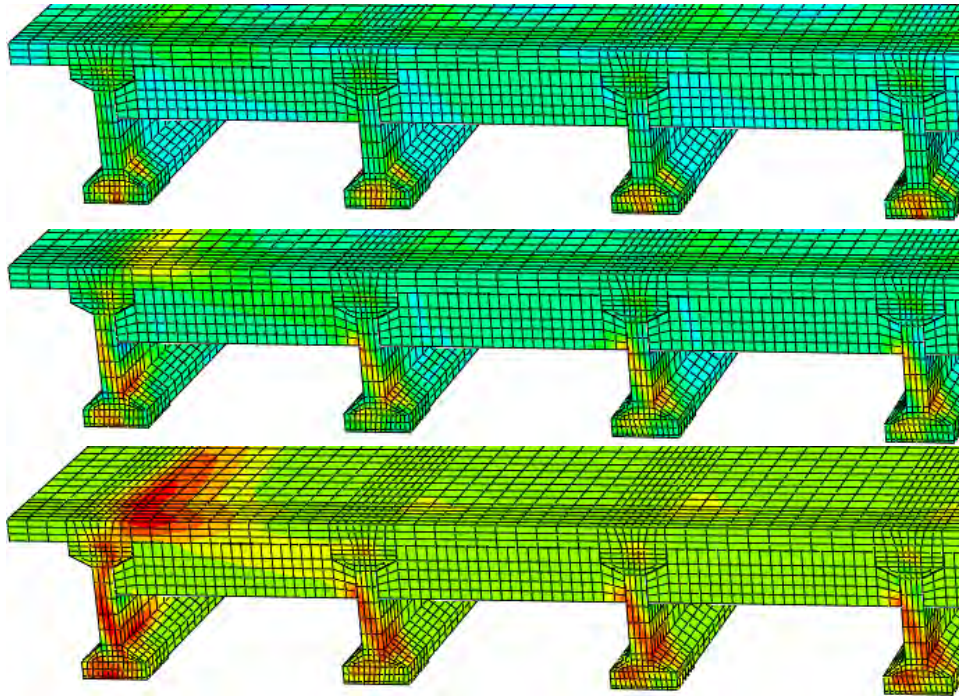


**Fig. 3.65 Damage development in the superstructure.**

Transverse displacement of the bridge under self-weight, prestressing, and transverse force is shown in Fig. 3.66. Overall the superstructure shifted in the transverse direction due to the transverse load, except for the end of G1 which was restrained by the exterior shear key. The end diaphragm was stiff in its plane; hence, the zones that were reinforced by the diaphragms were stiff and thus demonstrated relatively small displacement.

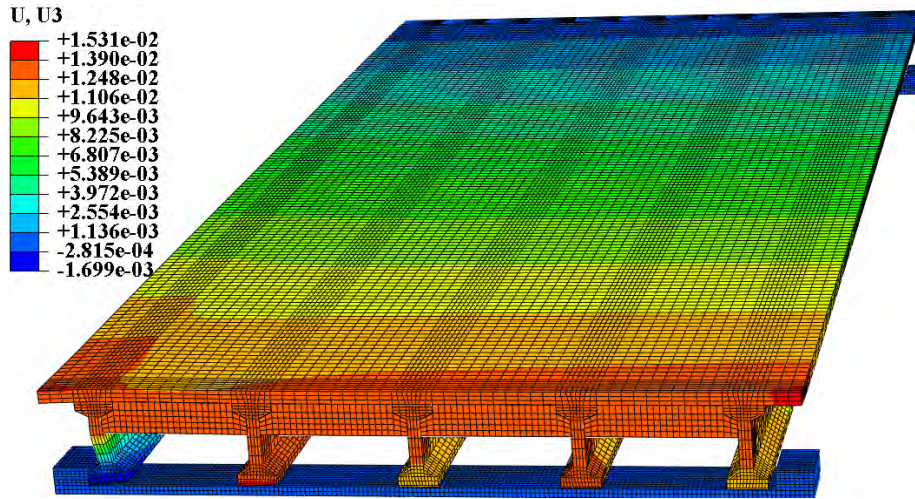


Fig. 3.66 Transverse drift under self-weight, prestressing, and transverse force. ( $\times 10$ ).

### 3.3.2 Friction coefficient 0.2

The friction coefficient of surface-to-surface contact between cap and girder was changed to be 0.2. Maximum principal stress and vertical deflection distributions of the bridge under self-weight and prestress are shown in Figs. 3.67 and 3.68. Compared with the bridge with full end diaphragms, under self-weight and prestress, the bridge with partial end diaphragms demonstrated similar stress and displacement results in terms of the distribution and magnitude.

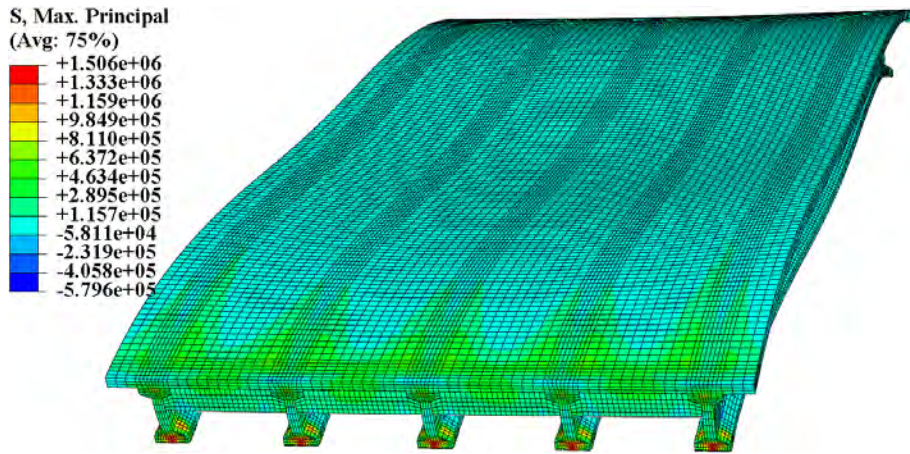
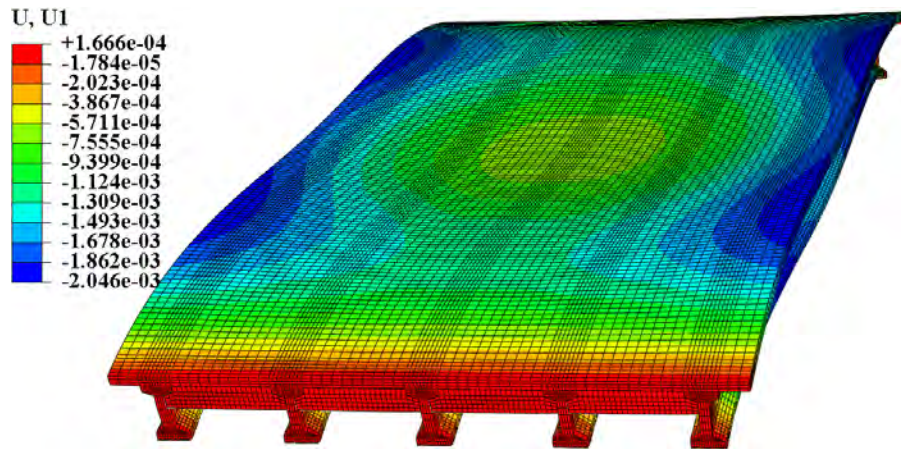
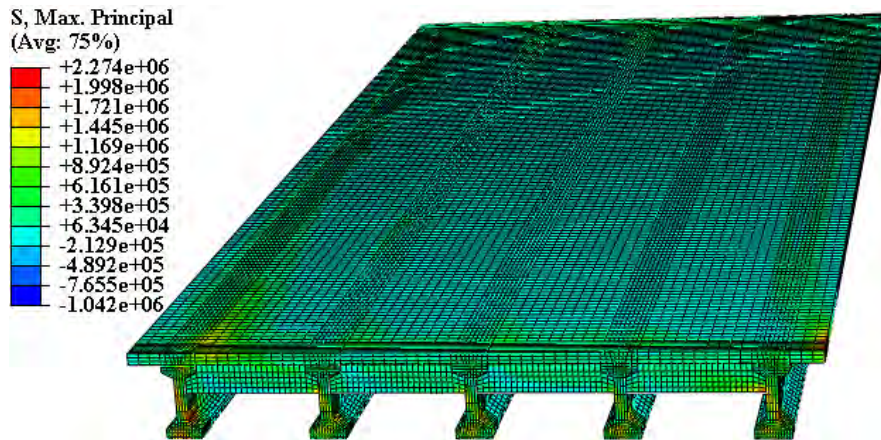


Fig. 3.67 Maximum principal stress under self-weight and prestressing. ( $\times 500$ ).

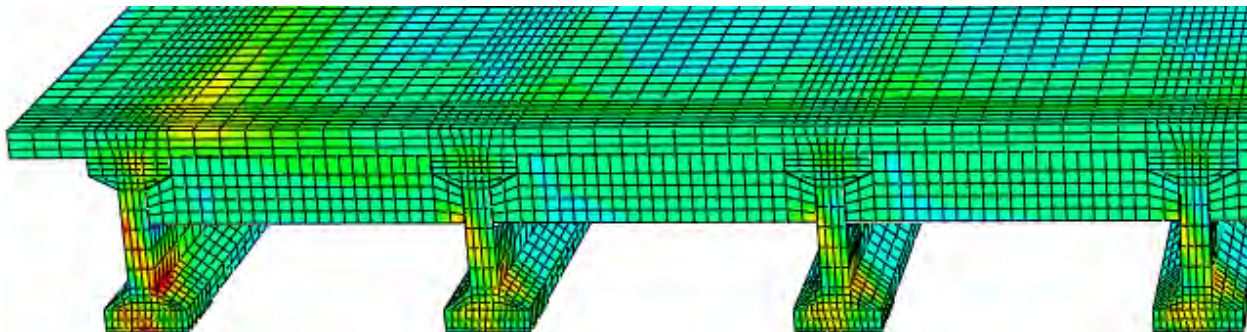


**Fig. 3.68 Vertical deflection under self-weight and prestressing. ( $\times 500$ ).**

Maximum principal stress distribution under self-weight, prestressing, and transverse force is shown in Fig. 3.69.



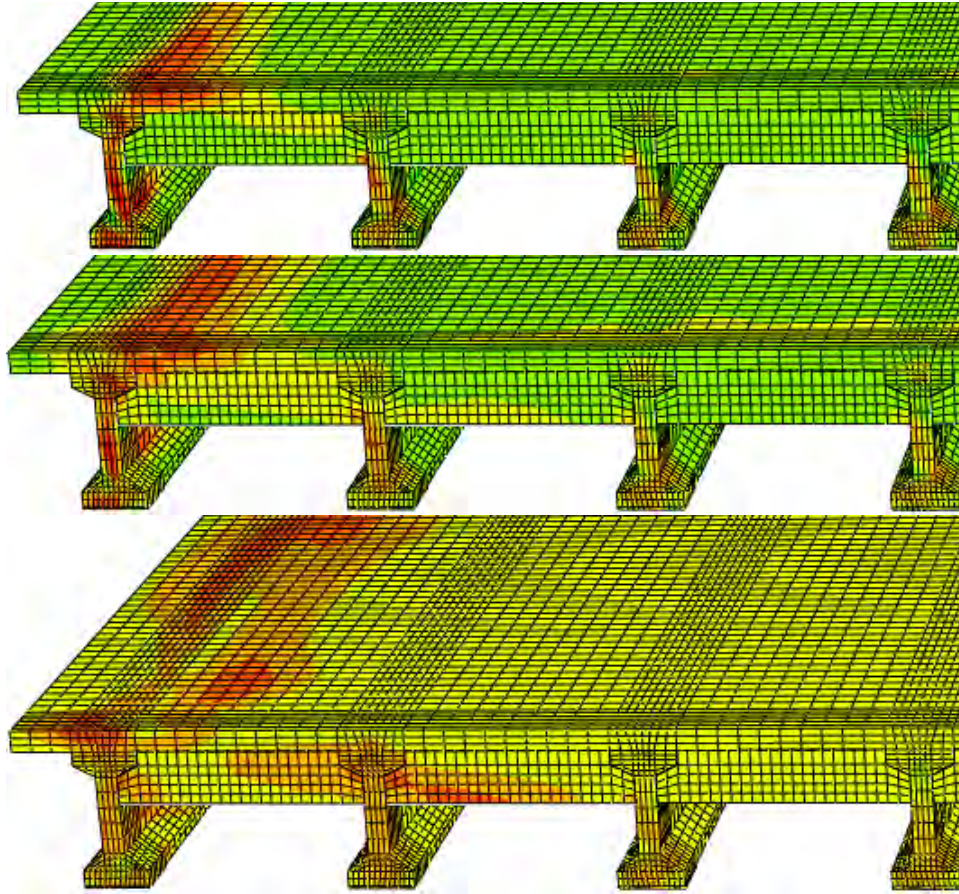
**(a) Top view of the superstructure.**



**(b) Zoom in the end diaphragm zone.**

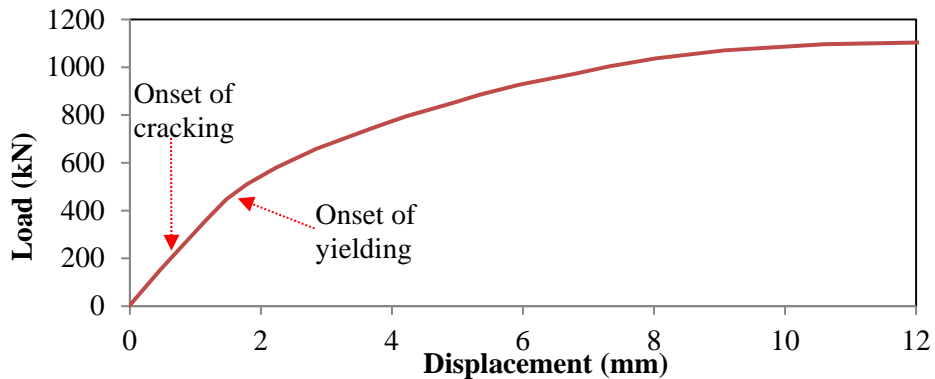
**Fig. 3.69 Maximum principal stress distribution under self-weight and prestressing.**

Fig. 3.69 shows that cracking initiates at the top of the deck and the web of exterior girder simultaneously. The damage development is shown in Fig. 3.70. The damage propagates in the deck and the end diaphragm, and will potentially go through the interior girders; the cracks in girders propagate along the longitudinal direction. The damage behavior demonstrated is in good agreement with the damage observed in the San Nicholas bridge shown in Fig. 1.1.



**Fig. 3.70 Damage development in the superstructure.**

The pushover curve is shown in Fig. 3.71.



**Fig. 3.71 Pushover curve (Load-Displacement relation).**

Transverse displacement of the bridge under self-weight, prestressing, and transverse force is shown in Fig. 3.72. Overall the whole superstructure shifted in the transverse direction due to the transverse load, except for the end of G1 which was restrained by the exterior shear key. The end diaphragm was stiff in its plane; hence, the zones that were reinforced by the diaphragms were stiff and thus demonstrated relatively small displacement.



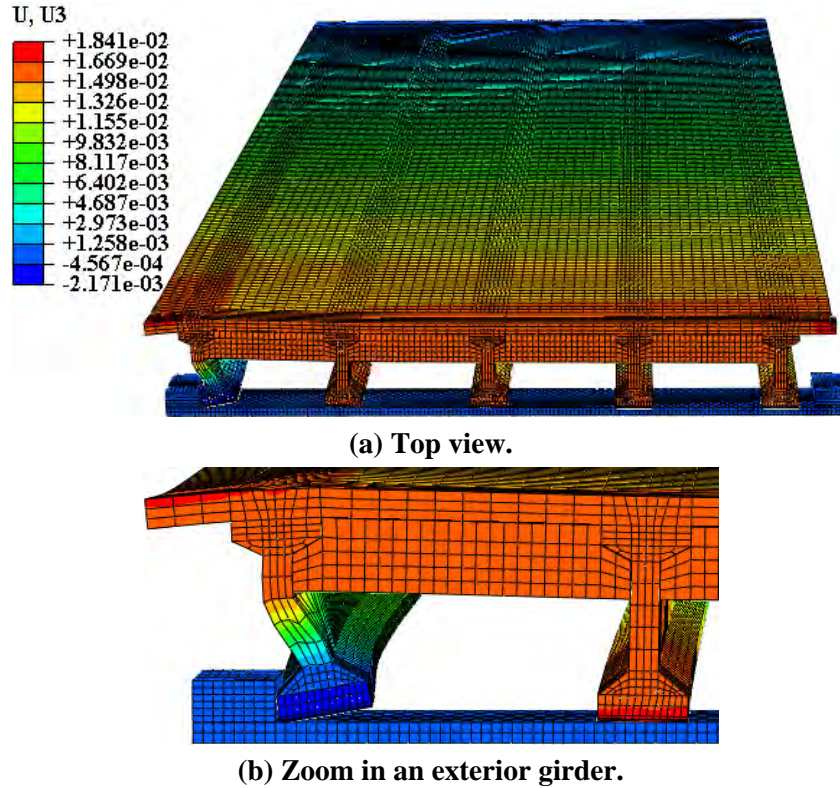


Fig. 3.72 Transverse drift under self-weight, prestressing, and transverse force. ( $\times 10$ ).

### 3.3.3 Friction coefficient 0.1

The friction coefficient of surface-to-surface contact between cap and girder was changed to be 0.1. Maximum principal stress and vertical deflection distributions of the bridge under self-weight and prestressing are shown in Figs. 3.73 and 3.74.

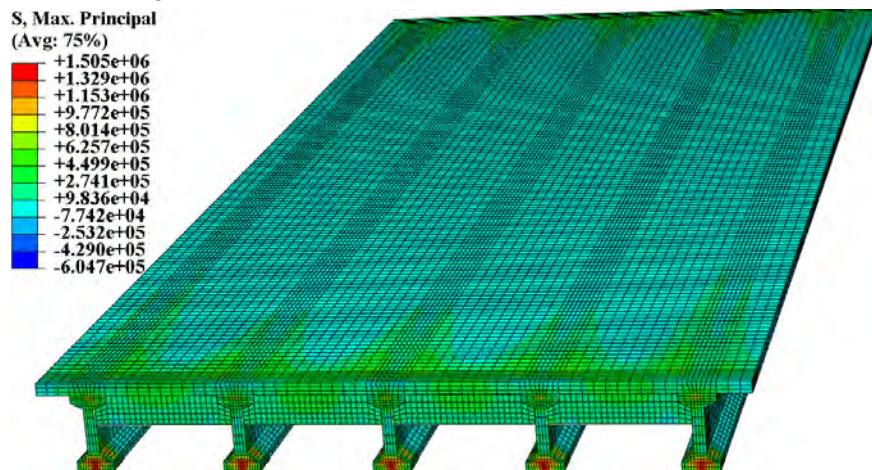


Fig. 3.73 Maximum principal stress distribution under self-weight and prestressing. ( $\times 500$ ).

Maximum principal stress distribution under self-weight, prestressing, and transverse force is shown in Fig. 3.75. Fig. 3.75 shows that cracking initiates at the top of the deck and the web of exterior girder simultaneously. The damage development is shown in Fig. 3.76.

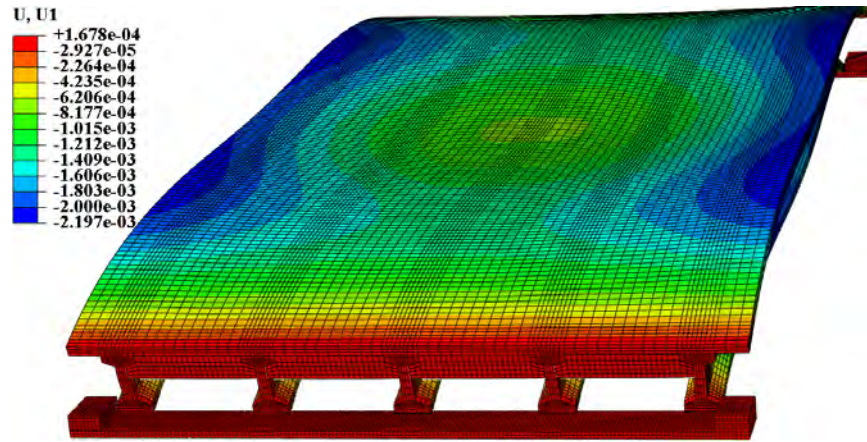


Fig. 3.74 Vertical deflection under self-weight and prestressing. ( $\times 500$ ).

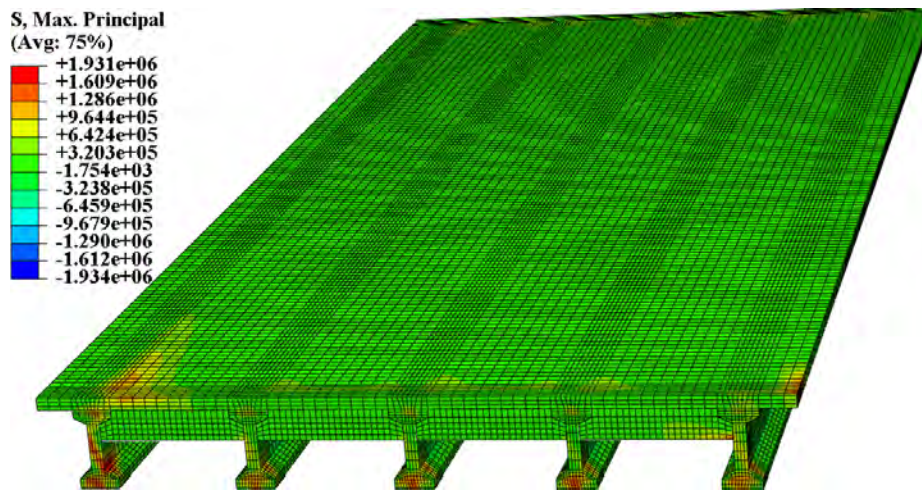
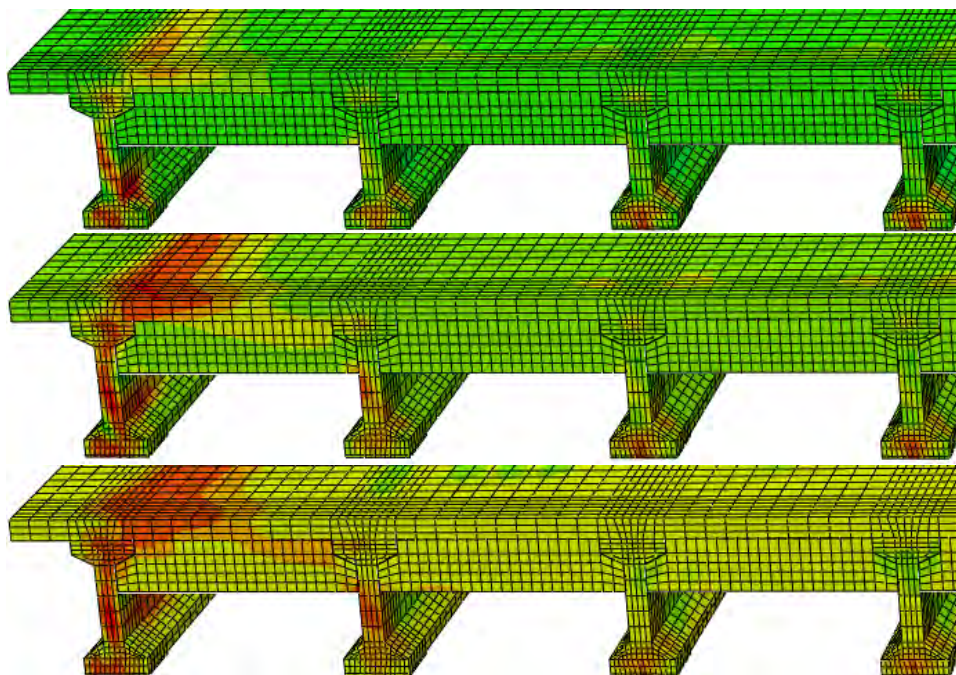
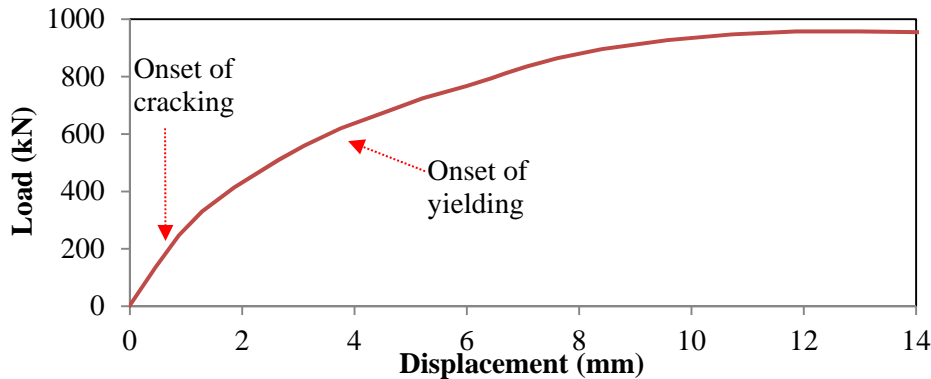


Fig. 3.75 Maximum principal stress under self-weight and prestressing.



**Fig. 3.76 Damage development in the superstructure.**

The pushover curve is shown in Fig. 3.77.



**Fig. 3.77 Pushover curve (Load-Displacement relation).**

The damage propagates in the deck and the end diaphragm, and will potentially go through the interior girders; the cracks in girders propagate along the longitudinal direction. The damage behavior demonstrated is in good agreement with the damage observed in the San Nicholas bridge shown in Fig. 1.1.

Transverse displacement of the bridge under self-weight, prestressing, and transverse force is shown in Fig. 3.78. Overall the whole superstructure shifted in the transverse direction due to the transverse load, except for the end of G1 which was restrained by the exterior shear key. The end diaphragm was stiff in its plane; hence, the zones that were reinforced by the diaphragms were stiff and thus demonstrated relatively small displacement.

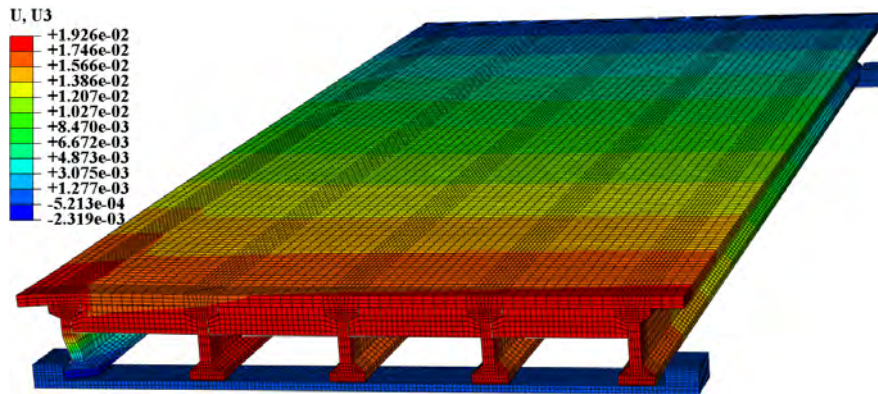


**Fig. 3.78 Transverse drift under self-weight, prestressing, and transverse force. ( $\times 10$ ).**

### 3.3.4 Frictionless

The friction coefficient of surface-to-surface contact between cap and girder was changed to be zero. Maximum principal stress and vertical deflection distributions of the bridge under self-weight and prestressing are shown in Figs. 3.79 and 3.80. Overall the stress was very small, because the stress due to selfweight was partially balanced by the prestress effect. However, localized stresses were caused by the prestressed tendons at the anchorage zones. The deflection distribution is overall symmetrical about the middle span in the longitudinal direction, and symmetrical about the G3 in the transverse direction. Compared with the bridge with full end diaphragms, under self-weight and prestress, the bridge with partial end diaphragms demonstrated similar stress and displacement results in terms of the distribution and magnitude.

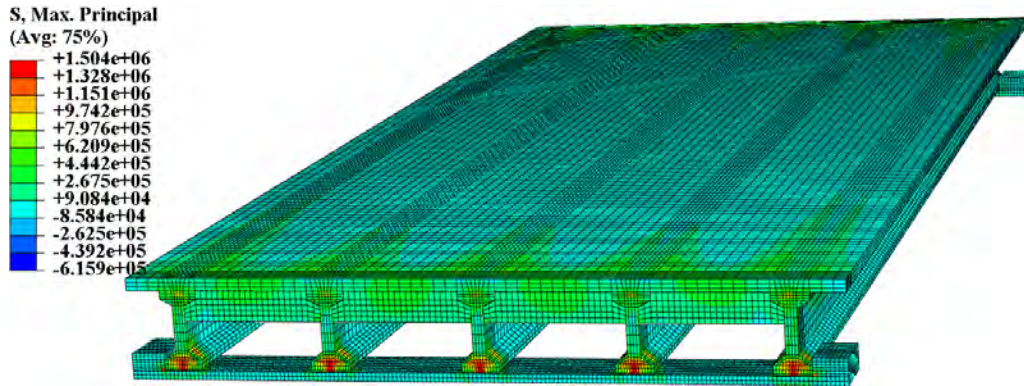


Fig. 3.79 Maximum principal stress under self-weight and prestressing.

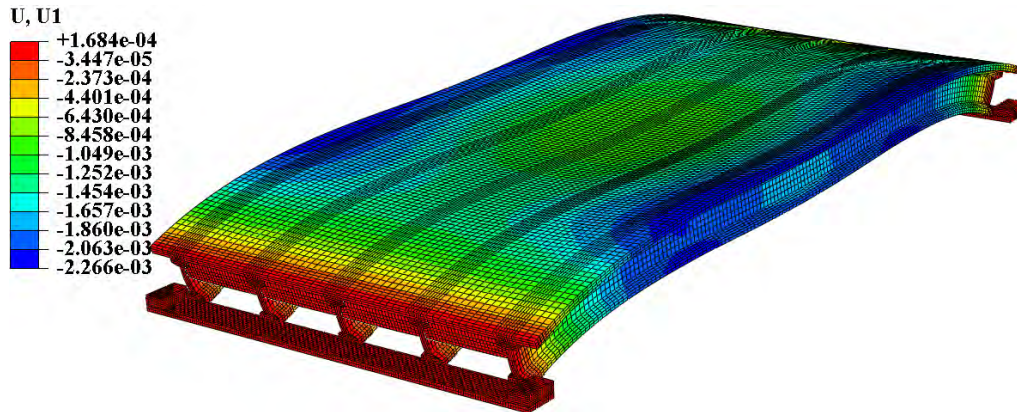


Fig. 3.80 Vertical deflection under self-weight and prestressing. ( $\times 500$ ).

Maximum principal stress distribution under self-weight, prestressing, and transverse force is shown in Fig. 3.81.

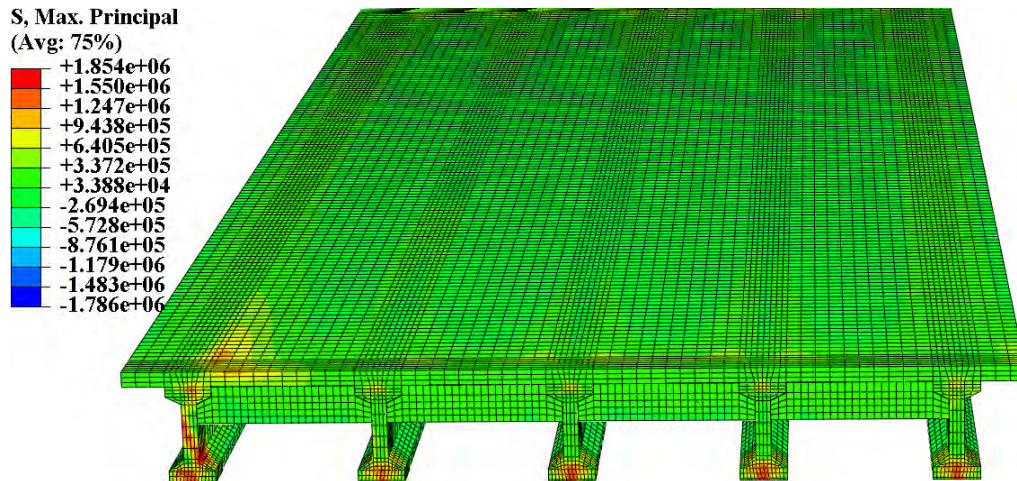
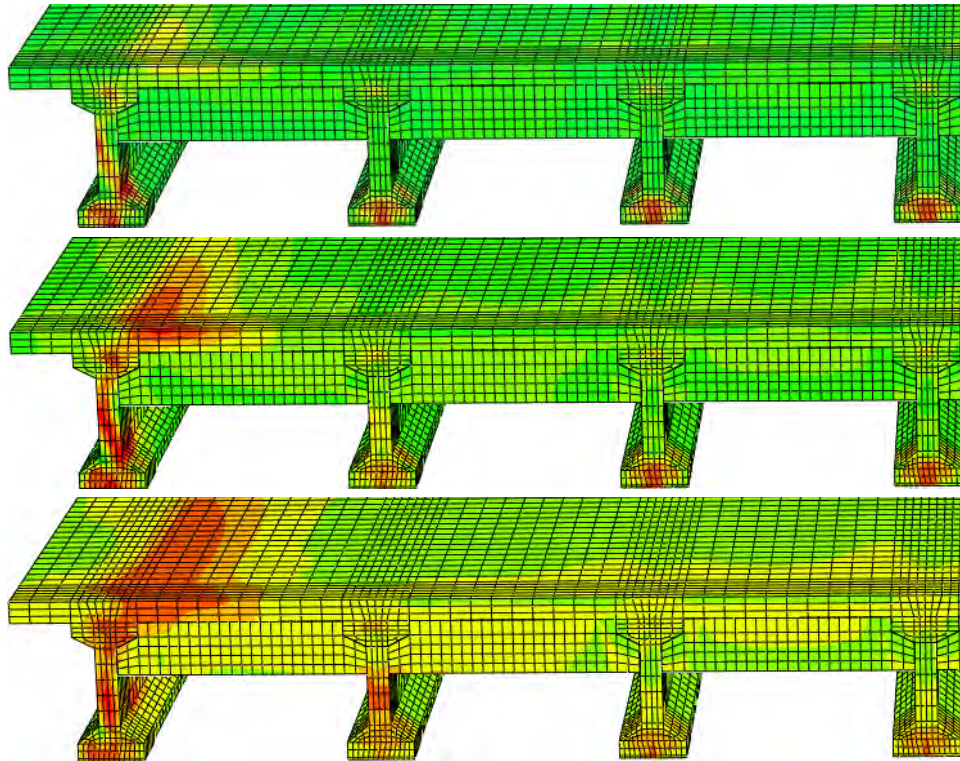
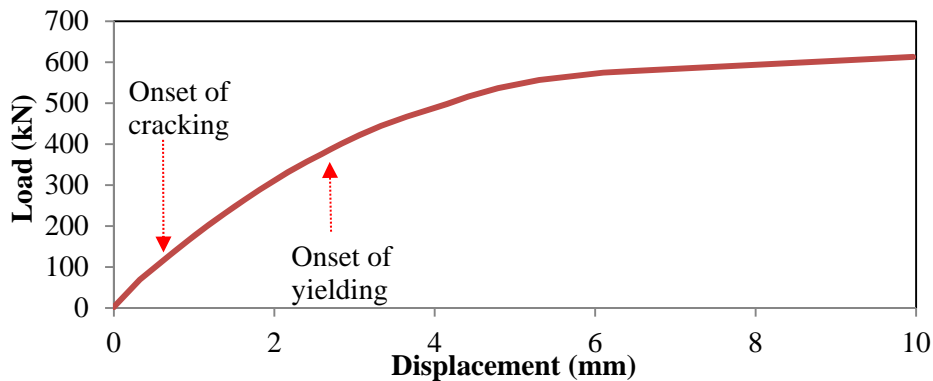


Fig. 3.81 Maximum principal stress under self-weight, prestressing and transverse load.



**Fig. 3.82 Maximum principal stress under self-weight, prestressing and transverse load.**

Fig. 3.81 shows that cracking initiates at the top of the deck and the web of exterior girder simultaneously. The damage development is shown in Fig. 3.82. The damage propagates in the deck and the end diaphragm, and will potentially go through the interior girders; the cracks in girders propagate along the longitudinal direction.



**Fig. 3.83 Pushover curve (Load-Displacement relation).**

The pushover curve is shown in Fig. 3.3.23. After the contact between E1 and G1 is established, reaction force will be applied to G1. With the increase of loading, maximum principal stress/strain in concrete will increase until crack is formed. Onset of crack corresponds to 2 mm transverse displacement. Then the structure will undergo a ‘softening’ stage representing the propagation of cracks in the concrete; however, the structure can resist higher load during that stage, because the concrete is reinforced by rebar that can provide tensile strength and restrain the cracking. With the propagation and widening of the cracks, eventually the rebar will yield and thus the structure will lose strength and fail.

### 3.3.5 Discussion on friction coefficient

The influence of friction coefficient can be evaluated based on the investigations in Sections 3.3.1-3.3.4.

The friction coefficient does not significantly influence the bridge's behaviors under self-weight and prestressing, which are known as vertical behaviors, as shown in Fig. 3.84. No significant change for the vertical deflection and maximum principal stress observed with the change of friction coefficient.

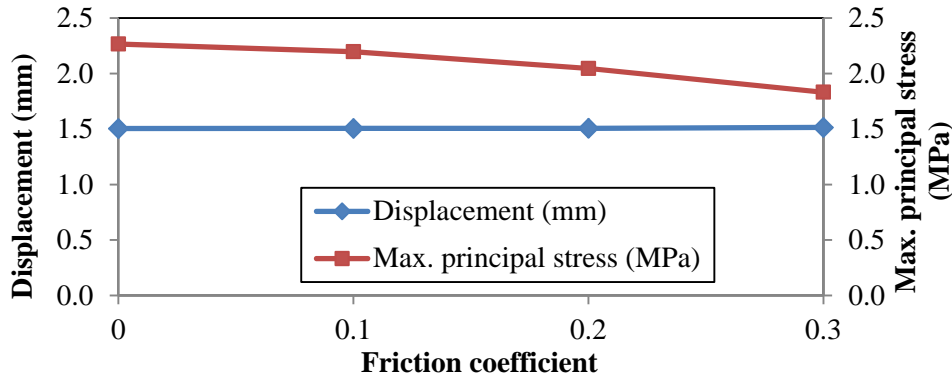


**Fig. 3.84 Influence of friction coefficient under self-weight and prestressing.**

The load-displacement relations of the bridges with different end diaphragms under self-weight, prestressing and transverse load are compared in Fig. 3.85 that demonstrates the friction coefficient can significantly influence bridge's transverse performance, including the failure mode, the transverse stiffness and capacity.

The failure modes have been introduced in the preceding sections. At the very beginning of the loading, the materials were ideal elastic, so the displacement increased linearly with the load in the five curves. When damage initiated, the curve would be nonlinear. Eventually the structure would fail due to the fracture of concrete and yield of rebar.

When the superstructure was supported on smooth caps by defining the friction coefficient to be zero, the movement of the superstructure would be solely constrained by exterior shear keys. Hence, in the transverse direction, the superstructure would only be subjected to the transverse load and the reaction force provided by the exterior shear key. The reaction force was all applied on the exterior girder where damage initiated and then propagated. When the deck and diaphragms are relatively thin, damage can possibly initiate and then propagate in the deck and diaphragm. This explains why the exterior girders are usually damaged earlier than the interior girders instead of being damaged simultaneously. The strength of interior girders was not fully utilized. Therefore, potentially the strength to resist transverse load can be further increased by making full use of the interior girders.

When the friction coefficient is nonzero, all girders will be directly subjected to friction force in the transverse direction, so damage can potentially initiate in the multiple girder simultaneously. In this way, all girders directly help resist the transverse load, and thus the transverse stiffness and capacity can be increased, as shown in Fig. 3.85. It is manifested that up to 100% capacity and 60% stiffness can be gained by increasing the friction coefficient from 0 to 0.3.

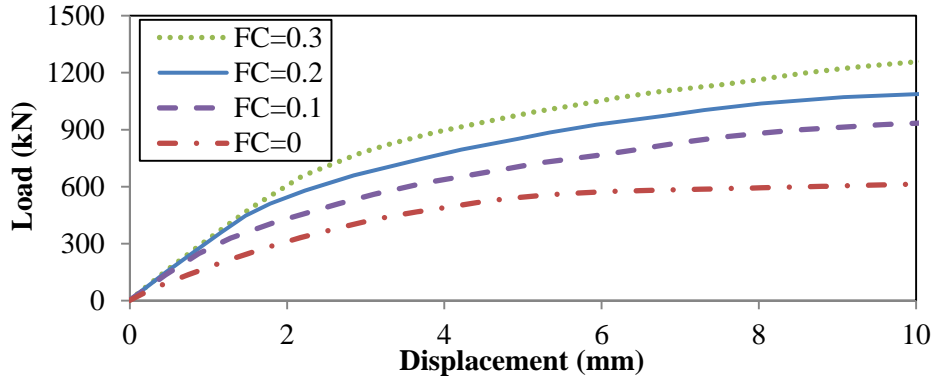


**Fig. 3.85 Comparison of pushover curves of bridges with different friction coefficients.**

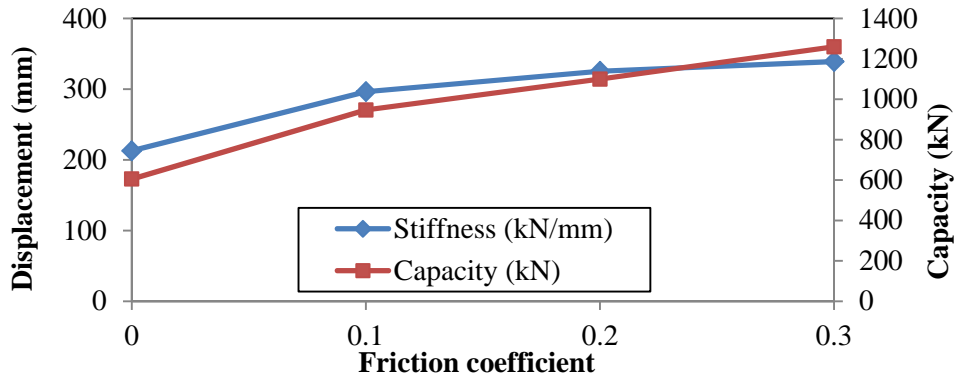


**Fig. 3.86 Influence of friction coefficient under self-weight, prestressing and transverse load.**

However, unfortunately during a real earthquake, the friction cannot always benefit the bridge. Typically a real world earthquake consists of both transverse and vertical ground motion components. The normal contact force varies during the earthquake; with a constant friction coefficient, the friction force will vary with the normal contact force. This phenomenon can also be considered in another way that is to keep the normal contact force constant by adjusting the friction coefficient. Downward inertia forces can be equivalent to an increase of friction coefficient; upward inertia forces can be equivalent to a decrease of friction coefficient. When the superstructure is subjected to a downward inertia force, the friction will be increased, so the structure will be able to resist more transverse inertia force, which benefits the structure. However, when the superstructure is subjected to an upward inertia force, the friction will be decreased, so the structure's capacity will be reduced, which may lead to damage.

### 3.4 Summary

In this section, bridges with different end diaphragms and support conditions were investigated. The influences of end diaphragm thickness and height, and the friction coefficient were evaluated in terms of the failure mode and capacity under self-weight, prestressing, and transverse load.

The bridge's behaviors under self-weight and prestressing were not significantly influenced by the end diaphragm and the friction coefficient of the supports. Within the investigation scope, less than 10% change was observed. However, the bridge's transverse behaviors are significantly influenced by end diaphragm and the friction coefficient of the supports.

For bridges with partial diaphragms, damage usually initiates near the joint of the exterior girder and the end diaphragm, which was in good agreement of the observations of damage in real world bridge. When the diaphragm thickness is varied from 10 cm to 50 cm, the stiffness linearly increases; however, the change of capacity is nonlinear. The curve can be divided into two parts by one data point that

corresponds to 75% diaphragm height. When the thickness is smaller than 30 cm, the capacity increased linearly. However, from 75% to 100% of diaphragm height, the capacity was increased by 160%. And when the diaphragm height was varied from 0 to 100%, the capacity was increased by 360%.

For bridges with full end diaphragms, damage can initiate at the joint of deck and end diaphragm or the joint of exterior girder and end diaphragm. When the diaphragm thickness was varied from 50 cm to 20 cm, the failure mode was fracture of concrete and yield of rebar; buckling of diaphragm was not observed. However, buckling of end diaphragm was observed when the diaphragm thickness was 10 cm, and transverse capacity was significantly reduced. When the diaphragm thickness is varied from 10 cm to 50 cm, the stiffness linearly increases; however, the change of capacity is nonlinear. The curve can be divided into two parts by one data point that corresponds to 30 cm diaphragm. When the thickness is smaller than 30 cm, the capacity increases fast, and up to 133% capacity can be obtained by increasing the diaphragm thickness from 10 cm to 30 cm. However, after the 30 cm thickness point, the capacity will keep constant.

When the friction coefficient is zero, representing smooth surfaces, transverse forces that the superstructure is subjected to will only consist of the transverse load and the reaction force provided by the exterior shear key. The reaction force is all applied on the exterior girder. In this case, damage will initiate and then propagate in the exterior girder; when the deck and diaphragms are relatively thin, damage can possibly initiate and then propagate in the deck and diaphragm. However, when the friction coefficient is not zero, all girders will be directly subjected to friction force in the transverse direction, so damage can potentially initiate in the multiple girder simultaneously. In this way, all girders directly help resist the transverse load, and thus the transverse stiffness and capacity can be increased. It is manifested that up to 100% capacity and 60% stiffness can be gained by increasing the friction coefficient from 0 to 0.3.



## SECTION 4 ANALYSIS OF BRIDGES WITHOUT END DIAPHRAGM

In this section, the performance of bridge superstructures without end diaphragm is investigated. The functions and effectiveness of interior shear keys and friction coefficient of support are evaluated in terms of the failure mode, transverse stiffness and capacity of the bridges.

### 4.1 Analysis of Bridge without Interior Shear Keys

Structural behaviors of the two types of bridge were compared by finite element analysis. Fig. 4.1 shows the cross sections of the two types of bridge.

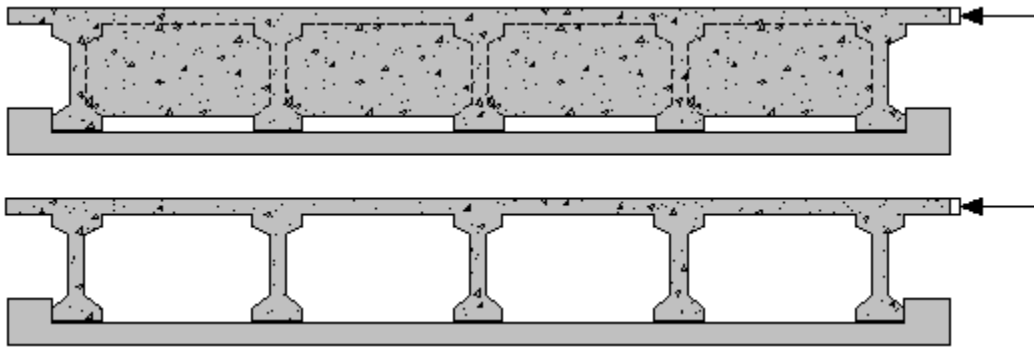


**Fig. 4.1 Comparison of the cross sections.**

The FE model of the bridge without end diaphragm is shown in Fig. 4.2. Maximum principal stress and vertical deflection distributions of the bridge under self-weight and prestressing are shown in Figs. 4.3 and 4.4, respectively. Overall the stress was very small, because the stress due to selfweight was partially balanced by the prestress effect. However, localized stresses were caused by the prestressed tendons at the anchorage zones. The deflection distribution is overall symmetrical about the middle span in the longitudinal direction, and symmetrical about the G3 in the transverse direction.

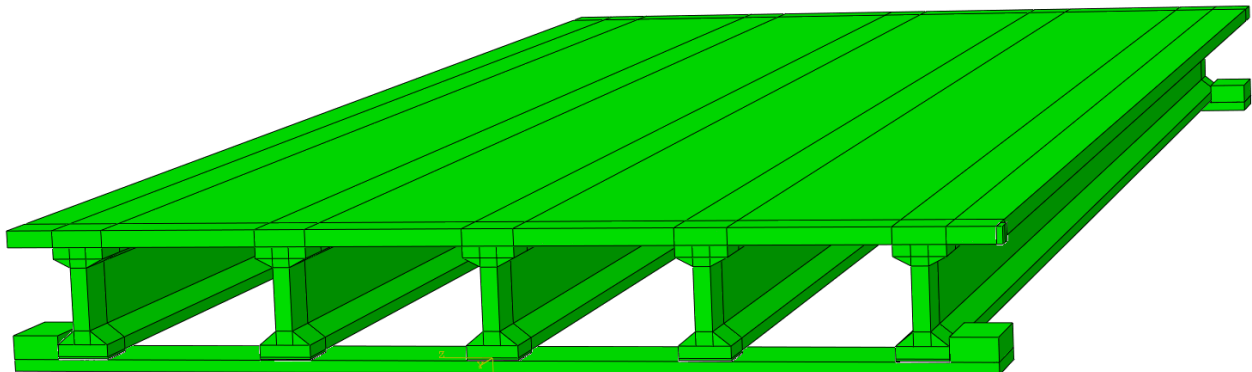


**Fig. 4.2 A simplified FE model of bridge without diaphragm.**

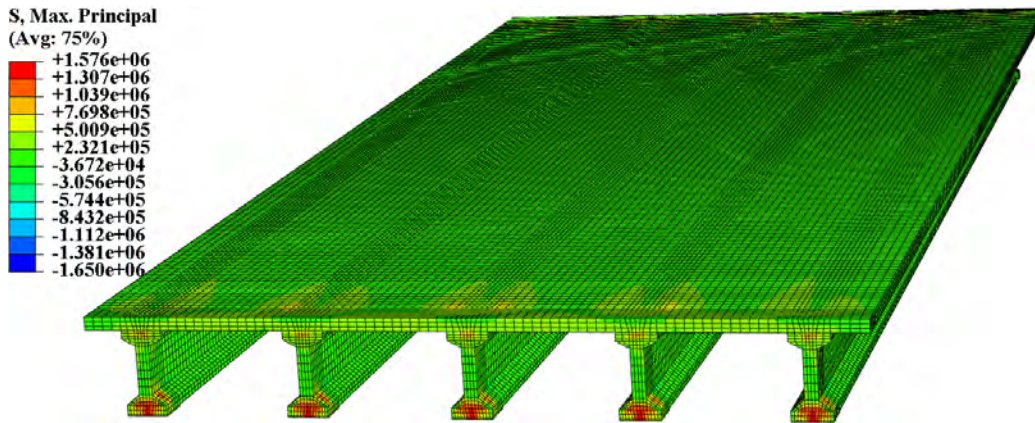


Fig. 4.3 Maximum principal stress distribution under self-weight and prestressing.

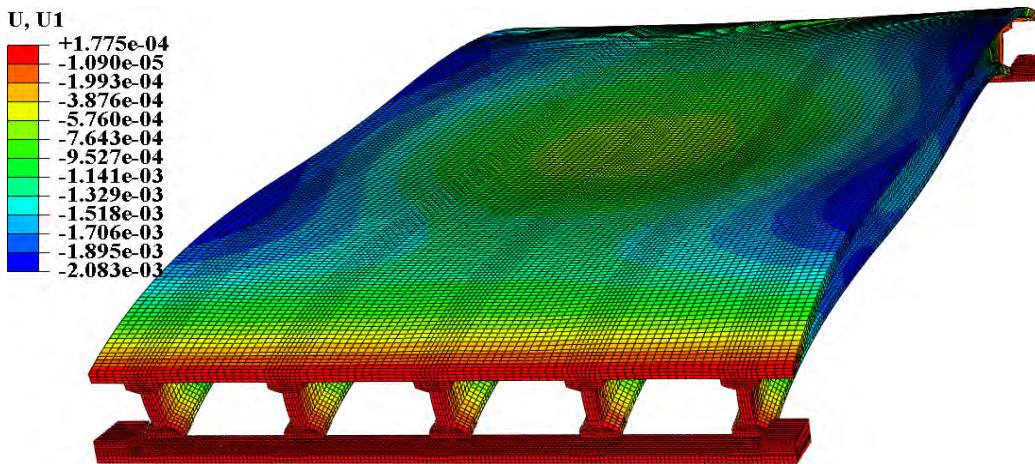


Fig. 4.4 Vertical displacement distribution under self-weight and prestressing. ( $\times 500$ ).

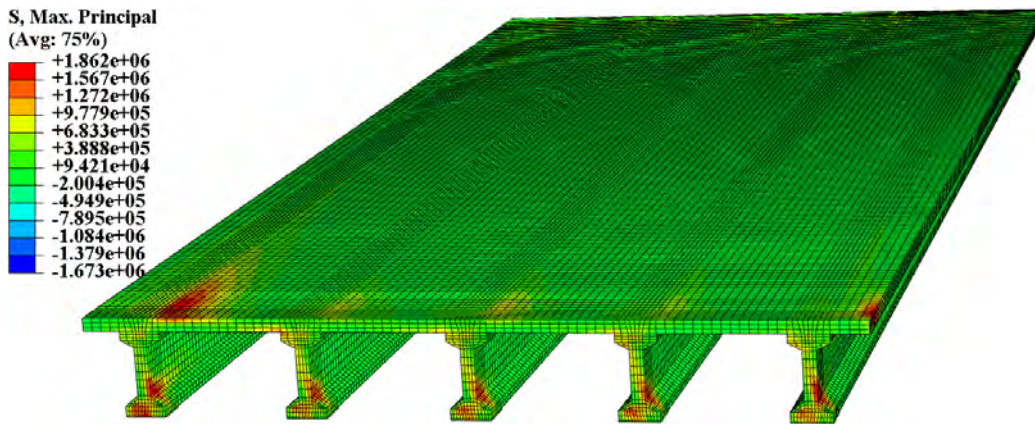
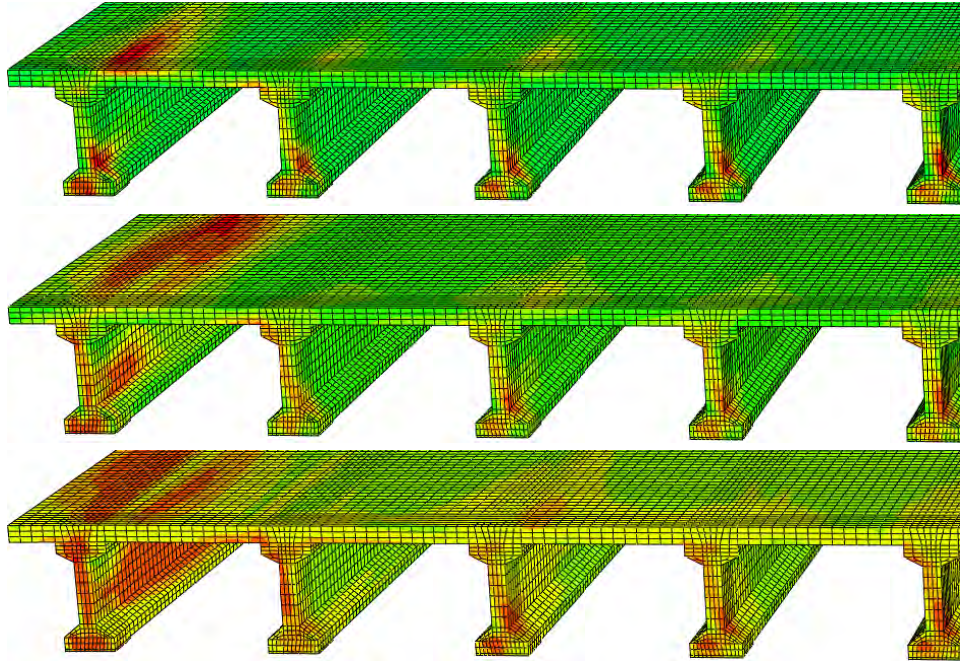


Fig. 4.5 Maximum principal stress distribution.

Fig. 4.5 shows the maximum principal stress distribution under self-weight, prestressing, and transverse force, which indicates that the cracking initiates at the top of the deck and the web of exterior and the adjacent interior girders, simultaneously. Fig. 4.6 shows the progressive damage development in concrete, where the damage propagates in the deck and the end diaphragm. The failure mode is in good agreement with the observations of a real world bridge, Chada Bridge, which is shown in Fig. 4.7.<sup>4,5</sup>



**Fig. 4.6** Damage development in the bridge superstructure.



**Fig. 4.7** Damage in Chada Bridge with no diaphragm.

Transverse displacement of the bridge under self-weight, prestressing, and transverse force is shown in Fig. 4.8.

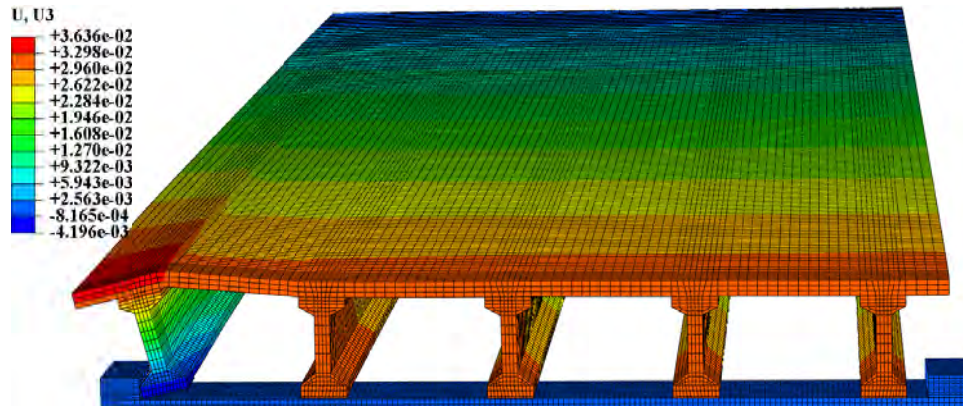


**Fig. 4.8** Transverse drift. ( $\times 10$ ).

The pushover curve is shown in Fig. 4.9.

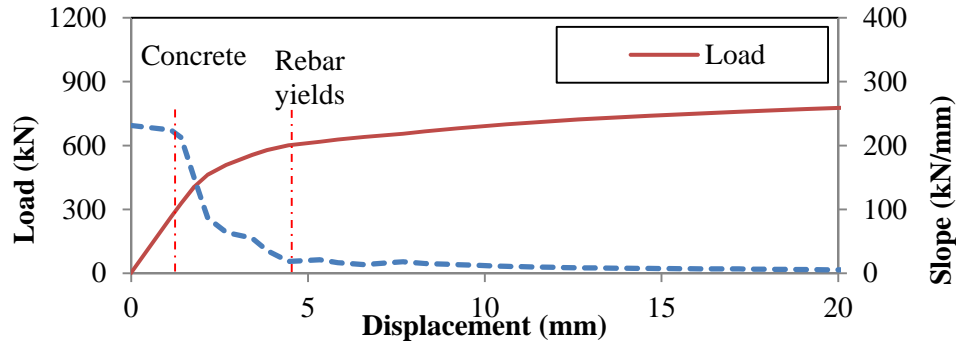


Fig. 4.9 Pushover curve (Load-Displacement relation).

## 4.2 Parametric Study of Friction Coefficient

### 4.2.1 Friction coefficient 0.3

The friction coefficient of the FE model shown in Fig. 4.2 was changed from 0.2 to 0.3. Maximum principal stress and vertical deflection distributions of the bridge under self-weight and prestressing are shown in Figs. 4.10 and 4.11, respectively.

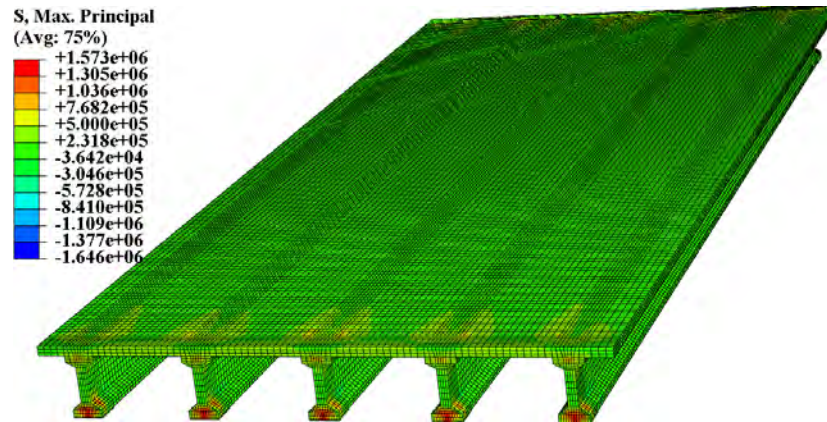


Fig. 4.10 Maximum principal stress distribution under self-weight and prestressing.

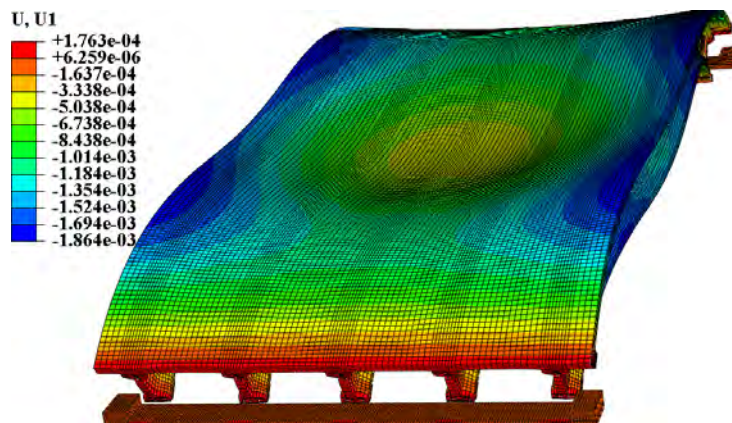


Fig. 4.11 Vertical deflection under self-weight and prestressing. ( $\times 500$ ).

Maximum principal stress distribution under self-weight, prestressing, and transverse force is shown in Fig. 4.12 that shows the cracking initiates at the top of the deck and the web of exterior, simultaneously.

The damage development is shown in Fig. 4.13 where the damage propagates in the deck and the end diaphragm; the cracks in girders propagate along the longitudinal direction.

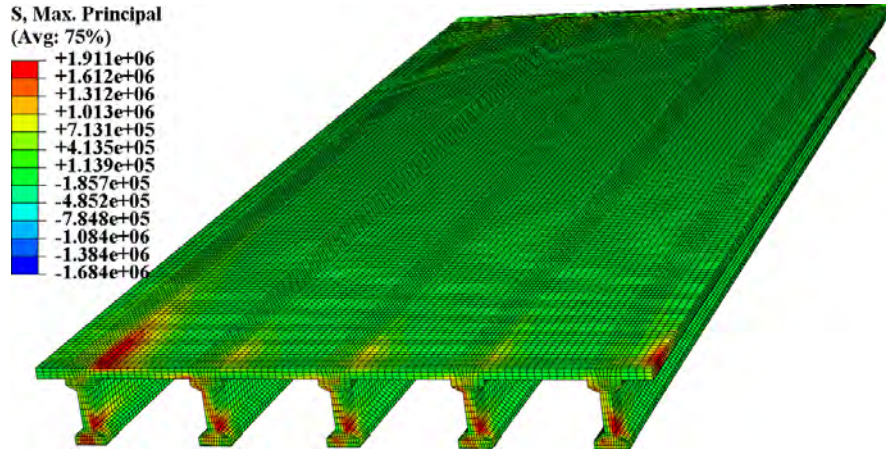


Fig. 4.12 Maximum principal stress.

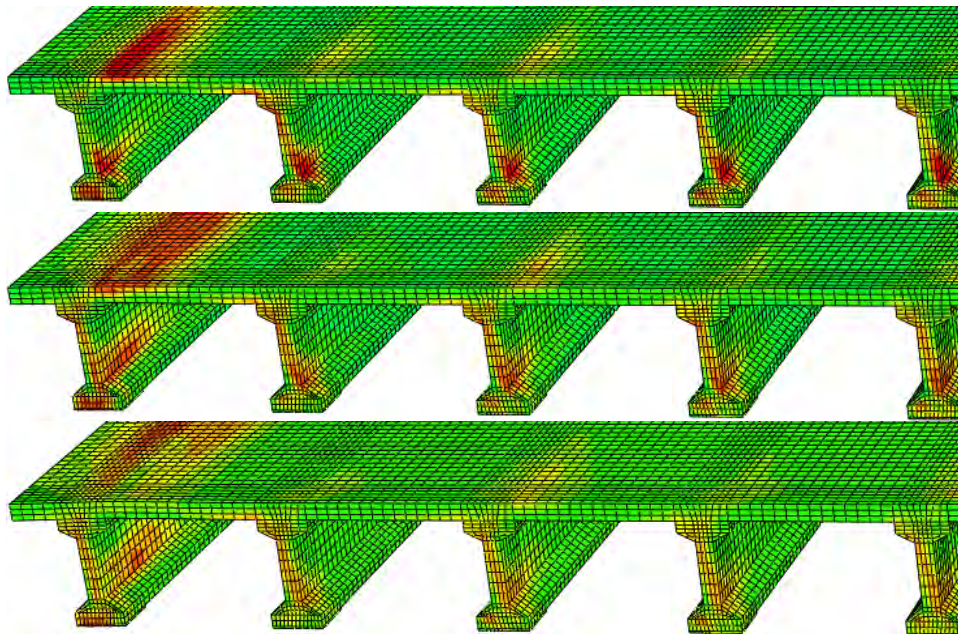


Fig. 4.13 Damage development in the superstructure.

The pushover curve is shown in Fig. 4.14. After the contact between E1 and G1 is established, reaction force will be applied to G1.

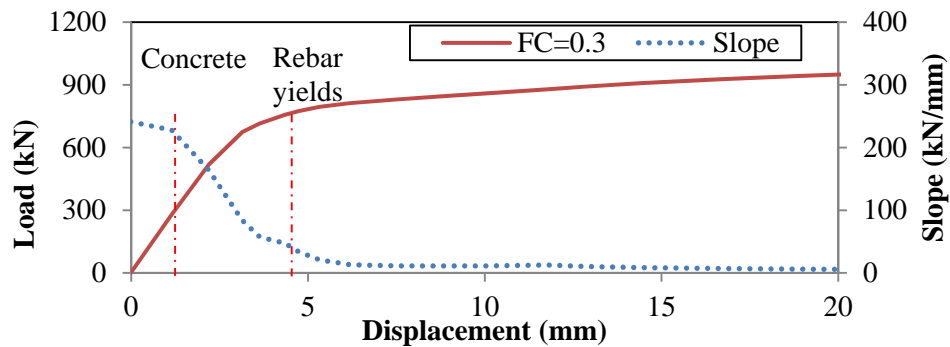


Fig. 4.14 Pushover curve (Load-Displacement relation).

Transverse displacement of the bridge under self-weight, prestress, and transverse force is shown in Fig. 4.15. Overall the superstructure shifted in the transverse direction due to the transverse load, except for G1 and G2 which were restrained by E1.

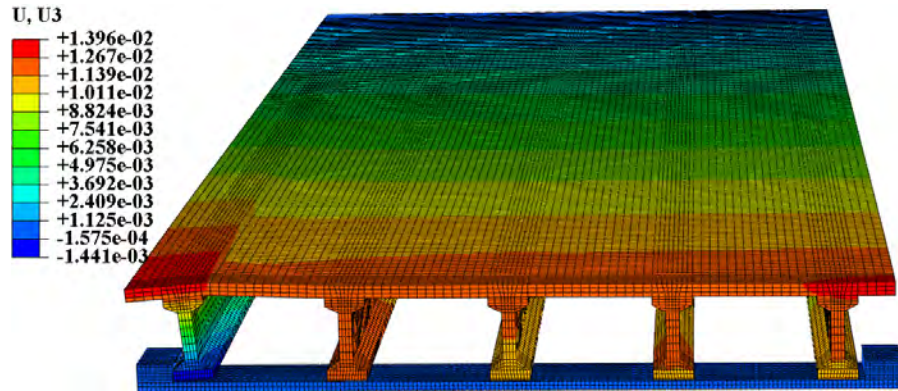


Fig. 4.15 Transverse drift. ( $\times 10$ ).

#### 4.2.2 Friction coefficient 0.2

The FE model and the simulation results have been introduced in Section 4.1.

#### 4.2.3 Friction coefficient 0.1

The friction coefficient is set to be 0.1. Maximum principal stress and vertical deflection distributions of the bridge under self-weight and prestressing are shown in Figs. 4.16 and 4.17, respectively.

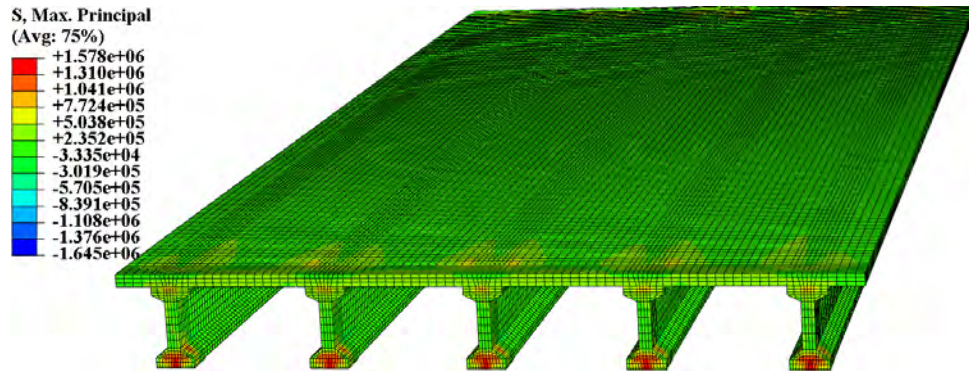


Fig. 4.16 Maximum principal stress distribution under self-weight and prestressing.

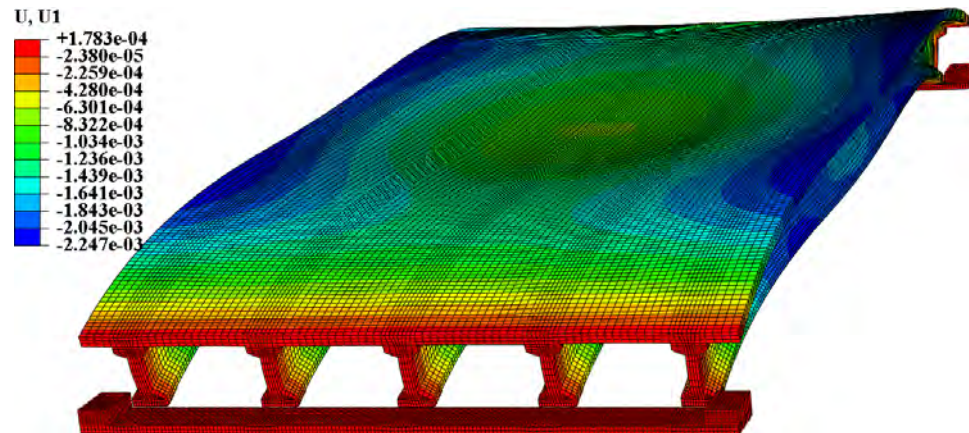
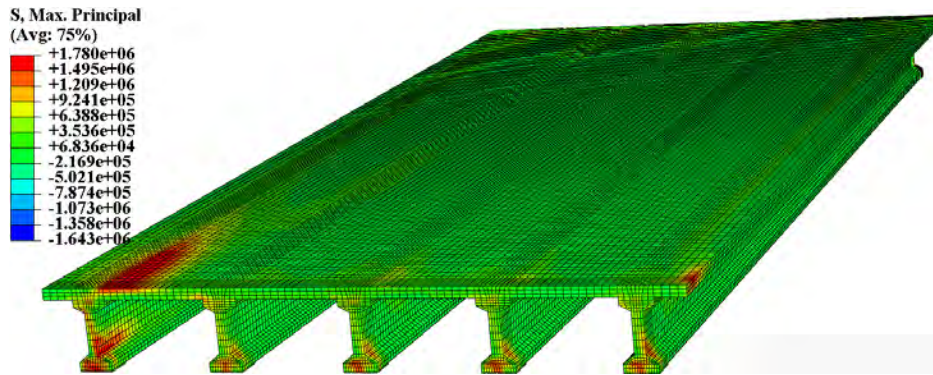
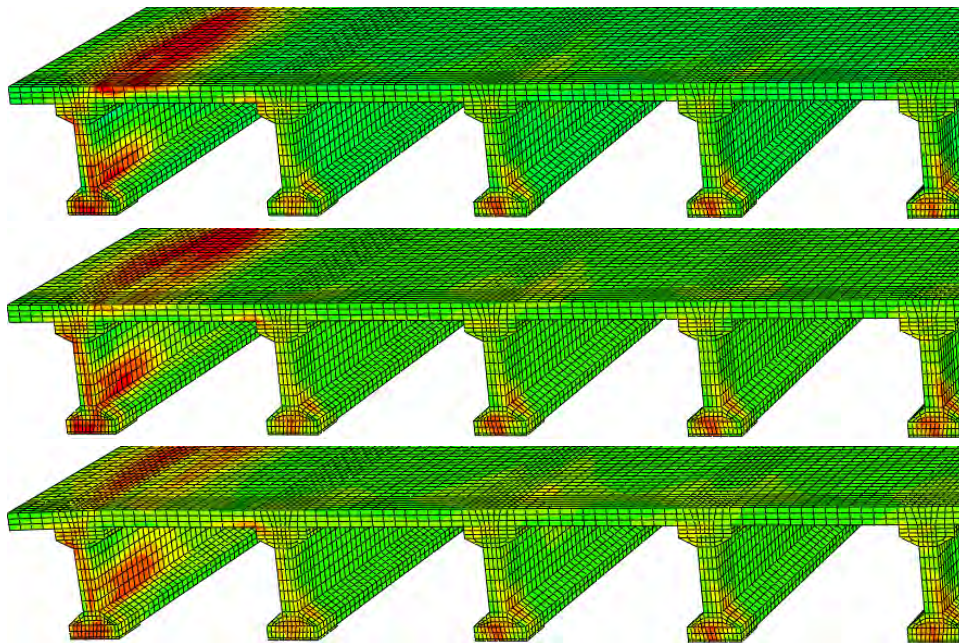


Fig. 4.17 Vertical displacement distribution under self-weight and prestressing. ( $\times 500$ ).

Maximum principal stress distribution under self-weight, prestressing, and transverse force is shown in Fig. 4.18 that shows the cracking initiates at the top of the deck and the web of exterior, simultaneously. The damage development is shown in Fig. 4.19 where the damage propagates in the deck and the end diaphragm; the cracks in girders propagate along the longitudinal direction.



**Fig. 4.18 Maximum principal stress.**



**Fig. 4.19 Damage development in the superstructure.**

The pushover curve is shown in Fig. 4.20. After the contact between E1 and G1 is established, reaction force will be applied to G1. With the increase of loading, maximum principal stress/strain in concrete will increase until crack is formed. Then the structure will undergo a ‘softening’ stage representing the propagation of cracks in the concrete; however, the structure can resist higher load during that stage, because the concrete is reinforced by rebar that can provide tensile strength and restrain the cracking. With the propagation and widening of the cracks, eventually the rebar will yield and thus the structure will lose strength and fail.

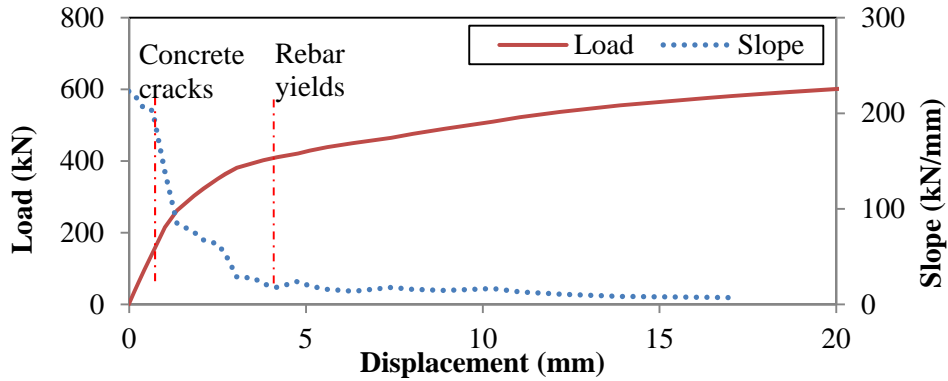


**Fig. 4.20 Pushover curve (Load-Displacement relation).**

Transverse displacement of the bridge under self-weight, prestressing, and transverse force is shown in Fig. 4.21. Overall the superstructure shifted in the transverse direction due to the transverse load, except for G1 and G2 which were restrained by E1.

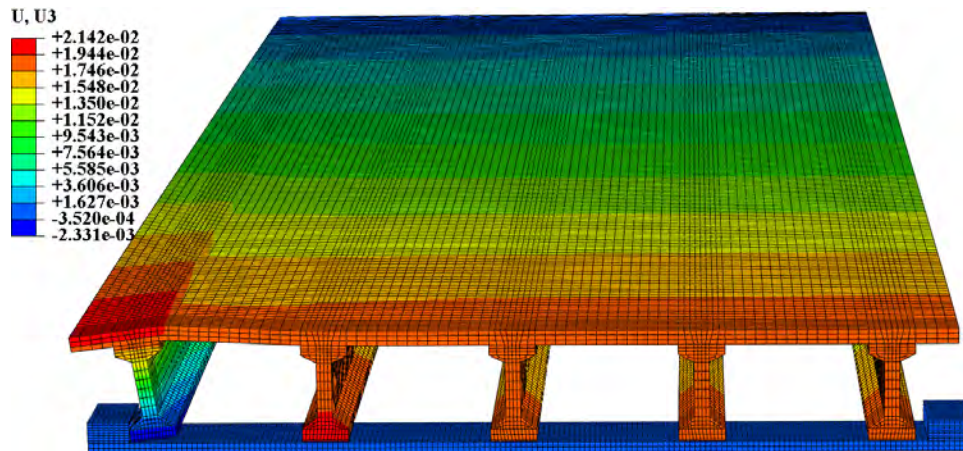


**Fig. 4.21 Transverse displacement. ( $\times 10$ ).**

#### 4.2.4 Frictionless

The friction coefficient is set to be zero. Maximum principal stress and vertical deflection distributions of the bridge under self-weight and prestressing are shown in Figs. 4.22 and 4.23, respectively.

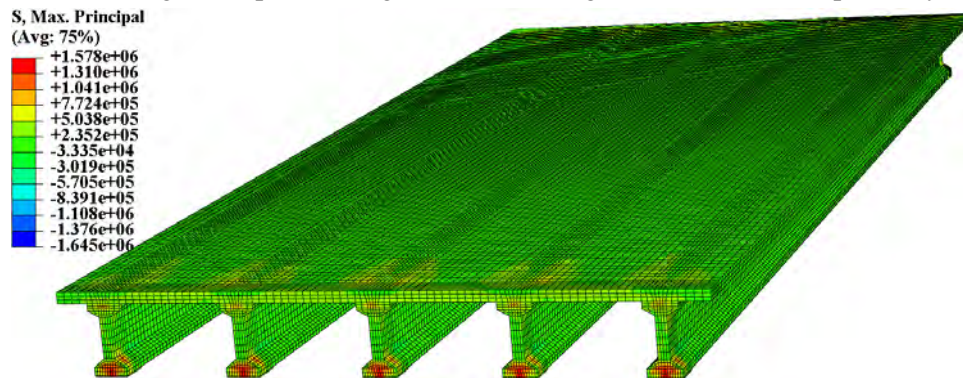


**Fig. 4.22 Maximum principal stress under self-weight and prestressing.**



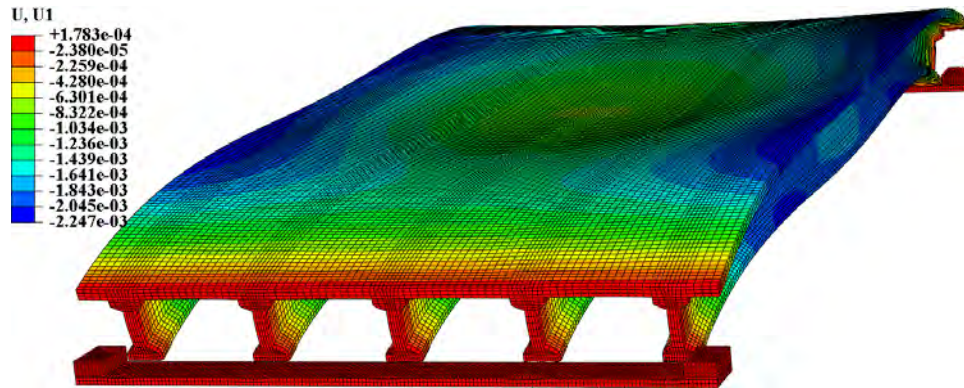


**Fig. 4.23 Vertical deflection under self-weight and prestressing. ( $\times 500$ ).**

Maximum principal stress distribution under self-weight, prestressing, and transverse force is shown in Fig. 4.24 that shows the cracking initiates at the top of the deck and the web of exterior, simultaneously. The damage development is shown in Fig. 4.25 where the damage propagates in the deck and the end diaphragm; the cracks in girders propagate along the longitudinal direction.

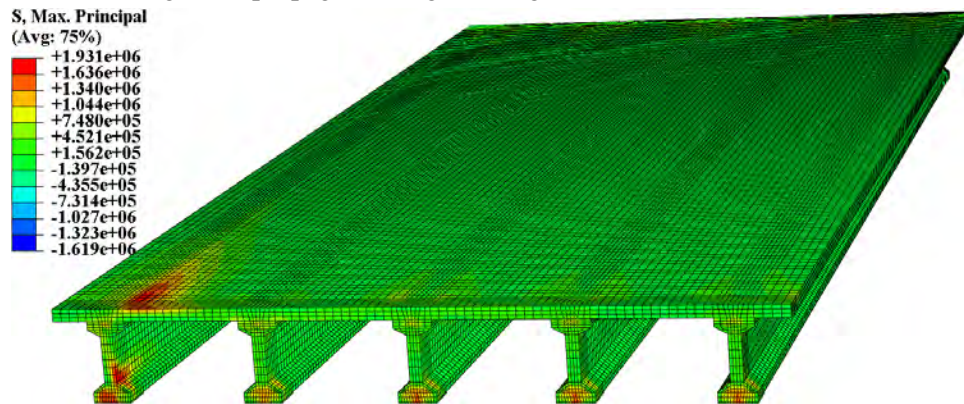


**Fig. 4.24 Maximum principal stress.**

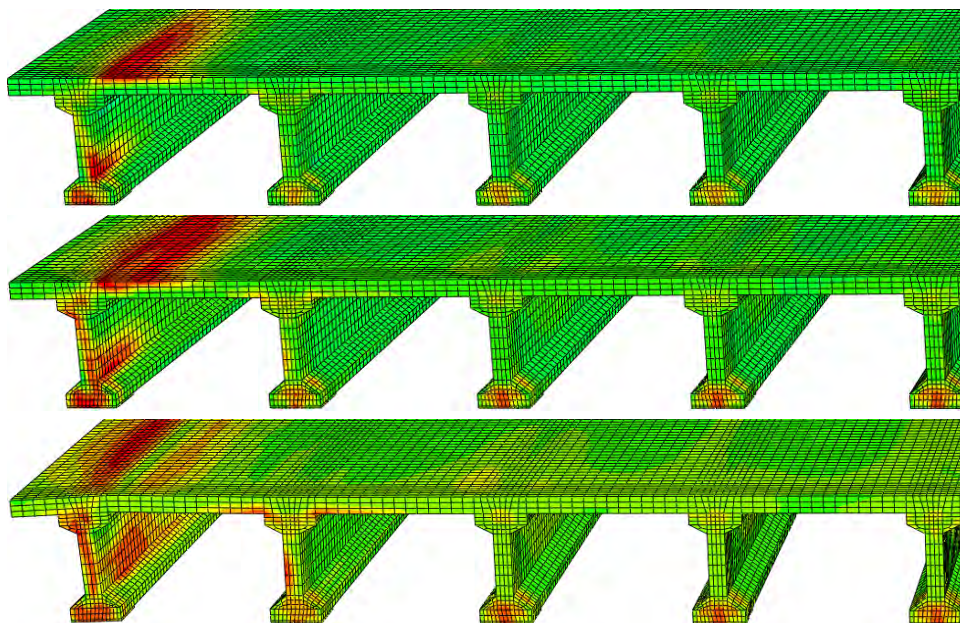


**Fig. 4.25 Damage development in the superstructure.**

The pushover curve is shown in Fig. 4.26. After the contact between E1 and G1 is established, reaction force will be applied to G1. With the increase of loading, maximum principal stress/strain in concrete will increase until crack is formed. Then the structure will undergo a ‘softening’ stage representing the propagation of cracks in the concrete; however, the structure can resist higher load during that stage, because the concrete is reinforced by rebar that can provide tensile strength and restrain the cracking. With the propagation and widening of the cracks, eventually the rebar will yield and thus the structure will lose strength and fail.

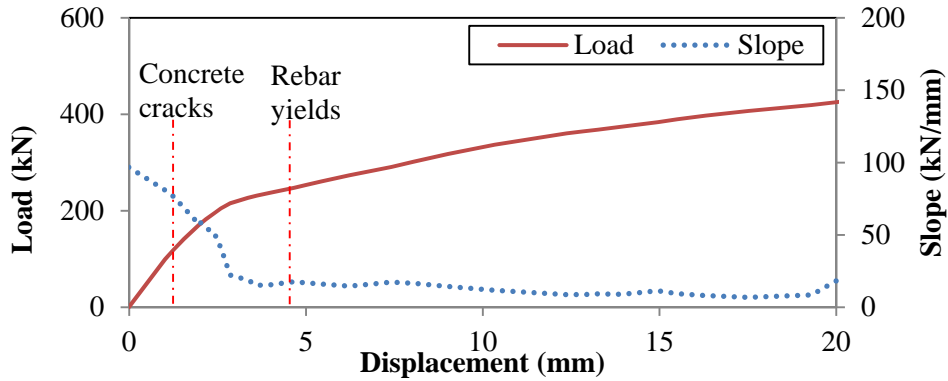


**Fig. 4.26 Pushover curve (Load-Displacement relation).**

Transverse displacement of the bridge under self-weight, prestressing, and transverse force is shown in Fig. 4.27. Overall the superstructure shifted in the transverse direction due to the transverse load, except for G1 and G2 which were restrained by E1.

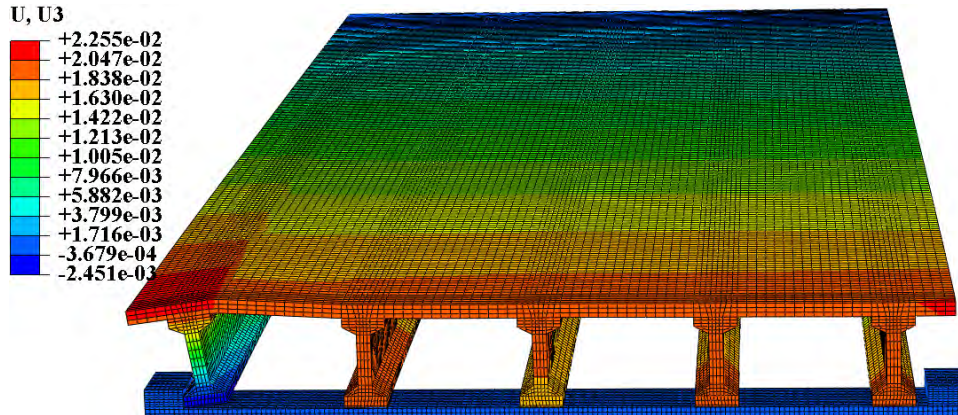


**Fig. 4.27 Transverse drift. ( $\times 10$ ).**

#### 4.2.5 Discussion on friction coefficient

The friction coefficient does not significantly influence the bridge’s responses to self-weight and prestressing, as indicated in Fig. 4.28. No significant change for the deflection and stress distributions was observed with the change of friction coefficient.

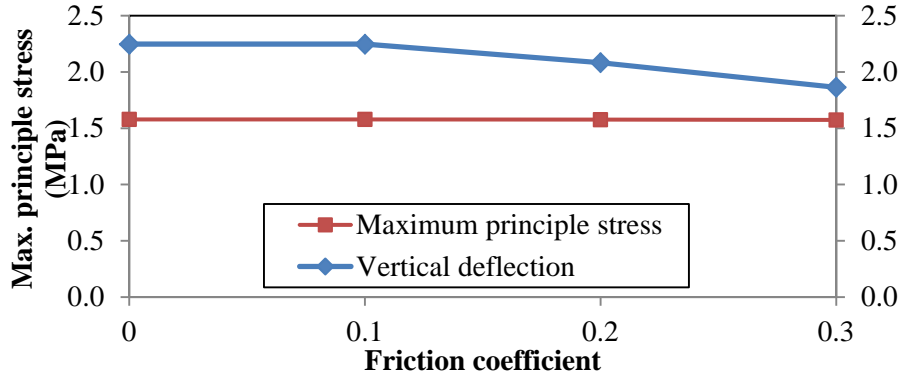


**Fig. 4.28 Influence of friction coefficient on vertical behaviors.**

The pushover curves corresponding to different friction coefficients are compared in Fig. 4.3.20 that demonstrates significant changes due to the friction coefficient. With the increase of friction coefficient, both transverse stiffness and capacity of the superstructure were increased, which was manifested in Fig. 4.30. Friction can restrain the transverse shift of the interior girders, and the reaction forces caused by the constraint can help resist the transverse inertia force. The total transverse reaction force can be distributed to multiple girders instead of concentrating on one single girder. In this way, the transverse stiffness and capacity can be appreciably increased. Up to 128% stiffness and 100% capacity can be gained by increasing the friction coefficient from 0 to 0.3.

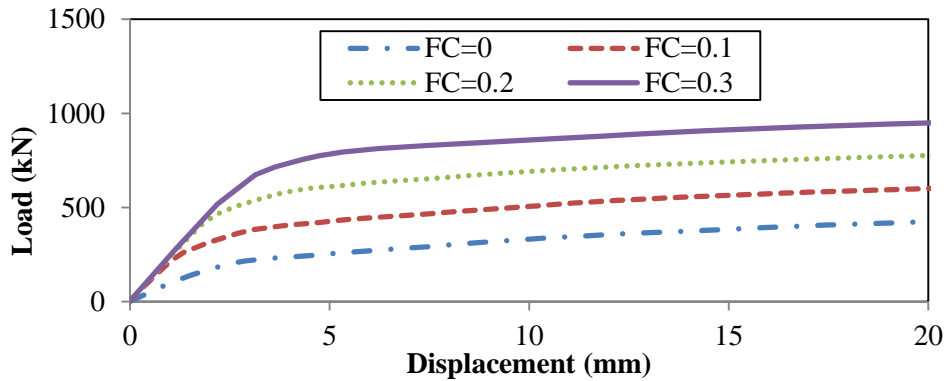


**Fig. 4.29 Comparison of pushover curves of bridges with different friction coefficients.**

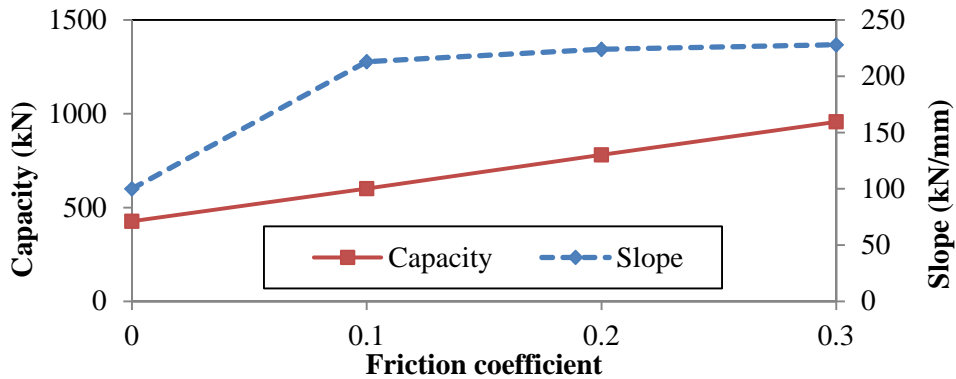


**Fig. 4.30 Influence of friction coefficient on transverse behaviors.**

### 4.3 Analysis of Bridge with Interior Shear Keys

Last section has indicated that the friction between the cap and girder can benefit the superstructure by helping increase the capacity to resist transverse load. However, during the real earthquake, the bridge can be subjected to vertical inertia force and thus the friction force will be decreased or even eliminated. Then the interior girders will not be able to provide resistance to the transverse load. To address this problem, interior shear keys are proposed to constrain the transverse movement of interior girders and thus enable the multiple girders work together to resist the transverse inertia force due to seismic ground motions.

Bridges with four different numbers of interior shear keys were investigated in this section as illustrated in Fig. 4.31. First, self-weight and prestressing were applied to each bridge. And then, the superstructures were pushed by transverse loads until failure. The bridges were evaluated in terms of failure mode, stiffness and capacity.

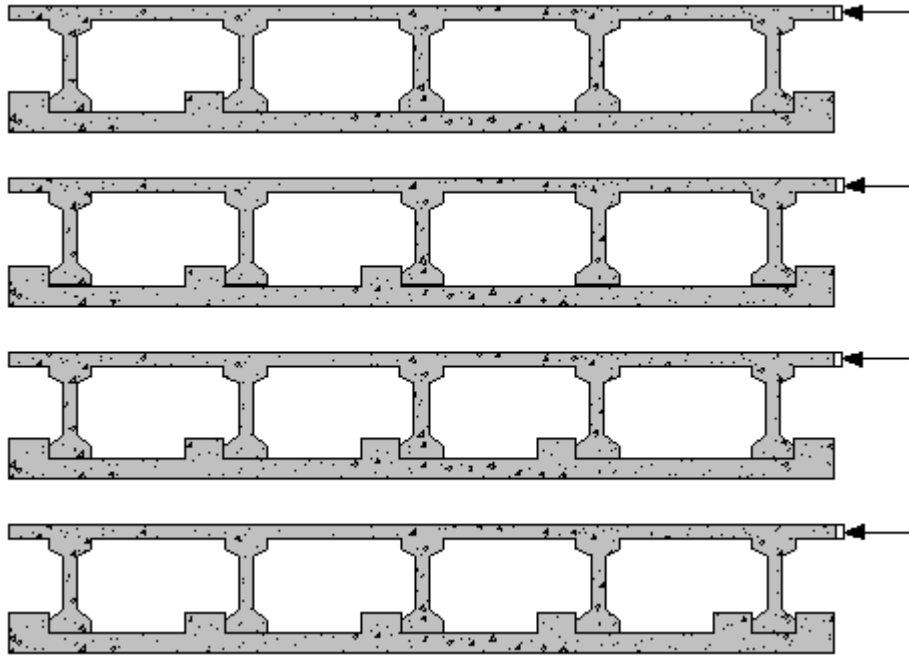


Fig. 4.31 Illustration of the bridges with various interior shear key configurations.

#### 4.3.1 Installed one interior shear key

The FE model of the bridge with one interior shear key is shown in Fig. 4.32.

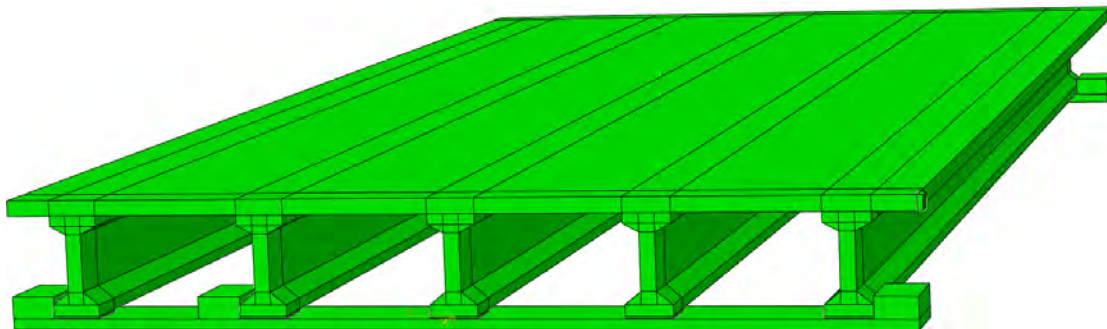
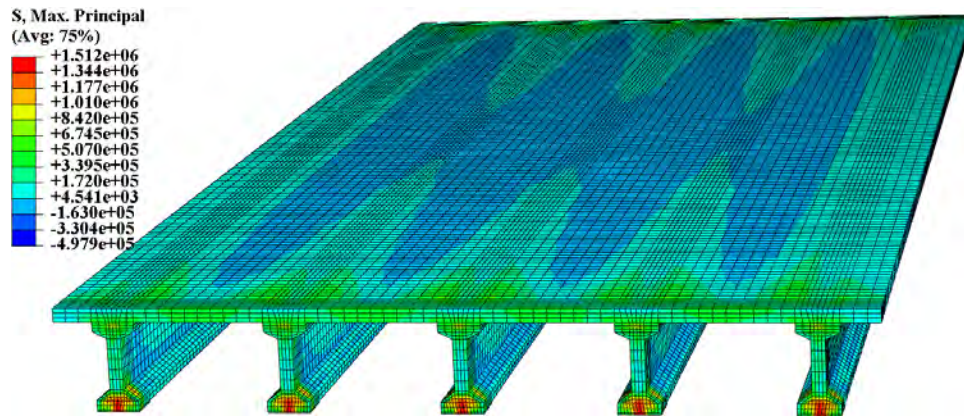


Fig. 4.32 A simplified FE model of bridge installed one interior shear key.

Maximum principal stress and vertical deflection distributions of the bridge under self-weight and prestressing are shown in Figs. 4.33 and 4.34, respectively. Overall the stress was very small, because the

stress due to selfweight was partially balanced by the prestress effect. However, localized stresses were caused by the prestressed tendons at the anchorage zones. The deflection distribution is overall symmetrical about the middle span in the longitudinal direction, and symmetrical about the G3 in the transverse direction.



**Fig. 4.33 Maximum principal stress distribution under self-weight and prestressing.**

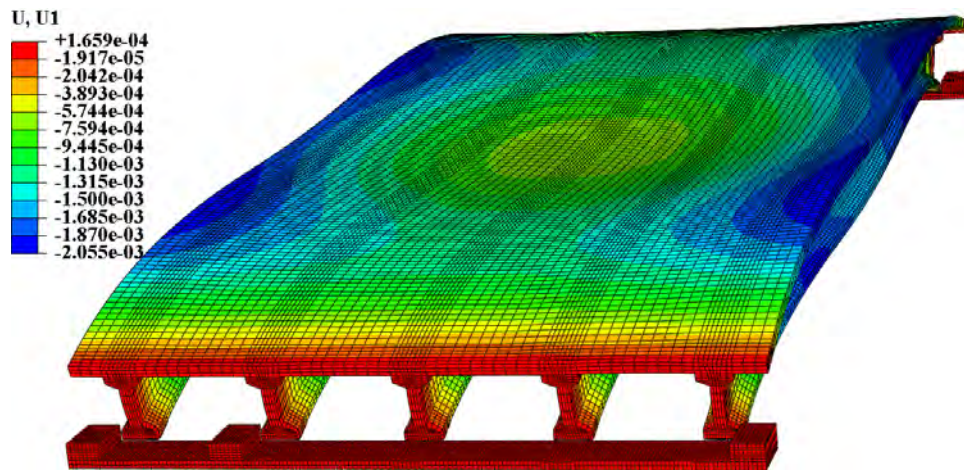


**Fig. 4.34 Vertical displacement distribution under self-weight and prestressing. (×500).**

Maximum principal stress distribution under self-weight, prestressing, and transverse force is shown in Fig. 4.35 that shows the cracking initiates at the top of the deck and the web of exterior and the adjacent interior girders, simultaneously. The damage development is shown in Fig. 4.36 where the damage propagates in the deck and the end diaphragm; the cracks in girders propagate along the longitudinal direction.

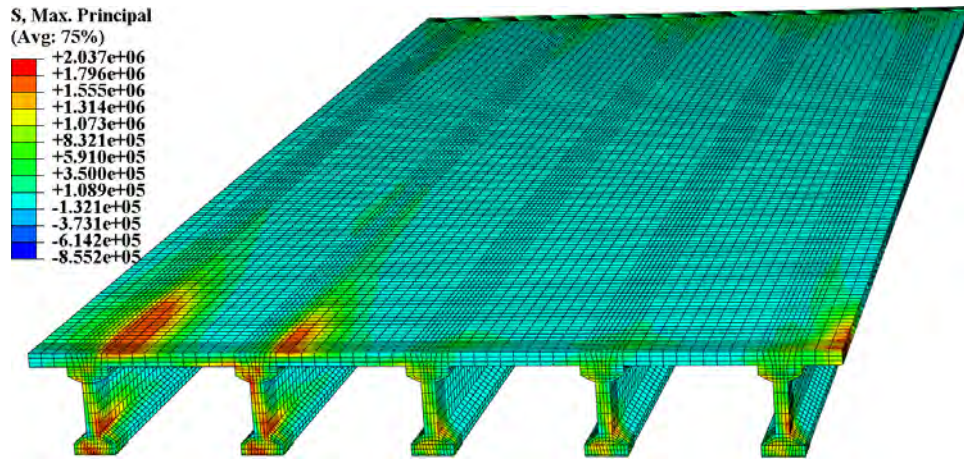


**Fig. 4.35 Maximum principal stress distribution.**

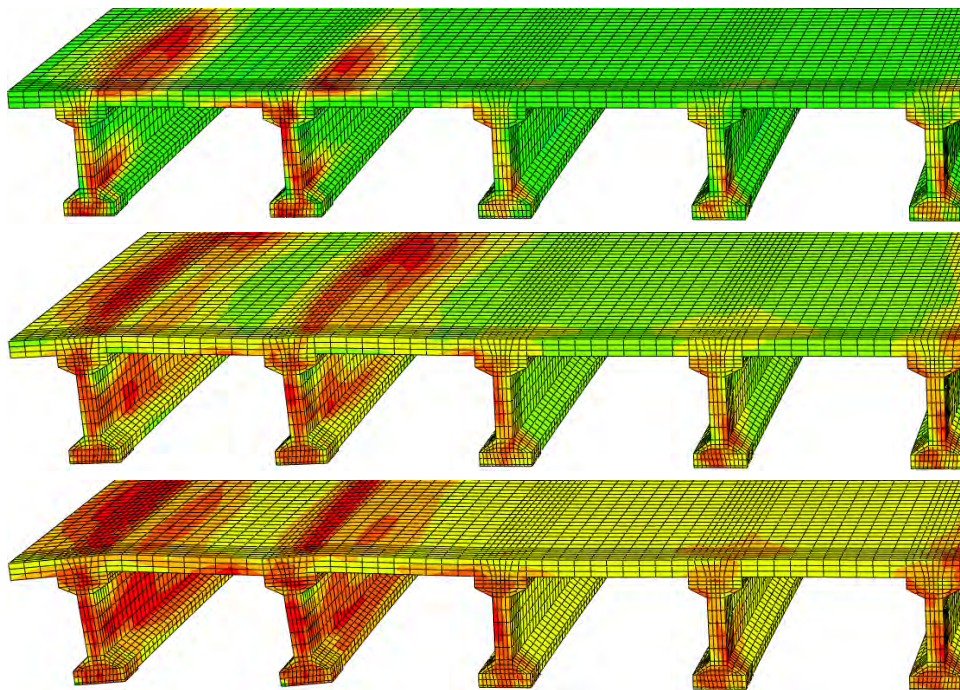


**Fig. 4.36 Damage development in the superstructure.**

The pushover curve is shown in Fig. 3.34.

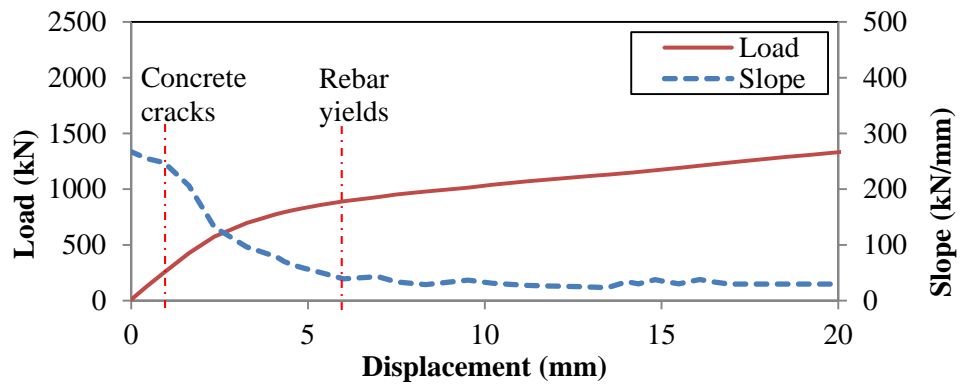


**Fig. 4.37 Pushover curve (Load-Displacement relation).**

Transverse displacement of the bridge under self-weight, prestressing, and transverse force is shown in Fig. 4.3.8. Overall the superstructure shifted in the transverse direction due to the transverse load, except for G1 and G2 which were restrained by E1.

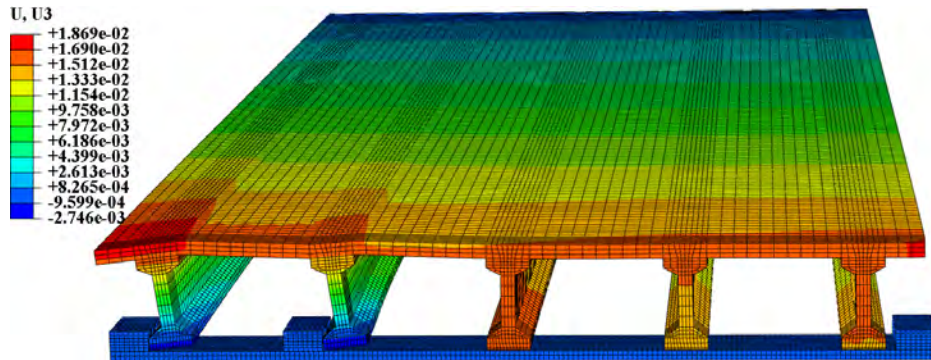


Fig. 4.38 Transverse displacement in the superstructure. ( $\times 10$ ).

### 4.3.2 Installed two interior shear keys

The FE model of the bridge with two interior shear keys is shown in Fig. 4.39. Maximum principal stress and vertical deflection distributions of the bridge under self-weight and prestressing are shown in Figs. 4.40 and 4.41, respectively. Overall the stress was very small, because the stress due to selfweight was partially balanced by the prestress effect. However, localized stresses were caused by the prestressed tendons at the anchorage zones. The deflection distribution is overall symmetrical about the middle span in the longitudinal direction, and symmetrical about the G3 in the transverse direction.

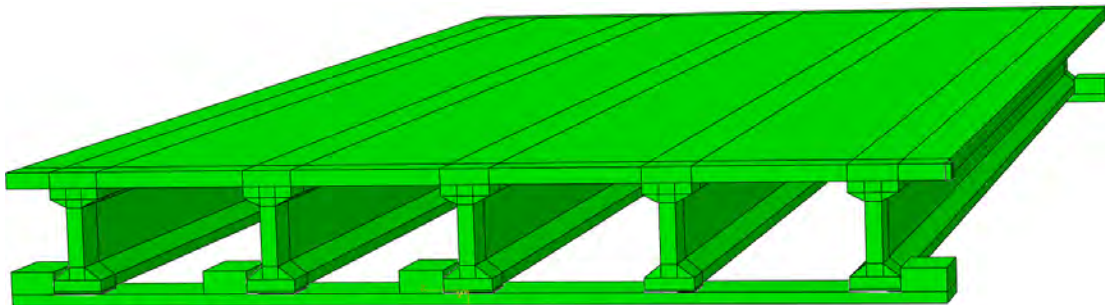


Fig. 4.39 A simplified FE model of bridge installed two interior shear key.

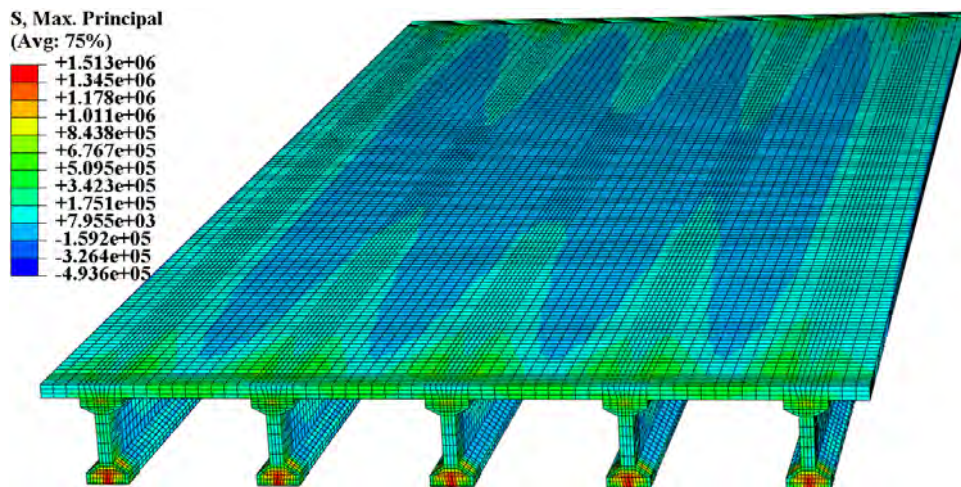
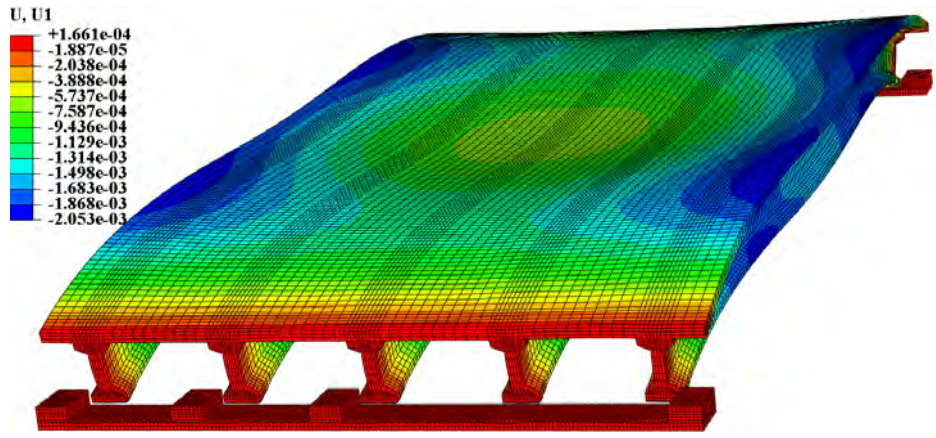
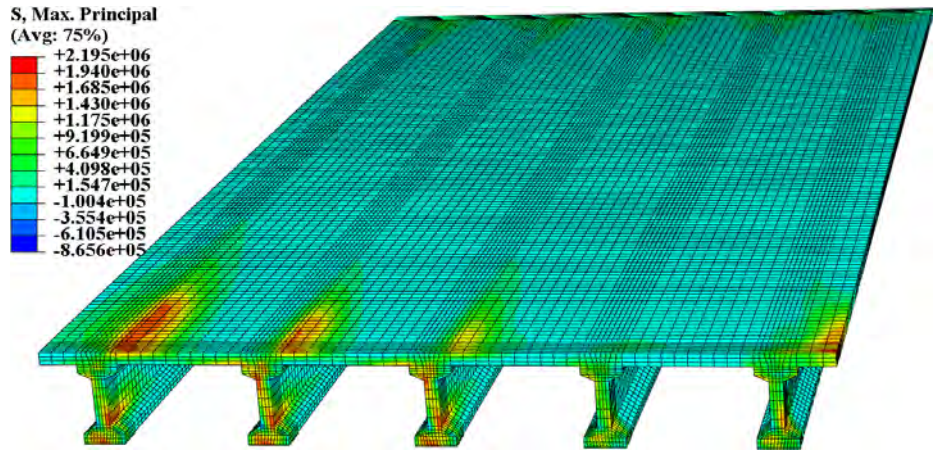


Fig. 4.40 Maximum principal stress under self-weight and prestressing.



**Fig. 4.41 Vertical displacement distribution under self-weight and prestressing. ( $\times 500$ ).**

Maximum principal stress distribution under self-weight, prestressing, and transverse force is shown in Fig. 4.42. Cracking initiates at the top of the deck and the web of exterior and the adjacent interior girders, simultaneously. The damage development is shown in Fig. 4.43 where the damage propagates in the deck and the end diaphragm; the cracks in girders propagate along the longitudinal direction.



**Fig. 4.42 Maximum principal stress in the superstructure.**

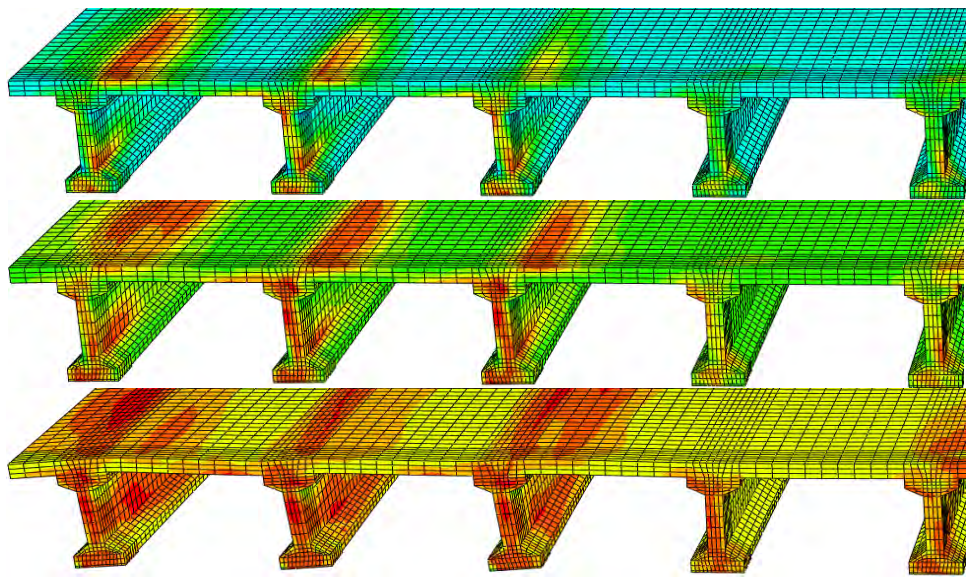


**Fig. 4.43 Damage development in the superstructure.**



The pushover curve is shown in Fig. 4.44.

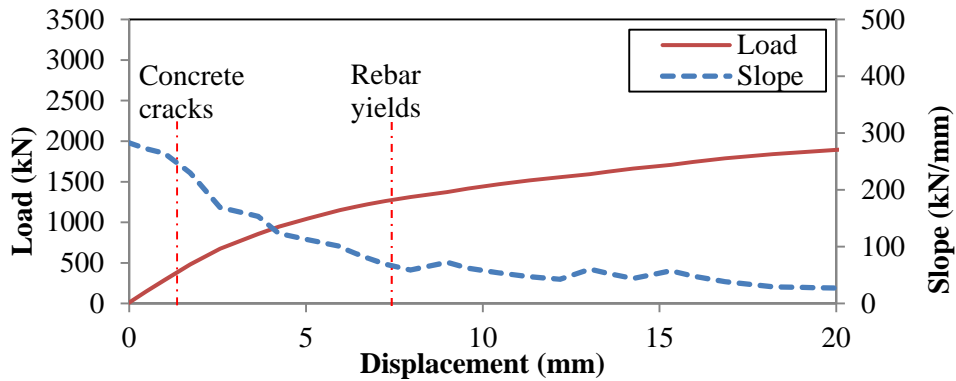


**Fig. 4.44 Pushover curve (Load-Displacement relation).**

Transverse displacement of the bridge under self-weight, prestressing, and transverse force is shown in Fig. 4.45. Overall the superstructure shifted in the transverse direction due to the transverse load, except for G1, G2 and G3, which were restrained by E1.

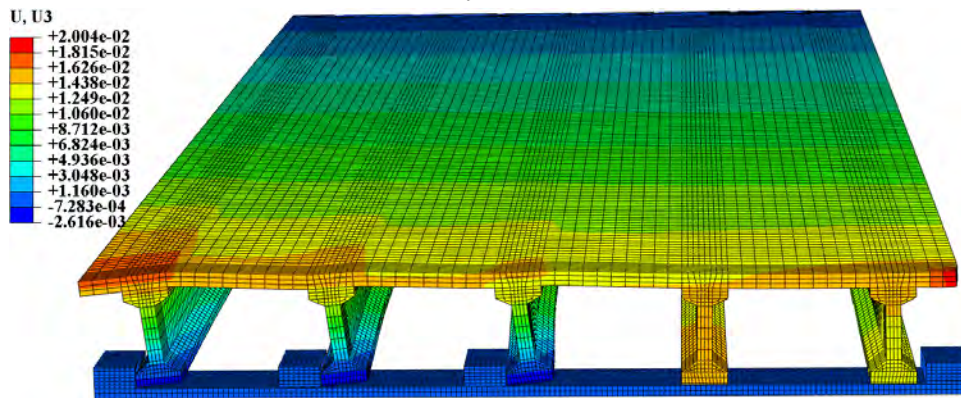


**Fig. 4.45 Transverse drift. ( $\times 10$ ).**

### 4.3.3 Installed three interior shear keys

The FE model of the bridge with two interior shear keys is shown in Fig. 4.46. Maximum principal stress and vertical deflection distributions of the bridge under self-weight and prestressing are shown in Figs. 4.47 and 4.48, respectively. Overall the stress was very small, because the stress due to selfweight was partially balanced by the prestressing effect. However, localized stresses were caused by the prestressed tendons at the anchorage zones. The deflection distribution is overall symmetrical about the middle span in the longitudinal direction, and symmetrical about the G3 in the transverse direction.

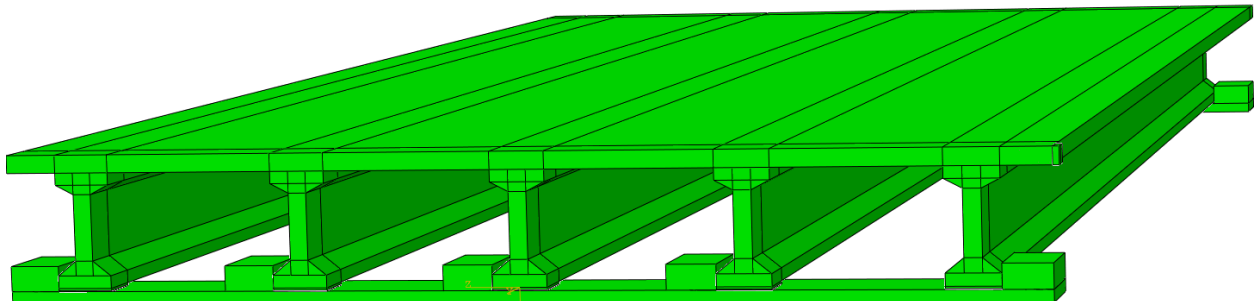


**Fig. 4.46 A simplified FE model of bridge installed three interior shear key.**

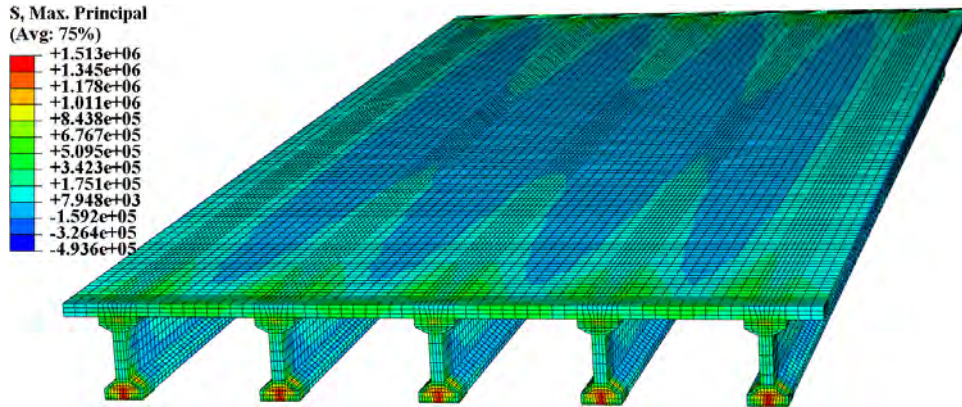


Fig. 4.47 Maximum principal stress under self-weight and prestressing.

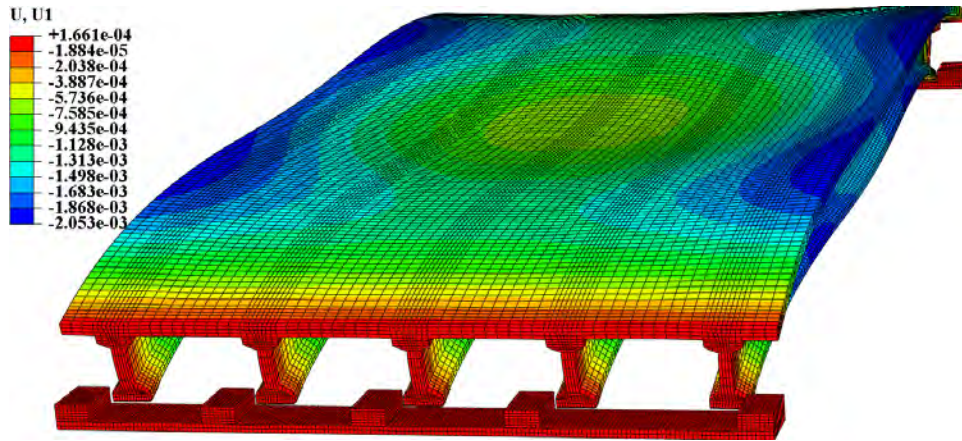


Fig. 4.48 Vertical deflection under self-weight and prestressing. ( $\times 500$ ).

Maximum principal stress distribution under self-weight, prestressing, and transverse force is shown in Fig. 4.49 that shows the cracking initiates at the top of the deck and the web of exterior and the adjacent interior girders, simultaneously. The damage development is shown in Fig. 4.50 where the damage propagates in the deck and the end diaphragm; the cracks in girders propagate along the longitudinal direction.

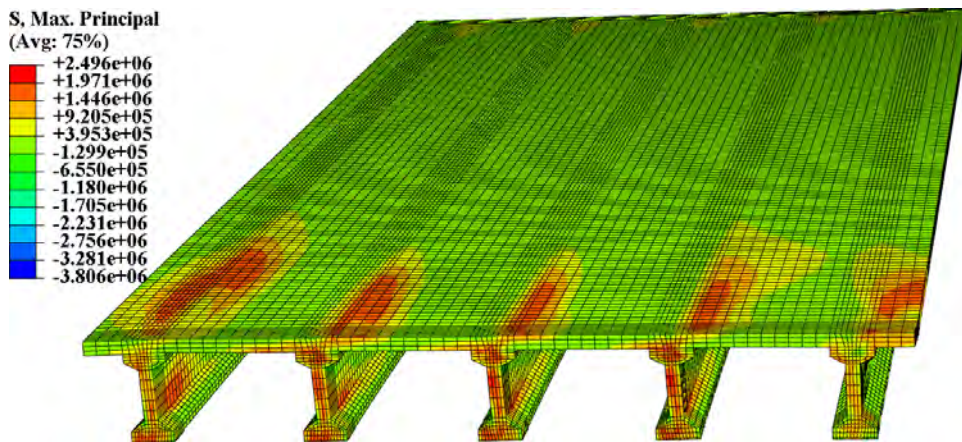
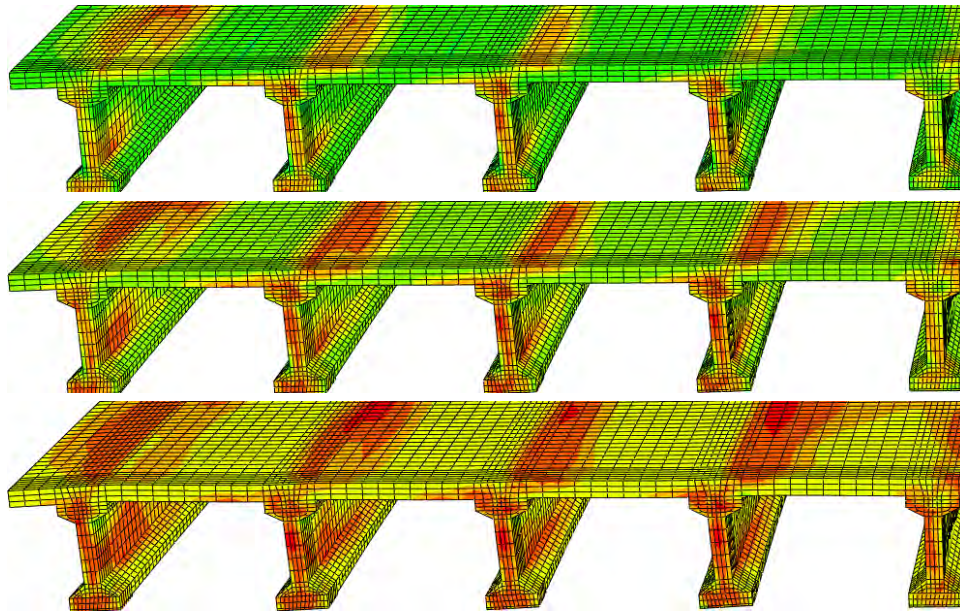
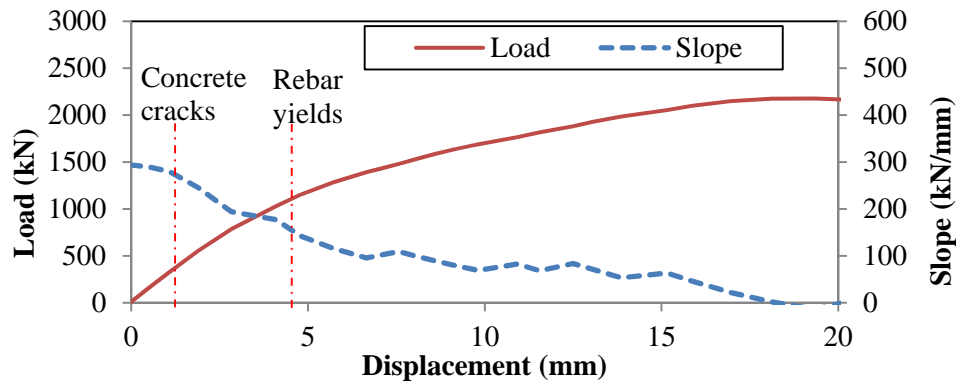


Fig. 4.49 Maximum principal stress. ( $\times 10$ ).



**Fig. 4.50** Damage development in the superstructure.

The pushover curve is shown in Fig. 4.51.



**Fig. 4.51** Pushover curve (Load-Displacement relation).

Transverse displacement of the bridge under self-weight, prestressing, and transverse force is shown in Fig. 4.52. Overall the superstructure shifted in the transverse direction due to the transverse load, except for G1, G2 and G3, which were restrained by E1.

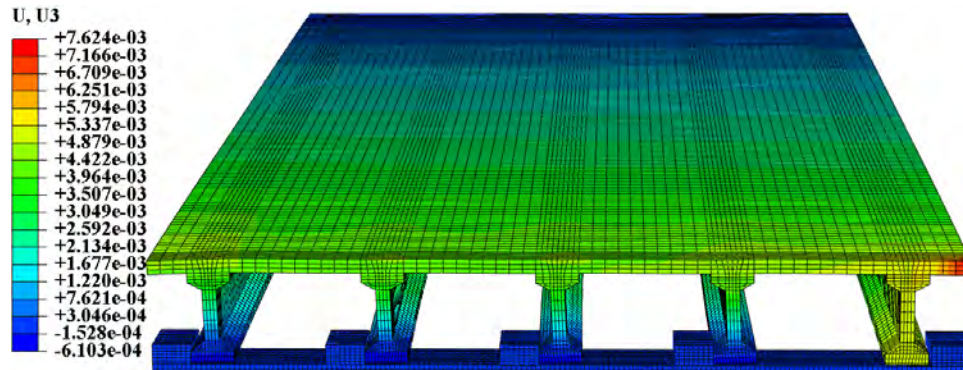


**Fig. 4.52** Transverse drift. ( $\times 10$ ).

#### 4.3.4 Installed four interior shear keys

The FE model of the bridge with two interior shear keys is shown in Fig. 4.53. Maximum principal stress and vertical deflection distributions of the bridge under self-weight and prestressing are shown in Figs. 4.54 and 4.55, respectively. Overall the stress was very small, because the stress due to selfweight was partially balanced by the prestressing effect. However, localized stresses were caused by the prestressed tendons at the anchorage zones. The deflection distribution is overall symmetrical about the middle span in the longitudinal direction, and symmetrical about the G3 in the transverse direction.

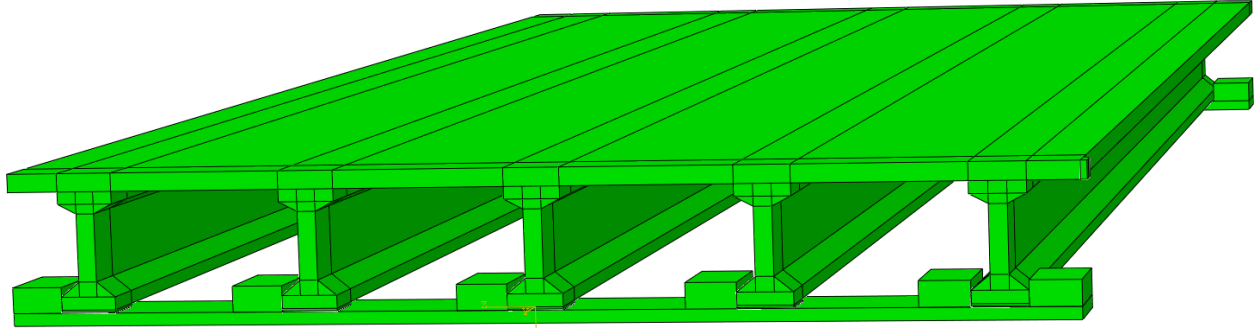


Fig. 4.53 A simplified FE model of bridge installed four interior shear key.

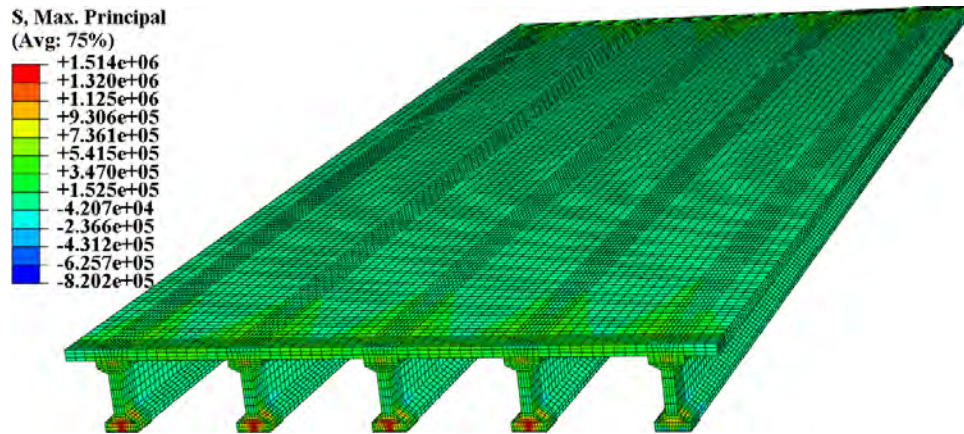


Fig. 4.54 Maximum principal stress under self-weight and prestressing.

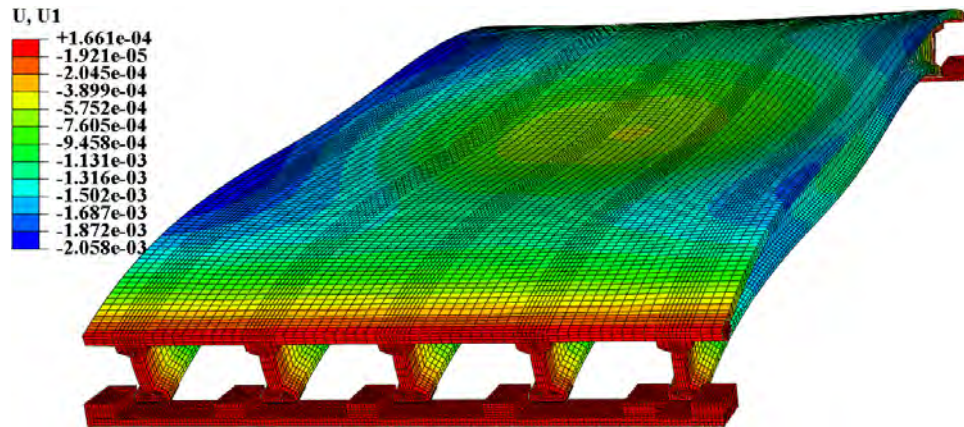
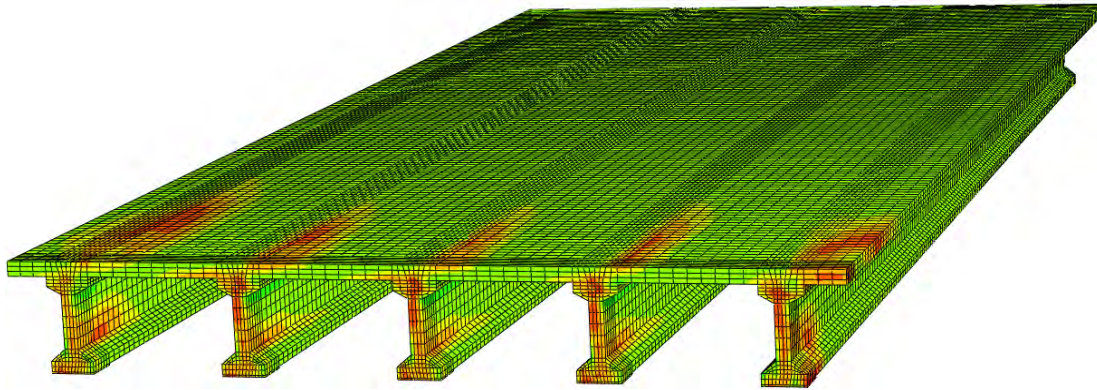


Fig. 4.55 Vertical deflection under self-weight and prestressing. ( $\times 500$ ).

Maximum principal stress distribution under self-weight, prestressing, and transverse force is shown in Fig. 4.56 that shows the cracking initiates at the top of the deck and the web of exterior and the adjacent interior girders, simultaneously. The damage development is shown in Fig. 4.57 where the

damage propagates in the deck and the end diaphragm; the cracks in girders propagate along the longitudinal direction.



**Fig. 4.56 Maximum principal stress.**

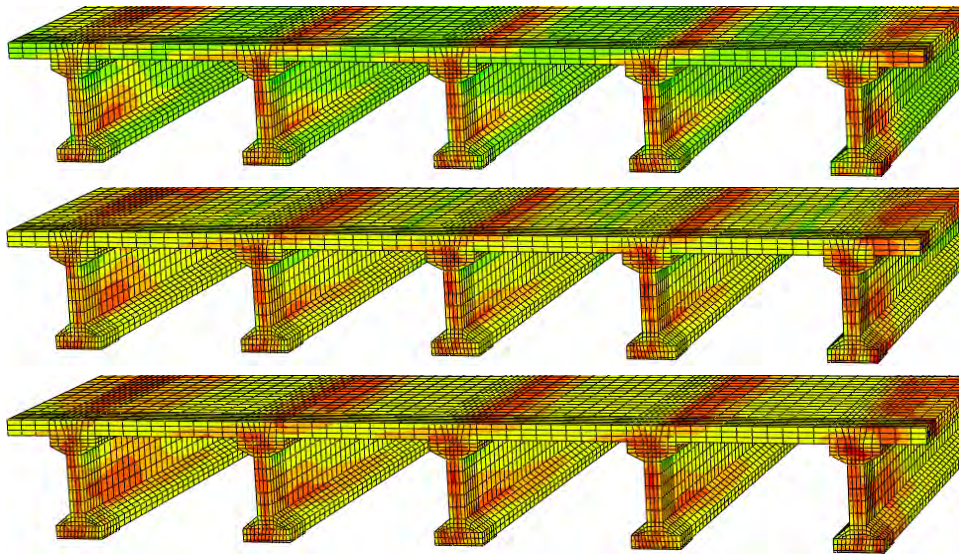


**Fig. 4.57 Damage development in the superstructure.**

The pushover curve is shown in Fig. 4.58.

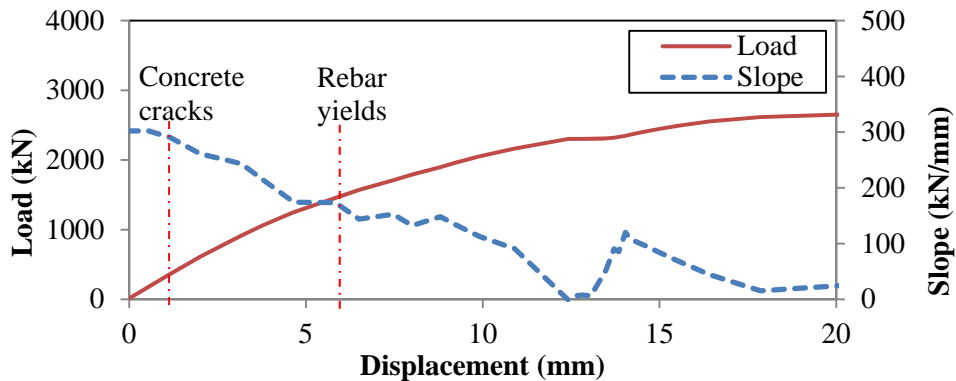


**Fig. 4.58 Pushover curve (Load-Displacement relation).**

Transverse displacement of the bridge under self-weight, prestressing, and transverse force is shown in Fig. 4.59. Overall the superstructure shifted in the transverse direction due to the transverse load, except for G1, G2 and G3, which were restrained by E1.

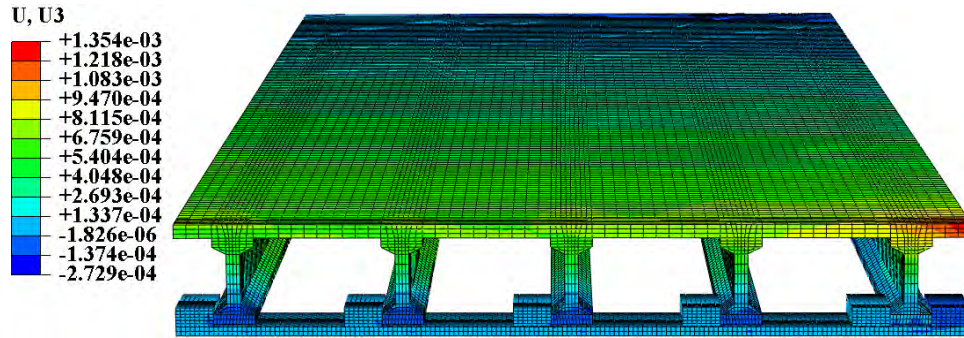


Fig. 4.59 Transverse drift. ( $\times 10$ ).

#### 4.3.5 Discussion on interior shear key

The interior shear key does not significantly influence the bridge's responses to self-weight and prestressing, as indicated in Fig. 4.60. No significant change for the deflection and stress distributions was observed with the change of interior shear key number.

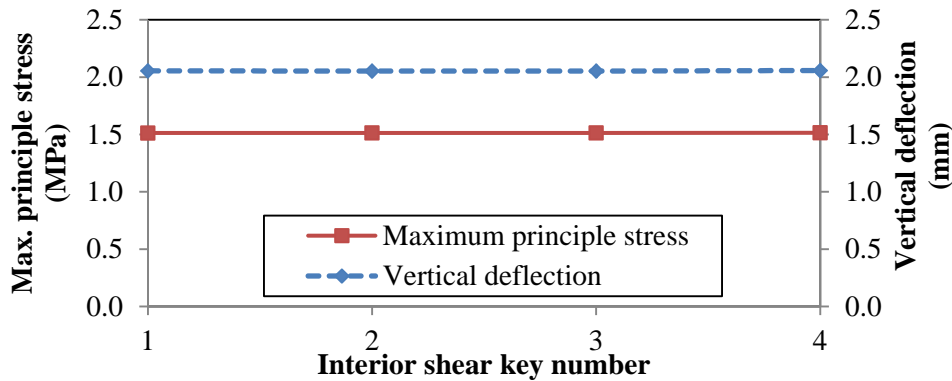
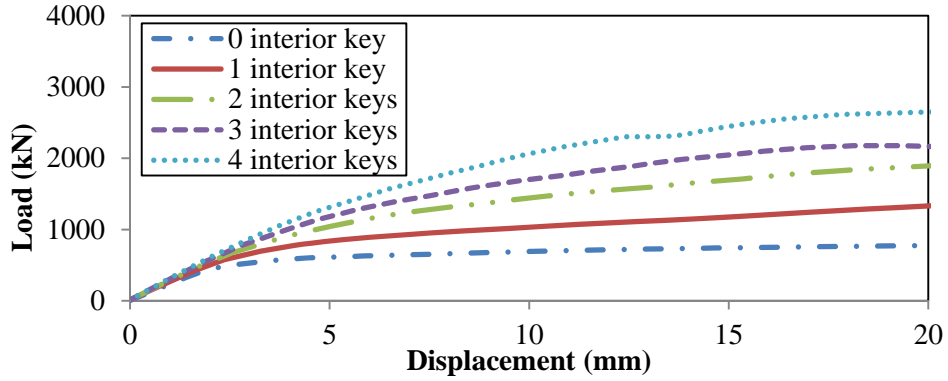


Fig. 4.60 Influence of interior shear key number on vertical behaviors.

The pushover curves corresponding to different interior shear key configurations are compared in Fig. 4.61 that demonstrates significant changes due to the shear key. With the increase of interior shear key, both transverse stiffness and capacity of the superstructure were increased, which was manifested in Fig. 4.62. Interior shear keys can constrain the transverse shift of the interior girders, and the reaction forces caused by the constraint can help resist the transverse inertia force. The total transverse reaction force can be distributed to multiple girders instead of concentrating on one single girder. In this way, the transverse stiffness and capacity can be appreciably increased. Up to 35% stiffness and 240% capacity can be gained by increasing the interior shear key number from 0 to 4.

Interior shear key provides an alternative to enhance the structure's performance under earthquake, and as a matter of fact, it is a more robust and reliable way than to increase the friction coefficient. When the superstructure is subjected to an upward inertia force, the normal contact force provided by the cap will decrease and thus the friction will be reduced. However, no matter whether the vertical inertia force is upward or downward, the interior shear key can always provide transverse reaction force as long as the contact is established.



**Fig. 4.61 Comparison of pushover curves of bridges with different numbers of interior shear keys.**

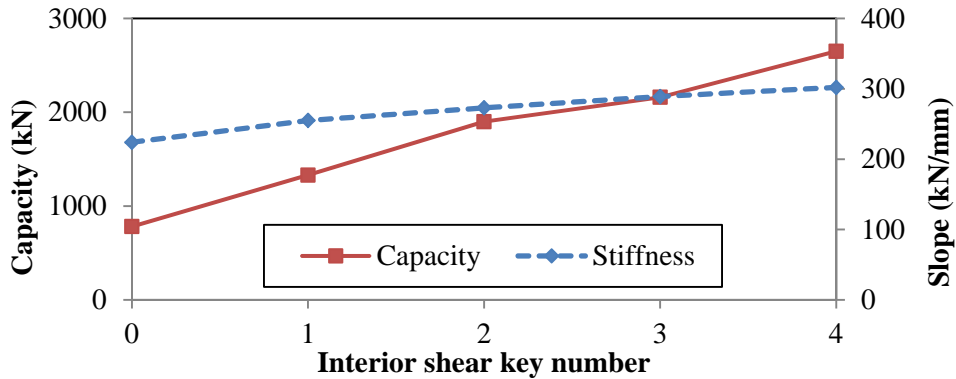


**Fig. 4.62 Influence of interior shear key number on transverse behaviors.**

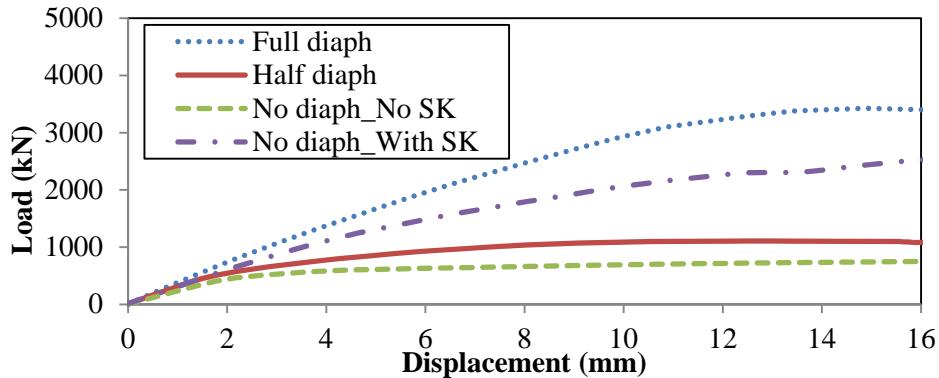


**Fig. 4.63 Comparison of pushover curves of different bridges.**

The simulations for each case have been introduced in the preceding sections with failure mode and the progressive failure process demonstrated. The comparisons of the pushover curves are shown in Fig. 4.63, including the bridges that have full or half end diaphragms, bridge that has neither end diaphragm nor interior shear key, and bridge that does not have end diaphragm but have interior shear keys. The bridge that has full end diaphragms provides the highest capacity, and thus can perform best in earthquakes. The capacities of bridges that have partial end diaphragms and do not have interior shear keys are low, so they demonstrate more damage. Bridge that does not have end diaphragm can gain benefit from interior shear keys that help multiple girders work together, so even though the capacity is not as high as that of the bridge with full end diaphragm, such bridge can also perform well in earthquakes. Another reason is such bridge is not as stiff as the bridge with full diaphragm in the transverse direction and has better ductility, so the demand capacity is lower.

#### 4.4 Summary

In this section, bridges without end diaphragm but with interior shear keys were investigated. The influences of the friction coefficient and the number of interior shear keys were evaluated in terms of the failure mode and capacity under self-weight, prestressing, and transverse load.

The bridge's vertical behaviors were not significantly influenced by the end diaphragm and the friction coefficient of the supports. Within the investigation scope, less than 10% change was observed. However, the bridge's transverse behaviors are significantly influenced by end diaphragm and the friction coefficient of the supports.

For bridges that have neither interior shear keys nor end diaphragm, damages usually initiate near the joint of the exterior girder and the end diaphragm. This was in good agreement with the observations of damages in real world bridge. When the FC was varied from 0 to 0.3, the capacity linearly increased from 427 to 957 kN; however, the change of stiffness is nonlinear. The curve can be divided into two parts by one data point that corresponds to 0.1 FC. There was a sudden increase from 0 to 0.1.

When the bridges are instrumented with interior shear keys, the capacity can be significantly increased. With the increase of interior shear key number, both transverse stiffness and capacity of the superstructure were increased. Interior shear keys can constrain the transverse shift of the interior girders, and the reaction forces caused by the constraint can help resist the transverse inertia force. The total transverse reaction force can be distributed to multiple girders instead of concentrating on one single girder. In this way, the transverse stiffness and capacity can be appreciably increased. Up to 35% stiffness and 240% capacity increases have been demonstrated when the interior shear key number was changed from 0 to 4.

Interior shear key provides an alternative to enhance the structure's performance under earthquake, and as a matter of fact, it is a more robust and reliable way than to increase the friction coefficient. When the superstructure is subjected to an upward inertia force, the normal contact force provided by the cap will decrease and thus the friction will be reduced. However, no matter whether the vertical inertia force is upward or downward, the interior shear key can always provide transverse reaction force as long as the contact is established.

By the comparison of pushover curves corresponding to different structures, the observations of the FHWA team during the Chile earthquake were understood, and it was verified that bridge superstructures with no end diaphragms between girders can be alternatives to the well-understood superstructures with end diaphragms when interior shear keys are provided.



## SECTION 5 DESIGN AND EVALUATION OF DUCTILE SHEAR KEYS

### 5.1 Introduction of Shear Keys

Shear keys are often designed in bridge caps or abutments to provide transverse support to the bridge superstructure under lateral loads. They are of vital importance in resisting seismic loads. Shear keys in bridge applications are divided into two types, exterior or interior. Both of them can restrain the transverse movement of bridge superstructure. The contact reaction forces are transferred to the abutments or caps. To avoid damaging the abutments or caps, the shear keys are usually designed as sacrificial.<sup>25</sup> Once their capacity is exceeded, the shear keys will be damaged and will not provide further support. Energy is dissipated in the damage of the shear keys instead of breaking the vertical elements and causing collapse.

In the current design, the shear keys are fixed on the abutment or cap. Such design leads to ease of construction. However, there are some disadvantages for such design. First, when the shear keys are broken, it will be difficult to repair or replace them. Secondly, the shear keys are rigid before the rupture of concrete, which limits the ductility of the bridge. Thirdly, the function to help multiple girders work together cannot be fully explored. The function and effectiveness of fixed interior shear keys have been introduced in Chapter 4. Even though the shear keys can significantly increase the capacity if the girders contact the shear keys simultaneously, the construction accuracy may not always be able to meet the requirements. When one girder contacts the shear key, there might be gaps between the other girders and their shear keys. As indicated in Chapter 4, the girders are sensitive to the gaps. Millimeter-order gaps can significantly influence the bridge's performance. Since the fixed shear keys are rigid, the girder's transverse movement will be totally constrained and thus will be damaged before other girders. Designs for ductile shear keys were proposed, of which the failure process is ductile instead of brittle. But the shear keys were still fixed by concrete, and would not demonstrate ductility until the rupture of concrete.

### 5.2 A Novel Design of Movable Shear Key

To address this demerit, the concept of 'movable shear key' is proposed, which means the shear key is not fixed but can slide on the abutment or cap, which is illustrated in Fig. 5.1. Comparison of a fixed shear key and a movable shear key is demonstrated in Fig. 5.2.

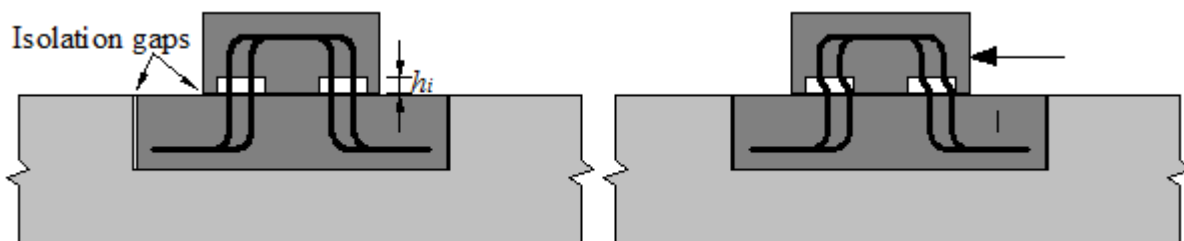
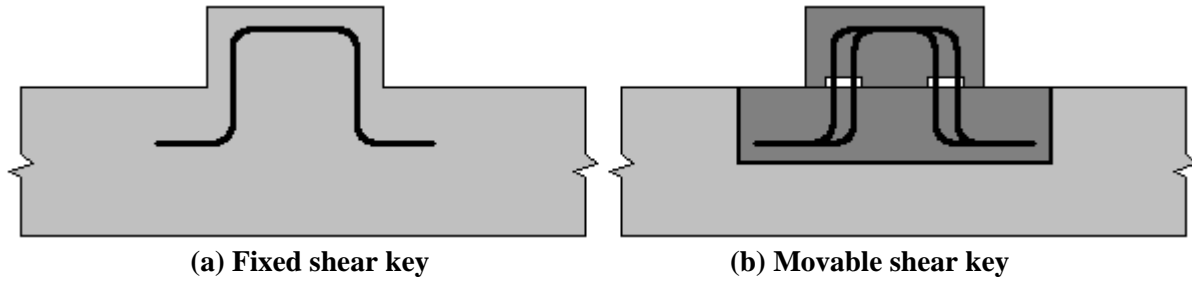


Fig. 5.1 Illustration of the movable shear key.

Movable shear keys mainly make use of rebar to provide transverse restraint instead of concrete, which enables better ductility, because the ductility of steel is far better than that of concrete. The stiffness and capacity can be conveniently designed by adjusting the amount of bars. By properly using movable shear keys that have lower stiffness than fixed shear keys, the capacity of superstructure can be improved by decreasing the sensitivity to gaps, and the ductility of the bridge can be significantly improved.

The movable shear keys can either be cast in the field or prefabricated. By presetting the isolation gaps, the shear keys are easy to be repaired or replaced. The whole part can be conveniently picked up for repair, or removed for replacement, which enables accelerated bridge construction and rehabilitation.



**Fig. 5.2 Comparison of fixed shear key and movable shear key.**

### 5.3 Implementation

The implementation of the movable shear key in bridge application is shown in Fig. 5.3 where fixed shear keys are replaced by movable shear keys. Under a transverse load, which simulates the transverse inertia force due to seismic ground motions, the bridge superstructure shifts; meanwhile, the shear keys slides along the abutment/pier cap due to the contact force. In this figure, for simplification purpose, only the shear keys on the left side were displayed. In real application, the shear keys can be installed on both sides to help resist cyclic earthquake effect.

The movable shear keys can be conveniently installed by simply being laid down in the preset pits.

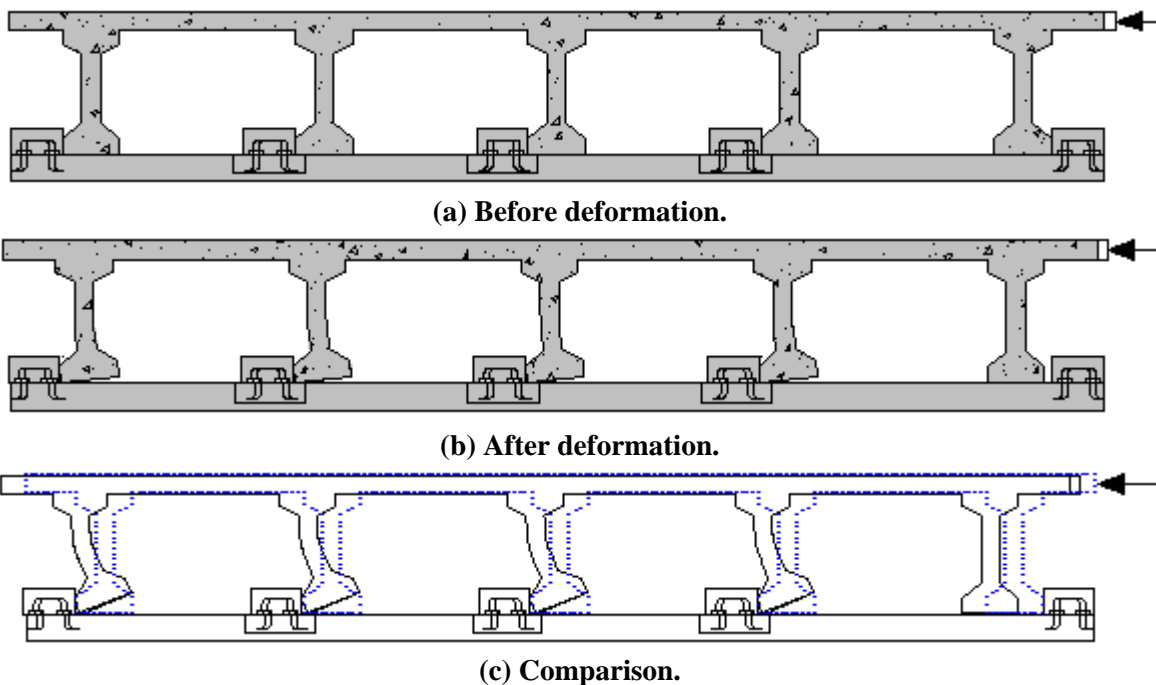


**Fig. 5.3 Implementation of the proposed movable shear key in bridge application.**

### 5.4 Analytical Models

The working principles of the movable shear key are interpreted by a model of compound springs which is schematically illustrated in Fig. 5.4 where the friction is neglected for simplification purpose, which is conservative in accordance with the discussion in Sections 3 and 4. Since the shear keys shift together with the girders after the contact is established, as shown in Fig. 5.3, each contacting pair can be abstracted to be two springs in series as shown in Fig. 5.5. When multiple contacts are established as shown in Fig. 5.4, the series springs will consist parallel spring. Each spring can be defined with elastic and plastic material properties.

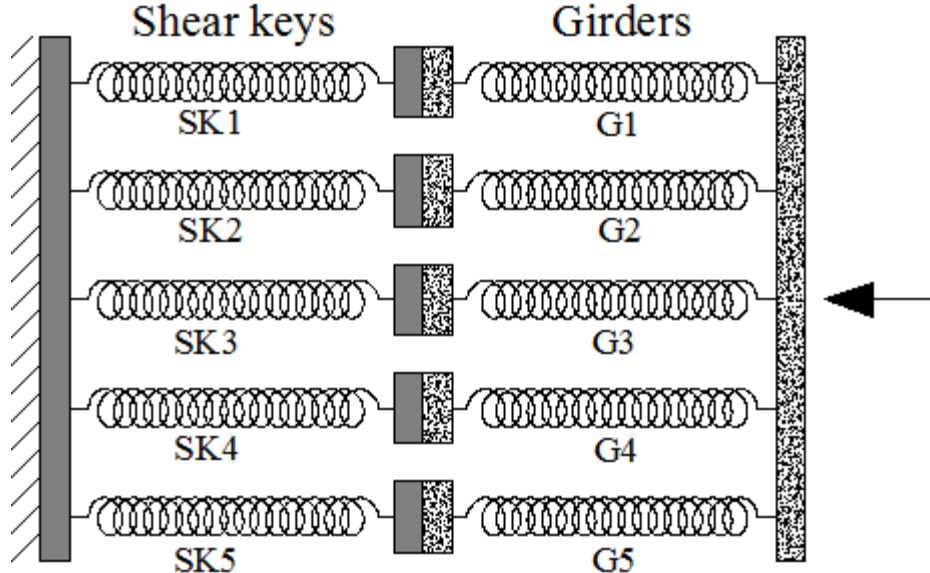


Fig. 5.4 The model of compound springs.

#### 5.4.1 Series springs

The transverse shift stiffness of a shear key is denoted by  $S_{SKi}$ ; the stiffness of a girder is denoted by  $S_{Gi}$ . The left boundary is fixed; the right side is subjected to a concentrated force. Under such boundary conditions, the length changes corresponding to the shear key and the girder are  $\Delta_{SKi}$  and  $\Delta_{Gi}$ , respectively. The total displacement is denoted by  $\Delta_T$ .

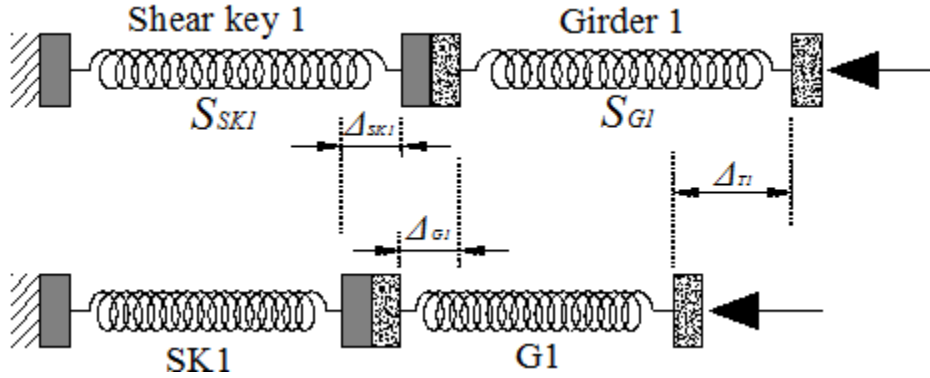


Fig. 5.5 Spring model for each pair of girder and shear key.

The compatibility equation for deformation can be written as:

$$\Delta_{T1} = \Delta_{SK1} + \Delta_{G1} \quad (5.1)$$

where in elastic range,

$$\Delta_{SK1} = \frac{F_{C1}}{S_{SK1}} \quad (5.2)$$

$$\Delta_{G1} = \frac{F_{C1}}{S_{G1}} \quad (5.3)$$

By substituting Eqs. (5.2) and (5.3) into Eq. (5.1), Eq. (5.1) becomes

$$\Delta_{T1} = \frac{F_{C1}}{S_{SK1}} + \frac{F_{C1}}{S_{G1}} \quad (5.4)$$

Eq. (5.4) can be rewritten as:

$$S_{EQ1} = \frac{F_{C1}}{\Delta_{T1}} = \frac{S_{SK1}S_{G1}}{S_{SK1}+S_{G1}} \quad (5.5)$$

where  $S_{EQ1}$  represents the equivalent total stiffness of the spring series system.

For fixed shear keys,

$$S_{SK1} \gg S_{G1}, \Delta_{SK1} \approx 0 \quad (5.6)$$

$$S_{EQ1} \approx S_{G1}, \Delta_{G1} \approx \Delta_{T1} \quad (5.7)$$

For movable shear keys,

$$S_{EQ1} < \min(S_{G1}, S_{SK1}), \Delta_{G1} < \Delta_{T1} \quad (5.8)$$

#### 5.4.2 Stiffness variations in compound model

For the compound model shown in Fig. 5.4, the stiffness of each spring can be different from that of another spring, which can be used to analogize the stiffness variations of multiple girders. For instance, the girders can have different stiffness values due to the variations in dimensions. Even for girders with the same dimension, they can demonstrate different stiffness. For example, the multiple girder system shown in Fig. 5.3, the exterior girders demonstrate smaller stiffness than the interior girder under transverse load, because the exterior girders are only restrained by the deck on one side instead of on both sides.

The compatibility equation for parallel springs can be written as:

$$\Delta_T = \Delta_{Ti} = \Delta_{SKi} + \Delta_{Gi} \quad (5.9)$$

where in elastic range,

$$\Delta_{SKi} = \frac{F_{Ci}}{S_{SKi}} \quad (5.10)$$

$$\Delta_{Gi} = \frac{F_{Ci}}{S_{Gi}} \quad (5.11)$$

By substituting Eqs. (5.10) and (5.11) into Eq. (5.9), the equivalent spring constant is

$$S_{EQi} = \frac{F_{Ci}}{\Delta_T} = \frac{S_{SKi}S_{Gi}}{S_{SKi}+S_{Gi}} \quad (5.12)$$

By substituting Eq. (5.12) into Eq. (5.11),

$$\Delta_{Gi} = \frac{\Delta_T}{1+\alpha_i} \quad (5.11)$$

where  $\alpha_i$  represents the ratio of stiffness of the girder and shear key, and thus  $\alpha_i = S_{Gi}/S_{SKi}$ .

If the stiffness of G1 is smaller than that of G2 and the shear keys have the same stiffness  $S_{SK}$ , meaning  $S_{G1} < S_{G2}$  and  $S_{SK1} = S_{SK2}$ , then  $\alpha_1 < \alpha_2$ , and thus  $\Delta_{G1} > \Delta_{G2}$ . This explains why the exterior girders usually suffer more than the interior girders in earthquakes.

Differentiate equation 5.2.11 with regard to  $S_{SKi}$ ,

$$\frac{d\Delta_{Gi}}{dS_{SKi}} = \Delta_T \frac{S_{G1}}{(S_{SK1} + S_{G1})^2} > 0 \quad (5.12)$$

Each girder's deformation increases with the increase of the shear key's stiffness. To reduce girder's deformation, the shear key's stiffness needs to be decreased. Therefore, the movable shear keys can benefit bridge superstructures by adjusting the deformations of multiple girders that demonstrate different stiffness.

### 5.4.3 Boundary variations in compound model

If all the contacts are established simultaneously, meaning there is no gap, each series springs can be analyzed following the above procedures. However, there are always unequal gaps between the shear key and girder due to construction errors, meaning the contacts cannot be established at the same time in the real world. The investigations in Chapter 4 have indicated that millimeter-order gaps can significantly reduce the structure's capacity. Such problems can be explained by boundary variations in the model of compound springs as illustrated in Fig. 5.6. The construction error is represented by a gap between the shear key and girder, which is denoted by  $\Delta_{ei}$  and  $i$  represents the girder/shear key number.

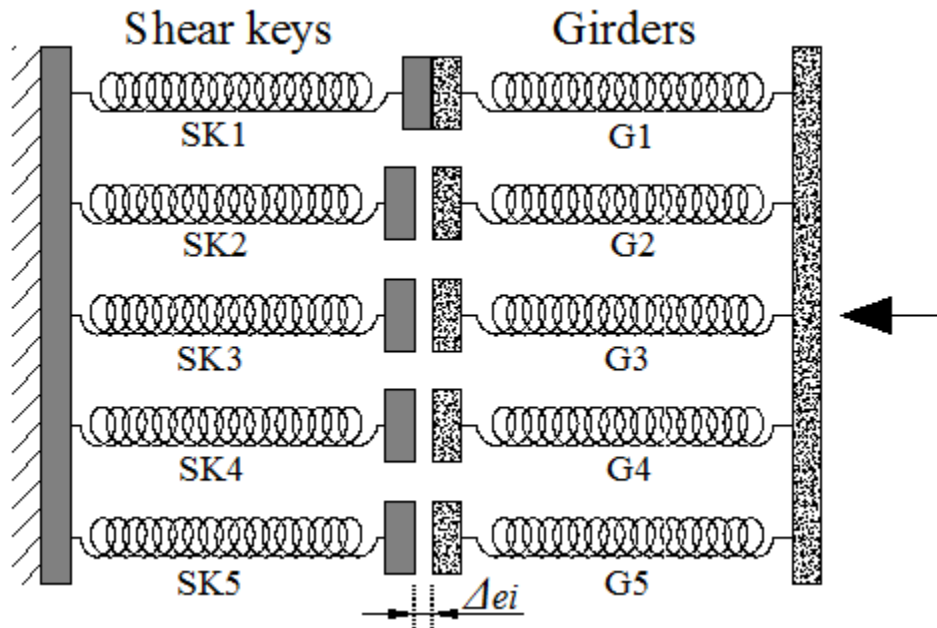


Fig. 5.6 The model of compound springs with gaps.

The compatibility equation for deformation can be written as:

$$\Delta_{Ti} = \Delta_{SKi} + \Delta_{Gi} \quad (5.13)$$

where in elastic range,

$$\Delta_{SKi} = \frac{F_{Ci}}{S_{SKi}} \quad (5.14)$$

$$\Delta_{Gi} = \frac{F_{Ci}}{S_{Gi}} \quad (5.15)$$

By substituting Eqs. (5.14) and (5.15) into Eq. (5.13),

$$\Delta_{Ti} = F_{Ci} \left( \frac{1}{S_{SKi}} + \frac{1}{S_{Gi}} \right) \quad (5.16)$$

The total transverse force can be obtained by:

$$F_C = \sum_1^n F_{Ci} = \sum_1^n \left( \frac{\Delta_{Ti}}{\frac{1}{S_{SKi}} + \frac{1}{S_{Gi}}} \right) \quad (5.17)$$

where  $n$  represents the number of girders that contact shear keys, and  $i=1,2,3,\dots,n..$

$$\Delta_{Ti} = \Delta_{T1} - \Delta_{ei} \quad (5.18)$$

For convenience, let

$$\Delta_{e2} \leq \Delta_{e3} \leq \Delta_{e4} \leq \Delta_{e5} \quad (5.19)$$

With the increase of transverse load, there will be a moment when  $\Delta_{T1} = \Delta_{e2}$ , which represents the second girder starts contacting the shear key. Thus, afterward it will contribute to resist the transverse load with the first girder. By substituting  $\Delta_{T1} = \Delta_{e2}$  into Eq. (5.16),  $F_{C1}$  can be calculated:

$$F_{C1} = \Delta_{e2} \left( \frac{S_{SK1} S_{G1}}{S_{SK1} + S_{G1}} \right) \quad (5.20)$$

Differentiating Eq. (5.20) with respect to  $S_{SK1}$  leads to

$$\frac{dF_{C1}}{dS_{SK1}} = \Delta_{e2} \left( \frac{S_{G1}}{S_{SK1} + S_{G1}} \right)^2 > 0 \quad (5.21)$$

Similarly, such deductions can be extended to other girders, and they can be written as:

$$\frac{dF_{Ci}}{dS_{SKi}} = (\Delta_{e(i+1)} - \Delta_{ei}) \left( \frac{S_{Gi}}{S_{SKi} + S_{Gi}} \right)^2 > 0 \quad (5.22)$$

Therefore, when the construction error value is constant, the reaction force applied on G1 can be reduced by the reduction of the shear key's stiffness. In other words, the movable shear key can benefit the bridge superstructure when construction error is unavoidable.

## 5.5 Evaluation of Movable Shear Keys

### 5.5.1 Without construction error

Without considering the construction error, all girders contact shear keys simultaneously, which corresponds to the case in Fig. 5.4. The transverse stiffness can capacity can be designed by adjusting the sizes of the bars in the movable shear keys. Three diameters were investigated, which were 5 mm, 10 mm, and 20 mm. The FC was set as 0.2.

(1) Diameter 5 mm bars

For shear keys with 5 mm bars, the maximum principal stress distribution under self-weight, prestressing, and transverse force is shown in Fig. 5.7 that shows the multiple girders are subjected to similar stress

distributions. Since the maximum principle stress was smaller than the cracking stress, the concrete did not crack. The failure was caused by the yielding of the bars in the shear keys that is illustrated in Fig. 5.1. The amplified displacement is shown in Fig. 5.8 where the transverse drift was manifested.

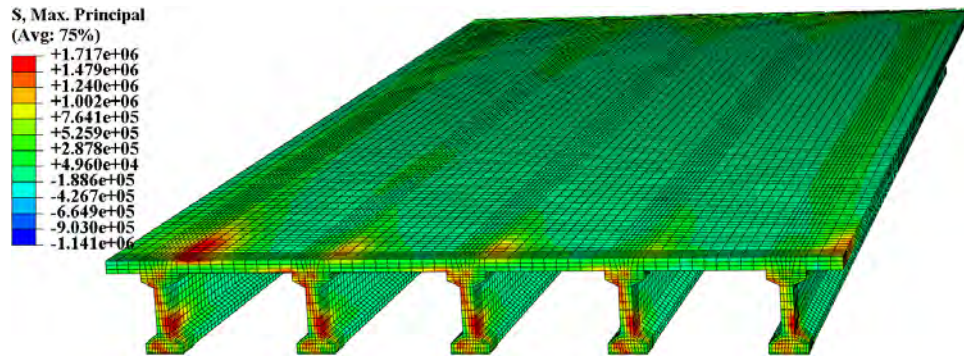


Fig. 5.7 Maximum principal stress. ( $\times 10$ ).

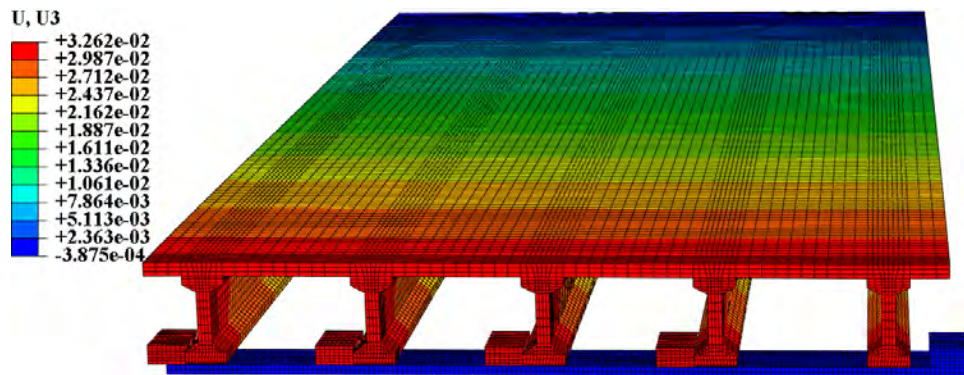


Fig. 5.8 Transverse drift. ( $\times 10$ ).

(2) Diameter 10 mm bars

For shear keys with 10 mm bars, the maximum principal stress distribution under self-weight, prestressing, and transverse force is shown in Fig. 5.9 that shows the multiple girders are subjected to similar stress distributions. Since the maximum principle stress was smaller than the cracking stress, the concrete did not crack. The failure was caused by the yielding of the bars in the shear keys. The amplified displacement is shown in Fig. 5.10 where the transverse drift was manifested.

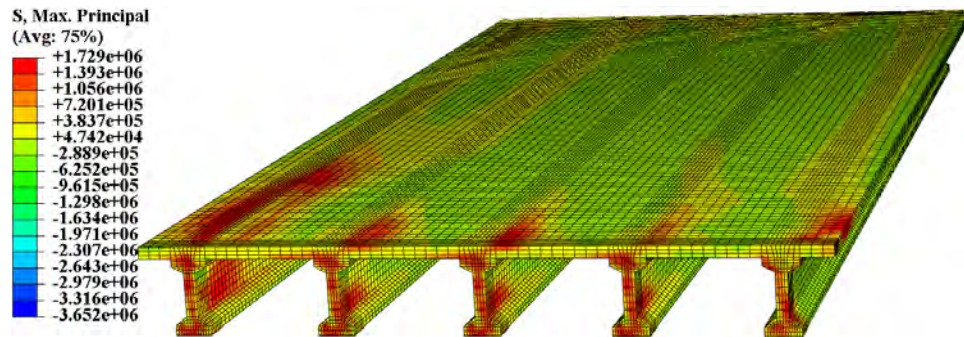


Fig. 5.9 Maximum principal stress. ( $\times 10$ ).

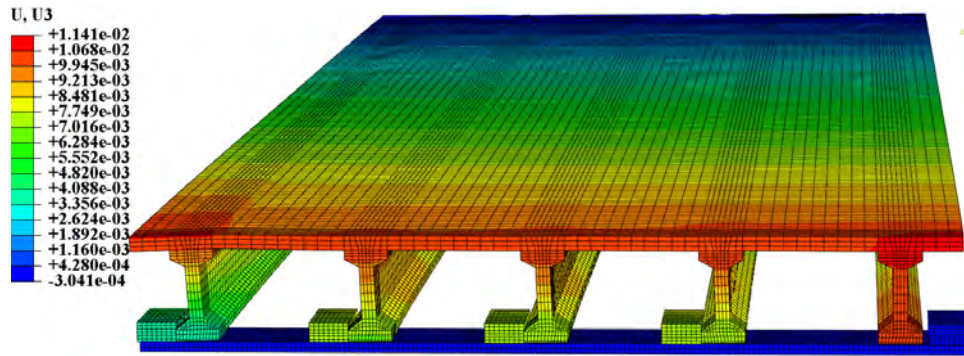


Fig. 5.10 Transverse drift. ( $\times 10$ ).

(3) Diameter 20 mm bars

For shear keys with 20 mm bars, the maximum principal stress distribution under self-weight, prestressing, and transverse force is shown in Fig. 5.11 that shows the multiple girders are subjected to similar stress distributions. Cracks appeared at the top of the deck and the webs of each girder. The failure mode is similar to that of the bridges with fixed shear keys. The amplified displacement is shown in Fig. 5.12 where the transverse drift was manifested.

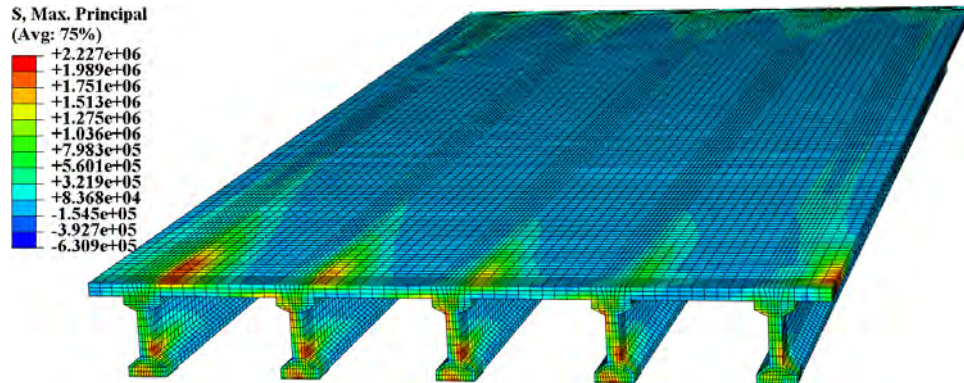


Fig. 5.11 Maximum principal stress. ( $\times 10$ ).

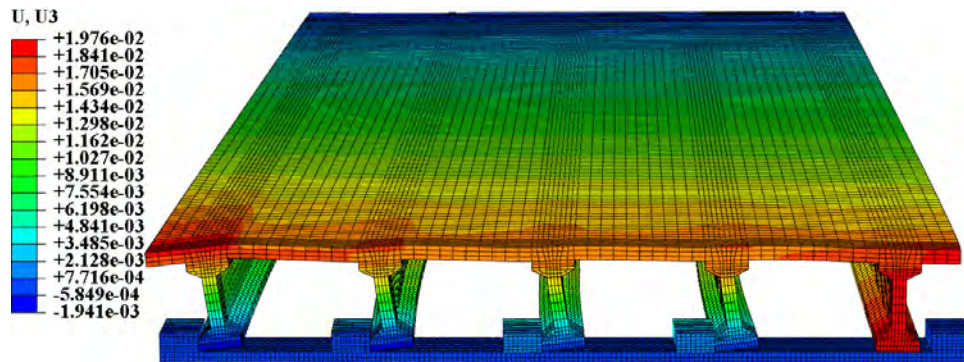
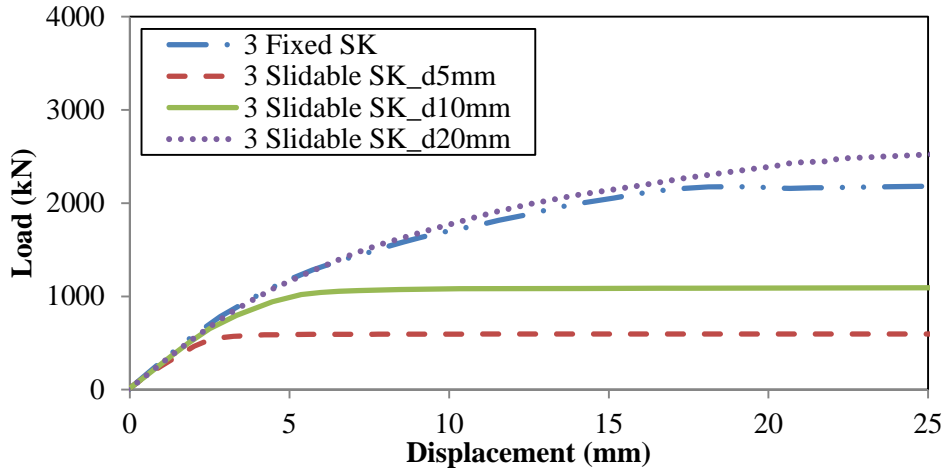


Fig. 5.12 Transverse drift. ( $\times 10$ ).

By the simulations of bridges with different shear key configurations, pushover curves are obtained and compared in Fig. 5.13, from which it can be observed that the bars yield when the diameters are 5 mm or 10 mm in movable shear keys. When 20 mm bars are used, rupture of concrete and yield of rebar in superstructure will happen. The movable shear keys can help the superstructure demonstrate higher capacity than the fixed shear keys.





**Fig. 5.13 Comparisons of pushover curves of bridges with different shear key configurations.**

### 5.5.2 Boundary variations

When the gap widths between the girders and shear keys are not the same, the contacts will not be established simultaneously, which has been introduced in Section 5.4.3 by the springs model. This problem was investigated by finite element analysis. When the exterior girder contacts the exterior shear key, four gaps were set for the other four girders, and the gap width was 5 mm. The bridges introduced in the Section 5.5.1 were investigated with 5mm preset gaps and compared with the bridge that did not have gap between the girders and shear keys. The studied bridges with 5mm gaps include one bridge with fixed shear keys and two bridges with movable shear keys. The diameters of bars in the movable shear keys were 5 mm and 10 mm, respectively. The FC was 0.2 in the simulations. The pushover curves are shown in Fig. 5.14.

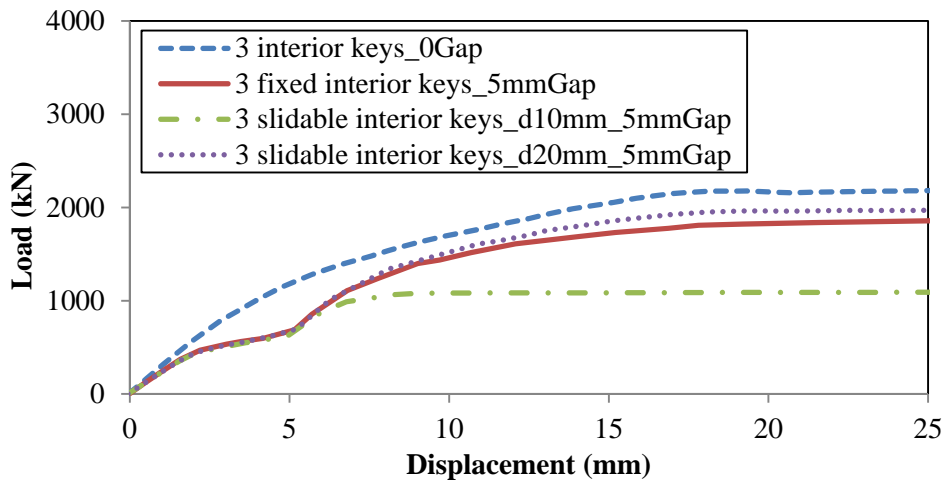


**Fig. 5.14 Comparisons of pushover curves of bridges with gaps.**

At the beginning, the single exterior girder resisted the transverse movement solely. The concrete cracked and the some rebar yielded. Then the contacts for the other four girders were established and all girders resist the transverse load together. By the comparison of the three bridges with preset gaps, the one with movable shear keys connected by 20 mm bars gained the highest capacity that was a little smaller than the ideal bridge with no gap.

## 5.6 Summery

A concept of movable shear key was presented, which benefits the bridge superstructures and the substructures. The transverse ductility could be appreciably improved. The stiffness was reduced which helps multiple girder configurations work better together, and it could possibly reduce the demand capacity in the seismic design. In summary, the movable shear keys benefit the bridge in four areas..

The ductility of the bridge can be significantly increased, which prevents ‘sudden failure’ from happening in earthquakes. More energy will be dissipated by the yielding of bars and the friction between components.

The demand capacity can be reduced by the decrease of transverse stiffness.

When unequal gaps existed due to the construction error, the movable shear keys could postpone the failure of the girders that contact the shear keys relatively earlier than other girders. Multiple girders can better work together, and thus higher capacity can be demonstrated.

When individual girder in the multi-girder system have different transverse stiffness, the movable shear keys can reduce the displacements of girders that have smaller stiffness than other girders, which will postpone the failure of girders with smaller stiffness and thus will improve the structural performance.

A model of compound springs was presented for analytical analysis of the working principles of the proposed design of movable shear keys. The model successfully interpreted the advantages of the movable shear keys, and was validated by numerical simulations.

## SECTION 6 CONCLUSIONS

Based on extensive simulations both analytically and numerically, several conclusions can be drawn.

(1) The vertical behavior of a concrete girder bridge superstructure is insignificantly influenced by the configuration and size of end diaphragms or the friction coefficient of supports.

(2) The thickness and height of end diaphragms can significantly increase the transverse capacity of a multi-girder bridge superstructure.

(3) The friction coefficient of bridge girders on their support surfaces can also significantly increase the transverse capacity of a girder bridge superstructure.

(4) The interior shear keys can significantly improve the seismic performance of a multi-girder bridge. Their effect is more robust than the friction. The transverse capacity of a multi-girder bridge superstructure can be increased almost linearly with the number of interior shear keys.

(5) A design of movable shear keys was presented and evaluated by numerical simulations. It was found effective to improving the seismic performance of a multi-girder bridge.

(6) A model of compound springs was analytically developed and numerically validated to quantify the effectiveness of shear keys.

## REFERENCES

1. Arora, D., Traber, J., and Byres, R. (2013) Accelerated Bridge Construction (ABC) Techniques for Heavy Lift (HL) & Materials Off-Loading Facility (MOF). Ports 2013: pp. 570-579. doi: 10.1061/9780784413067.059
2. Attanayake, U., Abudayyeh, O., Cooper, J., Mohammed, A., and Aktan, H. (2014). "First Full-Depth Deck-Panel Accelerated Bridge Construction Project in Michigan: Constructability Challenges and Lessons Learned." *J. Perform. Constr. Facil.* 28, SPECIAL SECTION: Performance of Bridges under Critical Natural Hazards, 128–135.
3. Li, L., Ma, Z., and Oesterle, R. (2010). "Improved Longitudinal Joint Details in Decked Bulb Tees for Accelerated Bridge Construction: Fatigue Evaluation." *J. Bridge Eng.*, 15(5), 511–522.
4. Wen-Huei Phillip Yen, Genda Chen, Mark Yashinsky, Youssef Hashash, Curtis Holub, Kehai Wang, and Xiaodong Guo, China Earthquake Reconnaissance Report: Performance of Transportation Structures During the May 12, 2008, M7.9 Wenchuan Earthquake. Publication No. FHWA-HRT-11-029, Federal Highway Administration, February 2011.
5. Wen-Huei Phillip Yen, Genda Chen, Ian Buckle, Tony Allen, Daniel Alzamora, Jeffrey Ger, and Juan G. Arias, Post-earthquake Reconnaissance Report on Transportation Infrastructure Impact of the February 27, 2010, Offshore Maule Earthquake in Chile. Publication No. FHWA-HRT-11-030, Federal Highway Administration, March 2011.
6. Norbert Büchter, Ekkehard Ramm and Deane Roehl. (2005). Three-dimensional extension of non-linear shell formulation based on the enhanced assumed strain concept. *International Journal for Numerical Methods in Engineering*. Volume 37, Issue 15, pages 2551–2568, 15 August 1994.
7. A.M. Citipitioglu, R.M. Haj-Ali, D.W. White. (2002). Refined 3D finite element modeling of partially-restrained connections including slip. *Journal of Constructional Steel Research*. 58, 995–1013.
8. Jason Tak-Man Cheung, Ming Zhang, Aaron Kam-Lun Leung, Yu-Bo Fan. (2005). Three-dimensional finite element analysis of the foot during standing—a material sensitivity study. *Journal of Biomechanics*. 38(5), 1045–1054.
9. Abeyinghe, R., Gavaise, E., Rosignoli, M., and Tzaveas, T. (2002). "Pushover Analysis of Inelastic Seismic Behavior of Greveniotikos Bridge." *J. Bridge Eng.*, 7(2), 115–126.
10. Zhihao Lu, Hanbin Ge, Tsutomu Usami. (2004). "Applicability of pushover analysis-based seismic performance evaluation procedure for steel arch bridges." *Eng. Structures*, 26, 1957 – 1977.
11. Dynamic of Structures: Theory and Applications to Earthquake Engineering, 3<sup>rd</sup> Edition, New Jersey: Prentice-Hall.
12. Vidic, T., Fajfar, P., and Fischinger, M. (1994). Consistent inelastic design spectra: strength and displacement. *Earthquake Engineering and Structural Dynamics* 23(5) 507-521.
13. Peter Fajfar, M.EERI. (2000). A Nolinear Analysis Method for Performance Based Seismic Design. *Earthquake Spectra*, Vol.16, No.3, pp.573-592.
14. Peter Fajfar. (1999). Capacity spectrum based on Inelastic demand .*Earthquake engineering and structural dynamics* , pp.979-993.
15. Chopra, A.K. and Goel, R.K. (2001). A Modal Pushover Analysis Procedure to Estimate Seismic Demands for Buildings: Theory and Preliminary Evaluation. Tech. Rep.2001/3, Pacific Earthquake Engineering Research Center, University of California, Berkeley, CA.
16. ABAQUS user manual 6.12.

17. Hillerborg, A., M. Modeer, and P. E. Petersson, "Analysis of Crack Formation and Crack Growth in Concrete by Means of Fracture Mechanics and Finite Elements," *Cement and Concrete Research*, vol. 6, pp. 773–782, 1976.
18. Lee, J., and G. L. Fenves, "Plastic-Damage Model for Cyclic Loading of Concrete Structures," *Journal of Engineering Mechanics*, vol. 124, no.8, pp. 892–900, 1998.
19. Rakesh K. Gael, and Anil K. Chopra. (2008) Role of Shear Keys in Seismic Behavior of Bridges Crossing Fault-Rupture Zones. *ASCE, Journal of Bridge Engineering*, Vol. 13, pp. 398-408.
20. Joseph J. Rencis and Sachin Terdalkar. (2007). Stress Concentrations and Static Failure for Common Elements used in Finite Element Stress Analysis. Proceedings of the 2007 Midwest Section Conference of the American Society for Engineering Education.
21. Crisfield MA. A Fast Incremental/Iteration Solution Procedure that Handles `Snap-Through. *Computers and Structures*, vol. 13, pp. 55–62, 1981.
22. G Powell and J Simons. Improved Iterative Strategy for Nonlinear Structures. *International Journal for Numerical Methods in Engineering*, vol. 17, pp. 1455–1467, 1981.
23. Ramm E. Strategies for Tracing the Nonlinear Response Near Limit Points. *Nonlinear Finite Element Analysis in Structural Mechanics*, Edited by E. Wunderlich, E. Stein, and K. J. Bathe, Springer-Verlag, Berlin, 1981.
24. Azadeh Bozorgzadeh, Sami Hanna Megally, Scott A. Ashford, and José I. Restrepo. (2007). Seismic Response of Sacrificial Exterior Shear Keys in Bridge Abutments. University of California, San Diego.
25. Sami Hanna Megally, Perdo F. Silva, and Frieder Seible. (2002). Seismic Response of Sacrificial Shear Keys in Bridge Abutments. University of California, San Diego.
26. Cai, C. S., Chandolu. A., and Araujo, M. (2009). Quantification of Intermediate Diaphragm Effects of Prestressed Concrete Girder Bridges on Load Distributions. *PCI Journal*, 54(2), 48-63.
27. Cai, C. (2005). "Discussion on AASHTO LRFD Load Distribution Factors for Slab-on-Girder Bridges." *Pract. Period. Struct. Des. Constr.*, 10(3), 171–176.
28. Bozorgzadeh, A., Megally, S., Restrepo, J., and Ashford, S. (2006). "Capacity Evaluation of Exterior Sacrificial Shear Keys of Bridge Abutments." *J. Bridge Eng.*, 11(5), 555–565.